A Measurement of the Mass of the Top Quark using the Ideogram Technique

ISBN 978-90-9024-076-3

Cover: An artistic impression of an *event* of a proton anti-proton collision recorded with the DØ detector on June 7 2004. A top quark pair was probably formed in this collision.

The work described in this thesis is part of the research program of the 'Nationaal Instituut voor Kernfysica en Hoge-Energiefysica (Nikhef)' in Amsterdam, the Netherlands. The author was financially supported by the 'Stichting voor Fundamenteel Onderzoek der Materie (FOM)'.

A Measurement of the Mass of the Top Quark using the Ideogram Technique

ACADEMISCH PROEFSCHRIFT

TER VERKRIJGING VAN DE GRAAD VAN DOCTOR
AAN DE UNIVERSITEIT VAN AMSTERDAM
OP GEZAG VAN DE RECTOR MAGNIFICUS
PROF. DR. D.C. VAN DEN BOOM
TEN OVERSTAAN VAN EEN DOOR HET COLLEGE VOOR PROMOTIES
INGESTELDE COMMISSIE, IN HET OPENBAAR TE VERDEDIGEN
IN DE AULA DER UNIVERSITEIT
OP WOENSDAG 3 JUNI 2009, TE 10:00 UUR

door

Pieter Willem Huib Houben

geboren te Nijmegen

promotores:	prof. dr. M.W.J.M. Demarteau
	prof. dr. F.L. Linde
co-promotor:	dr. M. Vreeswijk

Faculteit der Natuurwetenschappen, Wiskunde en Informatica

Contents

Introduction

About twenty four centuries ago, the Greek philosopher Demokritos stated that matter is composed of indivisible constituents that determine its characteristics. Such a building block he called ἀτομος (atomos). This statement that there is an indivisible smallest particle was merely a postulate. From natural observations he inferred characteristics on the atomos.

More than two millennia later, after many chemical experiments, the idea had been formed that all matter is made of elements or combinations of elements. In 1803 John Dalton suggested that each element consists of unique atoms which can be combined to form compounds, thus reviving Demokritos' idea of the atomos [1]. The atom, as suggested by Dalton, had at least one characteristic in common with the atomos predicted by Demokritos: the atoms characterized the elements. In addition, they also seemed indivisible.

In 1911 Rutherford discovered that the atom has an internal structure [2], consisting of a nucleus and a cloud of electrons surrounding it. The electron had been discovered as a separate particle in 1897 by J.J. Thomson [3]. In 1919 it was Rutherford again who discovered the proton [4], which is one of the constituents of the atomic nucleus. The nucleus itself thus has an internal structure. In 1932 James Chadwick discovered the neutron [5], which appeared to be a neutral copy of the proton, and is the other constituent of the atomic nucleus. Not only is the atom built from smaller constituents, it is not indivisible: electrons can be split off from atoms and the nucleus itself can be split. Thus, although the atoms characterize the elements, like Demokritos' atomos, they are divisible in protons, neutrons, and electrons.

Throughout the twentieth century many particles similar to the proton and the neutron were discovered. These were called hadrons and were found to be categorizable in the group of mesons and the group of baryons. Similar to the neutron in β decay, the hadrons decay into other particles. However, no internal structure of the hadrons was observed.

The hadrons were regarded as indivisible and elementary, i.e. without an internal structure, until in 1961 Murray Gell-Mann was able to explain the characteristics of the hadrons by stating that they are built from smaller constituents which he called quarks [6]. Gell-Mann needed the existence of three different species (or flavours) of

quarks to explain all hadrons observed in those days. Three quarks or three anti-quarks together form a baryon, like the proton and the neutron. A quark and an anti-quark together form a so called meson. As even more hadrons were discovered, additional quark flavours were needed. There are six quark flavours, which at present are believed to be elementary. Only the lightest two quarks are abundent in nature. The others can be produced either artificially in an experiment or in showers of cosmic rays. After creation, a hadron containing one of the four heavy quarks, will decay. The particles and the ways in which they interact are described by the Standard Model.

The heaviest quark is the so called top quark. It is approximately thirty times as heavy as the second heaviest quark. It was discovered in 1995 at the Tevatron proton anti-proton collider [7, 8]. The Tevatron at present collides protons with anti-protons at a centre-of-mass energy of 1.96 TeV. Part of the enormous energy in such a collision can be used to create mass. This way, in these collisions, new particles can be formed, including top quarks. At the moment the Tevatron collider is the only collider energetic enough to produce top quarks. The top quark is special, because it decays before it hadronizes, that is, before it combines with other quarks to form a hadron. Due to the decay, the top quark cannot be observed directly, but its decay products can be, and via these its properties are measured.

One of the interesting properties of the top quark is its mass. Knowledge of the mass of the top quark is important, because it constrains the mass of the not yet observed Higgs boson. The Higgs boson has been predicted in order to explain the masses of the particles within the Standard Model. It has not been observed yet and finding it is one of the great quests of many particle physicists at the moment. Because the mass of the top quark is correlated with the mass of the Higgs boson, precise knowledge of the first helps to constrain the allowed values for the latter. Also, it is known that the Standard Model cannot be the final description of nature at the sub-nuclear scale, for it does not describe e.g. quantum gravitation or dark matter, which are clearly present in the universe. As one of the variables in the Standard Model, the top quark mass is important to check the consistency of the model and precise knowledge of the model may lead to a better understanding of the underlying physical principles and may be the gateway to new physics.

This thesis describes a measurement of the mass of the top quark on data collected with the DØ detector at the Tevatron collider in the period from 2002 until 2006. The first chapter describes the Standard Model and the prominent role of the top quark mass. The second chapter gives a description of the DØ detector which is used for this measurement. After the $p\bar{p}$ collisions have been recorded, reconstruction of physics objects is required, which is described in Chapter 3. Chapter 4 describes how the interesting collisions in which top quarks are produced are separated from the 'uninteresting' ones with a set of selection criteria. The method to extract the top quark mass from the sample of selected collisions (also called events), which is based on the ideogram technique, is explained in Chapter 5, followed in Chapter 6 by

the description of the calibration of the method using simulation of our most precise knowledge of nature. Chapter 7 shows the result of the measurement together with some cross checks and an estimation of the uncertainty on this measurement. This thesis concludes with a constraint on the Higgs boson mass.

Chapter 1

The top quark

1.1 The Standard Model

The best description of nature at the subnuclear scale is provided by the Standard Model (SM) of particle physics [9]–[15]. The Standard Model is a quantum field theory describing particles and their interactions, based on local gauge invariance. The elementary particles of the Standard Model are listed in Table 1.1. The particles are classified as those with half-integer spin, the fermions, and those with integer spin, the bosons.

Quarks and leptons are matter particles and are fermions. The six types of quarks (with negative chirality), called flavours, can be grouped in three weak isospin doublets: the up quark (u), the charm quark (c) and the top quark (t) have electric charge $+\frac{2}{3}e$ and weak isospin $+\frac{1}{2}$ and are the isospin partners of, respectively, the down quark (d), the strange quark (s) and the bottom quark (b), which have electric charge $-\frac{1}{3}e$ and weak isospin $-\frac{1}{2}$. Similar to the quarks, the leptons with negative chirality are grouped in three weak isospin doublets: the electron neutrino (ν_e), the muon neutrino (ν_μ) and the tau neutrino (ν_τ) are electrically neutral and have weak isospin $+\frac{1}{2}$. Their isospin partners have electric charge $-e$ and weak isospin $-\frac{1}{2}$. They are, respectively, the electron (e), the muon (μ) and the tau lepton (τ). The quarks and leptons with positive chirality are singlets and have weak isospin 0.

The Standard Model incorporates three fundamental forces which are mediated by the gauge bosons, which have spin $1\hbar$. The gauge boson which propagates the electromagnetic force is the photon (γ). The weak force is propagated by the $W^\pm$ and Z bosons, described by the electroweak theory. The gluons (g) carry the strong force, described by quantum chromodynamics (QCD). The only other fundamental force in nature, gravity, has not been incorporated in the Standard Model yet. Though important in daily life, gravity is of no importance for the processes described in this analysis.

	particles	spin/$\hbar$	electric charge/e
quarks	$u \quad c \quad t$ $d \quad s \quad b$	$\frac{1}{2}$	$+\frac{2}{3}$ $-\frac{1}{3}$
leptons	$\nu_e \quad \nu_\mu \quad \nu_\tau$ $e^- \quad \mu^- \quad \tau^-$	$\frac{1}{2}$	0 -1
gauge bosons	γ Z $W^\pm$ g	1	0 0 ± 1 0
Higgs boson	H	0	0

Table 1.1: *The particles of the Standard Model with their spin and electric charge (expressed in unit charge e, which is the charge of the positron). The Higgs boson has not been observed.*

Several particles listed in Table 1.1 have corresponding anti-particles with the anti-particle having an electric charge opposite to that of its corresponding particle. The electrically neutral gauge bosons are their own anti-particles.

1.1.1 Electroweak theory

Electrically charged particles interact via the electromagnetic force, which is carried by the photon. Its coupling is the fine structure constant, $\alpha = e^2/4\pi\epsilon_0\hbar c$, which depends on the energy scale of the process considered, which is called the running of α. For increasing energy, α increases. For very low energies α is approximately $1/137$, whereas at the Z boson mass it is approximately $1/128$ [16]. The weak force is carried by the W bosons and the Z boson, which have more intricate couplings than the photon. The combined electromagnetic and weak interactions are described by a $SU(2) \times U(1)$ symmetry.

The Brout-Englert-Higgs mechanism

To endow the W and Z boson with mass, the Standard Model needs a mechanism that spontaneously breaks the underlying $SU(2) \times U(1)$ symmetry of the electroweak theory. The mechanism in the Standard Model is the Brout-Englert-Higgs mechanism, also called the Higgs mechanism. The Higgs mechanism introduces a scalar doublet field with a vacuum energy expectation value of 246 GeV, which breaks the underlying symmetry. This gives rise to the existence of a massive, scalar particle, the Higgs boson, which couples directly to each field in the Standard Model with a coupling

constant proportional to the mass of the corresponding particle. The Higgs boson has not been observed.

The mass of the Higgs boson is a free parameter in the Standard Model. At the large electron positron collider (LEP) at CERN a lower limit on the mass of the Higgs boson of 114.4 GeV/c^2 at 95 % confidence level was determined by direct searches [17]. The Higgs boson contributes indirectly to other measured processes, such as the production of W and Z bosons, via higher order quantum loop corrections, which are explained below.

Quantum loop corrections

In the Standard Model at tree level, the mass of the W boson, M_W, is related to the mass of the Z boson, M_Z, the Fermi constant, G_μ, and the fine-structure constant, α, via the formula:

$$M_W^2 = \frac{M_Z^2}{2}\left(1 + \sqrt{1 - \frac{4}{M_Z^2}\frac{\pi\alpha}{\sqrt{2}G_\mu}}\right). \tag{1.1}$$

However, at higher order there are corrections to the pole mass of the W boson and Eq. 1.1 has to be modified:

$$M_W^2 = \frac{M_Z^2}{2}\left(1 + \sqrt{1 - \frac{4}{M_Z^2}\frac{\pi\alpha}{\sqrt{2}G_\mu}\frac{1}{1-\Delta r}}\right). \tag{1.2}$$

Δr contains by its definition all higher order effects that shift the mass of the W boson from its tree level value. The diagrams depicted in Fig. 1.1 contribute to the self energy of the W boson and thus cause a shift from its tree level mass [18, 19]. These corrections to the mass of the W boson are called radiative corrections.

The Feynman diagram in Fig. 1.1(a) shows a fermionic loop correction to the W propagator. The size of the fermionic loop corrections is:

$$\Delta r_{\text{fermionic}} = -\frac{\cos^2(\theta_W)}{\sin^2(\theta_W)}\Delta\rho_{\text{fermionic}}\,, \tag{1.3}$$

with:

$$\Delta\rho_{\text{fermionic}} = \frac{G_\mu}{8\sqrt{2}\pi^2}\sum_i C_i \Delta m_i^2\,, \tag{1.4}$$

where the sum is over the quark and lepton weak isospin doublets, and θ_W is the Weinberg angle. In Eq. 1.4 C_i is a colour factor. Hence for quarks $C_i = 3$, while $C_i = 1$ for leptons. In Eq. 1.4 Δm_i is the mass difference between the two particles in a lepton or quark doublet. Because the mass difference is negligible for all doublets except for the one with the top quark and the bottom quark, $\Delta\rho_{\text{fermionic}}$ equals to good approximation (neglecting the mass of the b quark):

$$\Delta\rho_{\text{fermionic}} \approx \Delta\rho_{\text{fermionic}}^{\text{top}} \approx \frac{G_\mu}{8\sqrt{2}\pi^2} 3 m_t^2\,, \tag{1.5}$$

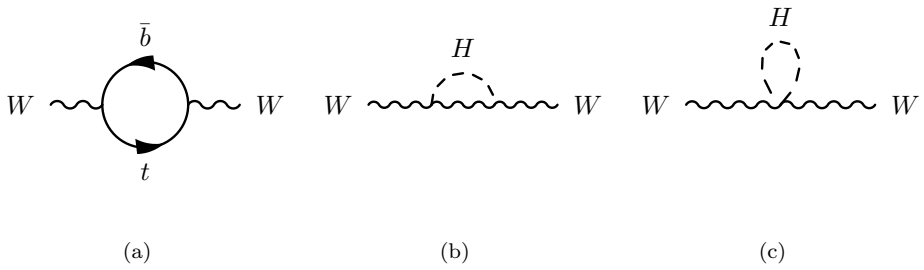

Figure 1.1: *Feynman diagrams illustrating loop corrections to the self energy of the W boson.*

which, for a top quark mass of 172.6 GeV/c^2, is 0.00934.

The Higgs boson also contributes to a shift in M_W through the bosonic loops which are shown at lowest order in Fig. 1.1(b) and 1.1(c). The contribution is logarithmic in the mass of the Higgs boson [20]:

$$\Delta r_{\text{Higgs}} \approx \frac{G_\mu M_W^2}{8\sqrt{2}\pi^2}\frac{11}{3}(\ln\frac{M_H^2}{M_W^2} - \frac{5}{6}), \tag{1.6}$$

which is -0.00107 for a Higgs boson mass of 120 GeV/c^2.

In addition Δr contains contributions from vacuum polarization, the running of α, vertex corrections, box corrections, and bosonic loop corrections to the mass of the Z boson. These do not depend on the mass of the top quark or on the mass of the Higgs boson and will be grouped to form Δr_{rest}. Δr can thus be written as:

$$\Delta r = -\frac{\cos^2(\theta_W)}{\sin^2(\theta_W)}\Delta\rho^{\text{top}}_{\text{fermionic}} + \Delta r_{\text{Higgs}} + \Delta r_{\text{rest}}\,. \tag{1.7}$$

Thus, in the Standard Model the masses of the W boson, top quark and Higgs boson are interrelated. If one knows the mass of the top quark and the mass of the W boson, one can constrain the mass of the Higgs boson. The present indirect upper limit on the mass of the Higgs boson is found to be 182 GeV/c^2 at 95 % confidence level, when taking into account the lower limit from direct searches.

1.1.2 Quantum Chromodynamics

The strong interaction of quarks and gluons is described by quantum chromodynamics (QCD), which is a gauge field theory, based on $SU(3)_{\text{colour}}$ symmetry, with a strong coupling constant α_s. QCD requires the existence of eight gauge bosons, the gluons. The gluons couple to particles carrying a colour charge. There are three

colours and three corresponding anti-colours. Only quarks and gluons, which are also called partons, carry colour charge and therefore these are the particles that experience the strong force. A colour and its anti-colour together are colour neutral. The combination of three different colours or three different anti-colours are also colour neutral. Free particles must be colour neutral objects[1]. Therefore, quarks do not exist freely. They can only exist in hadrons, bound states of (anti-)quarks. This is called confinement. The hadrons can be divided in mesons, which consist of a quark and an anti-quark, and baryons, consisting of three quarks or three anti-quarks. The Standard Model also allows other bound states of quarks, but no conclusive evidence has been found for these yet. When two quarks or gluons separate, the gluon field between them at one point contains enough energy that it is energetically advantageous to create new quark pairs, which can then combine with the quarks already present to form hadrons. This process is called hadronization.

Two up and one down quark, called the valence quarks, constitute a proton. In addition, many quark anti-quark pairs and gluons, called sea quarks and gluons, exist dynamically within the proton.

The energy of a parton in a proton is given as the fraction, x, of the total proton energy. The probability that a parton with flavour a in a proton has a fraction x of the proton energy, is given by the parton distribution function (PDF), $f_a(x, Q^2)$. The PDF depends on the scale Q^2 of the process, which is the negative of the squared momentum transfer. The PDFs of several quarks and the gluon in the proton are shown in Fig. 1.2.

A highly energetic parton from a hard process in a proton anti-proton collision, hadronizes to form a *jet* of particles. If a final state quark radiates a highly energetic gluon, a separate particle jet can be formed. This process is called final state radiation (FSR). If in a particle collision one of the incoming partons radiates a gluon, it is called initial state radiation (ISR).

To calculate the cross section of a particular process in perturbative QCD, one sums over all relevant Feynman diagrams to the appropriate orders of α_s, using techniques called renormalization and regularization to avoid divergences [21]. The effective, renormalized coupling depends on Q^2, the square of the typical momentum scale of the process. In deep-inelastic proton anti-proton scattering, the square of the four-momentum transfer between the two quasi-free colliding quarks is used. However, for other processes, a different typical momentum scale must be chosen. E.g. for the final state parton showering process described in Section 3.1, the squared mass of the branching parton is used. The dependence of α_s on Q^2 is called the running of α_s and at next-to-leading order it is given by:

$$\alpha_s(Q^2) = \frac{\alpha_s(\mu_0^2)}{1 + (\frac{\alpha_s(\mu_0^2)}{12\pi})(33 - 2n_f)\ln(\frac{|Q^2|}{\mu_0^2})}, \tag{1.8}$$

[1] Free particles must even be colour singlets.

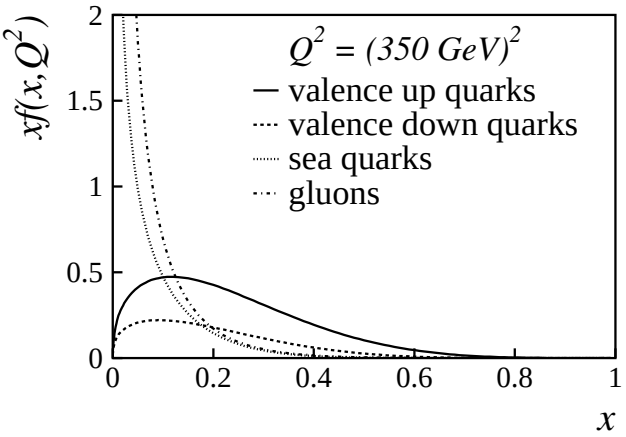

Figure 1.2: *The PDFs $f(x, Q^2)$ multiplied by the momentum fraction x as a function of x for the valence up quarks (solid line), the valence down quarks (dashed line), the sea quarks (dotted line), and the gluons (dashed/dotted line) in the proton. The PDFs were computed by CTEQ6L with $Q^2 = (350\,\mathrm{GeV})^2$.*

where n_f is the number of quark flavours that participate in the internal loops and μ_0^2 is a reference scale at which α_s has been measured. At higher orders, the relation between α_s and Q^2 depends on the renormalization scheme. A commonly used reference scale is the square of the mass of the Z boson where $\alpha_s = 0.118$ [16]. There is a $|Q|$ for which α_s is unity and perturbation theory no longer holds. This $|Q|$ is called Λ_{QCD} and is approximately 200 MeV. Any theoretical prediction using perturbative QCD can be derived only well above this scale. With increasing Q^2, α_s decreases and finally becomes zero. This behaviour is called asymptotic freedom.

1.2 Top quark properties

The top quark (t) was discovered by the CDF and DØ collaborations in 1995 [7, 8], after it had been predicted as the weak isospin partner of the observed bottom (b) quark. With a mass of approximately 172 GeV/c^2 the top quark is by far the heaviest of the known quarks and is approximately 35 times as heavy as its weak isospin partner, the b quark.

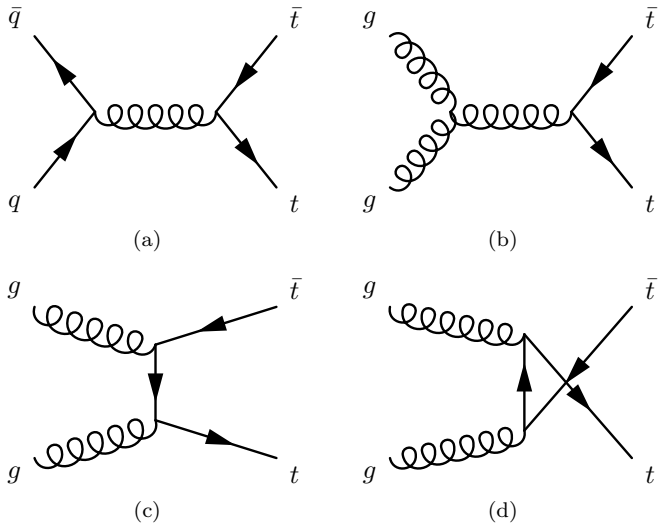

Figure 1.3: *The lowest order Feynman diagrams for the production of a top quark pair.*

1.2.1 Production of top quarks

The top quark is either 'pair produced' through QCD processes, or produced singly via the weak interaction. The four Feynman diagrams of top pair production at tree level are shown in Fig. 1.3. The top pair production cross section in proton anti-proton collisions at a centre-of-mass energy ($\sqrt{s}$) of 1.96 TeV is about 7 pb [22]. In proton anti-proton collisions at $\sqrt{s} = 1.96$ TeV the contribution of quark anti-quark annihilation to the top pair cross section is 85% and gluon fusion contributes 15% to the top pair cross section [23, 24]. The first evidence for single-top production was found by the DØ experiment in 2007 [25]. Single top production has a Standard Model cross section of about 3 pb.

In proton anti-proton collisions, the cross section ($\sigma_{t\bar{t}}$) for top pair production can be written as

$$\sigma_{t\bar{t}}(m_t) = \sum_{a,b} \int dx_a \, dx_b f_a^p(x_a, Q^2) f_b^{\bar{p}}(x_b, Q^2) \hat{\sigma}(ab \to t\bar{t}; \hat{s}, m_t), \tag{1.9}$$

where a and b label the colliding partons, carrying fractions x_a and x_b of the proton and anti-proton four-momenta, $\hat{\sigma}$ is the parton level cross section of the process $ab \to t\bar{t}$ at a centre-of-mass energy $\sqrt{\hat{s}}$ of the incoming partons and m_t is the mass of the top quark. f_a^p and $f_b^{\bar{p}}$ are the parton distribution functions.

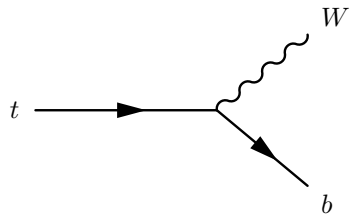

Figure 1.4: *The decay of a top quark to a W boson and a bottom quark.*

1.2.2 Decay of top quarks

The top quark decays before it hadronizes [26]. In the Standard Model in nearly 100% of the cases it decays to a W boson and a b quark, for which the Feynman diagram is shown in Fig. 1.4. Therefore, ignoring ISR and FSR for the moment, the signature of a top pair event is completely determined by the decays of the two W bosons. The W bosons either decay hadronically to a quark and an anti-quark or leptonically to a charged lepton and its corresponding (anti-)neutrino. In case both W bosons from the (anti-)top decay hadronically, there are six quarks from the top pair decay in the event. These quarks hadronize and form six particle jets. This is called the fully hadronic channel. If one W boson decays leptonically and the other one hadronically, the top pair event has 4 quarks, one charged lepton, and one neutrino. These events are called semi-leptonic events. If both W bosons decay leptonically, there are two quarks, two oppositely charged leptons and two (anti-)neutrinos in the event. This mode is called the fully leptonic channel. The branching fractions of a top pair for the different channels are displayed graphically in Fig. 1.5. The event signature is often more complicated, though, due to gluons coming from ISR or FSR which may give rise to additional jets.

Width of the top quark

Neglecting terms of order m_b^2/m_t^2, α_s^2, and $(\alpha_s/\pi)M_W^2/m_t^2$, the width of the top quark is [27]:

$$\Gamma_t = \frac{G_F m_t^2}{8\pi\sqrt{2}}\left(1-\frac{M_W^2}{m_t^2}\right)^2\left(1+2\frac{M_W^2}{m_t^2}\right)\left[1-\frac{2\alpha_s}{3\pi}\left(\frac{2\pi^2}{3}-\frac{5}{2}\right)\right]. \tag{1.10}$$

At a mass of the top quark of 175 GeV/c^2 the width of the top quark is 1.5 GeV/c^2.

1.2.3 Mass of the top quark

Figure 1.6 shows the plane of the mass of the W boson versus the mass of the top quark with the present 'world average' values within one standard deviation indicated by the ellipse (taken/updated from Ref. [28][29], including two-loop corrections for the precision observables [30]–[33]). The lines in the plane of M_W versus m_t in Fig.

1.6 represent constant Higgs boson masses. As can be seen in the figure, the present measurements of m_t and M_W prefer a Higgs boson with a mass below ~ 200 GeV/c^2. Also shown are the regions in M_W-m_t space allowed by the Standard Model and the minimal supersymmetric Standard Model (MSSM). The MSSM is the smallest supersymmetric extension of the Standard Model [34].

Good knowledge of the mass of the top quark (m_t) is especially interesting for three reasons:

- because of radiative corrections in the Standard Model, a precision measurement of m_t allows to put indirect constraints on the mass of the Higgs boson;
- the Yukawa coupling, y_t, of the top quark to the Higgs boson is given by:

$$y_t = \frac{\sqrt{2}\, m_t}{\nu}\,, \tag{1.11}$$

  with ν the vacuum expectation value of the Higgs field which is 246 GeV/c^2. The high mass of the top quark gives rise to a Yukawa coupling of the top quark to the Higgs boson close to unity, which may signal a special role for the top quark in the electroweak symmetry breaking which gives rise to all masses. The Yukawa coupling is unity if the top quark mass is 173.9 GeV/c^2;
- some models [35]–[42] suggest exotic production mechanisms of top quark pairs which would make the top quark pair cross section deviate from its Standard Model prediction. Because the cross section in the Standard Model depends

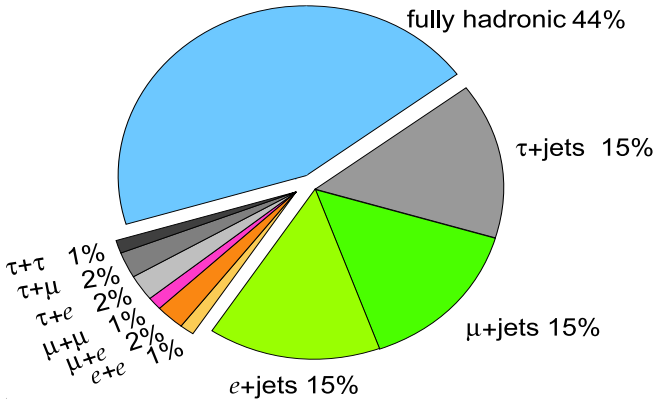

Figure 1.5: *The branching fractions of top quark pairs. The decay channels are categorized as the fully hadronic channel, the semi-leptonic channel and the fully leptonic channel.*

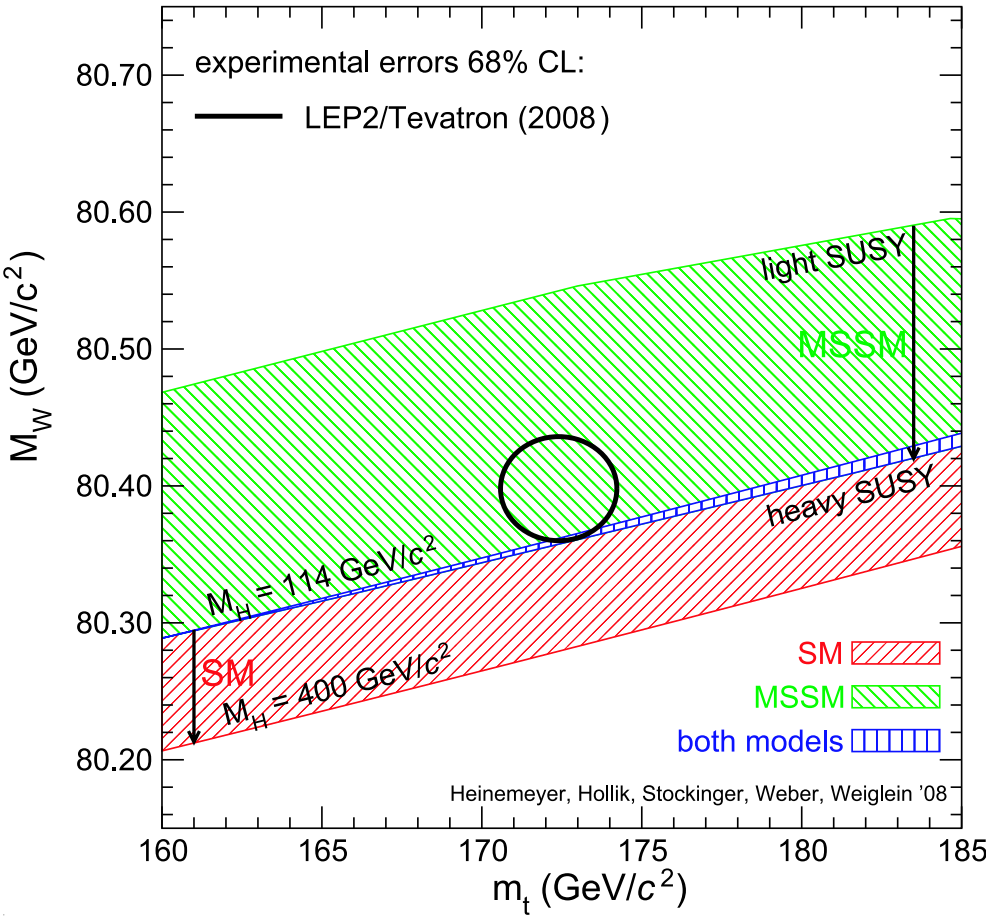

Figure 1.6: *The plane of the top quark mass and the mass of the W boson. In this plane the regions allowed by the Standard Model and an extension to the Standard Model, the minimal supersymmetric Standard Model (MSSM), are indicated. The ellipse indicates the 68% confidence interval of the present day measurements of the top quark mass and the W boson mass.*

strongly on the mass of the top quark, a precise knowledge of this mass constrains these models.

Chapter 2

Experimental setup

The data used in this analysis were collected with the DØ detector at the Fermilab Tevatron proton anti-proton collider. In this chapter the Tevatron collider and the DØ detector are described.

2.1 The Tevatron collider

The Tevatron collider, located at the Fermi National Accelerator Laboratory near Chicago, USA, is a ring of six kilometres in circumference in which protons and anti-protons collide at a centre-of-mass energy of 1.96 TeV. It operates with 36 bunches of protons and 36 bunches of anti-protons with a bunch spacing of 396 ns. During data taking in the summer of 2006 the Tevatron collider typically provided DØ with a luminosity of 90 pb^{-1} per month.

2.2 The DØ detector

The DØ detector, of which Fig. 2.1 shows a schematic overview, is a multi-purpose detector consisting of a central tracking system to reconstruct the primary and secondary vertices and to measure the trajectories of charged particles, a calorimeter system to measure a particle's energy, a muon system, and a dedicated trigger system. These systems are described in more detail in the following sections. The DØ detector also has forward proton detectors and luminosity counters, but, since both subsystems are not used directly for this analysis, these will not be described here. The DØ detector is described in detail in Ref. [43].

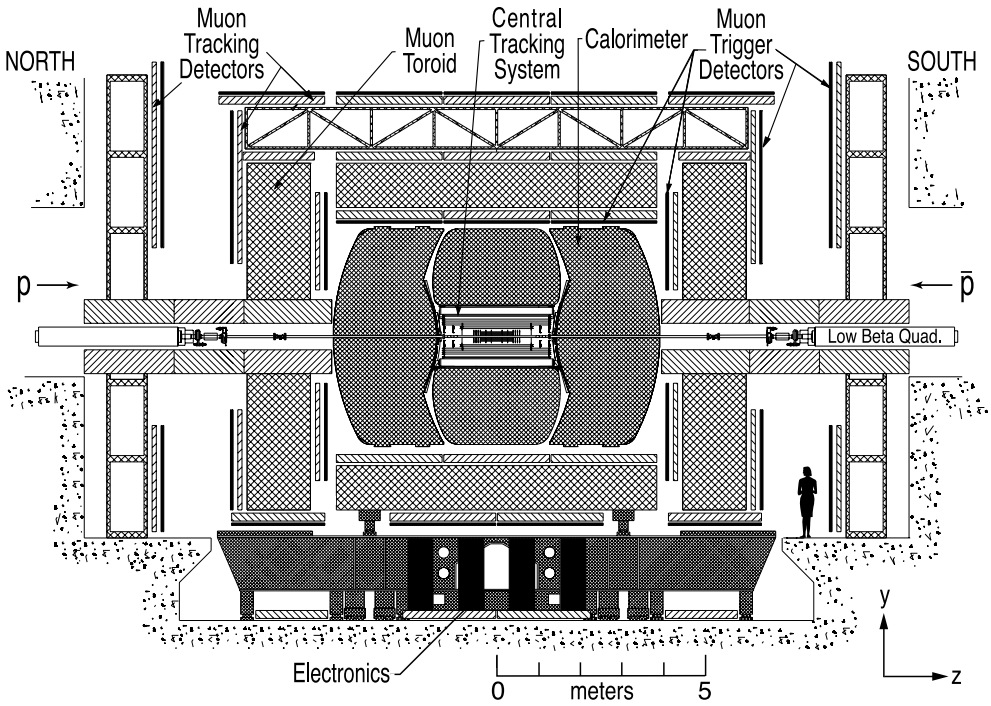

Figure 2.1: *A schematic overview of the DØ detector. The different subsystems are indicated.*

2.2.1 Coordinate system

In DØ a right-handed coordinate system with its origin at the nominal interaction point at the centre of the detector is used. The positive z-axis coincides with the beam line in the direction of the protons. The positive y-axis points upwards and the x-axis points away from the centre of the Tevatron ring. The polar angle θ is the angle with respect to the positive z-axis and the azimuthal angle ϕ the angle with respect to the positive x-axis in the xy-plane. We also make use of pseudorapidity, η, defined as:

$$\eta \equiv -\ln\left(\tan(\theta/2)\right). \tag{2.1}$$

As a measure of the distance between two objects, a quantity often used is:

$$\Delta R \equiv \sqrt{(\Delta\eta)^2 + (\Delta\phi)^2}\,, \tag{2.2}$$

where $\Delta\eta$ and $\Delta\phi$ are the differences in η and ϕ, respectively.

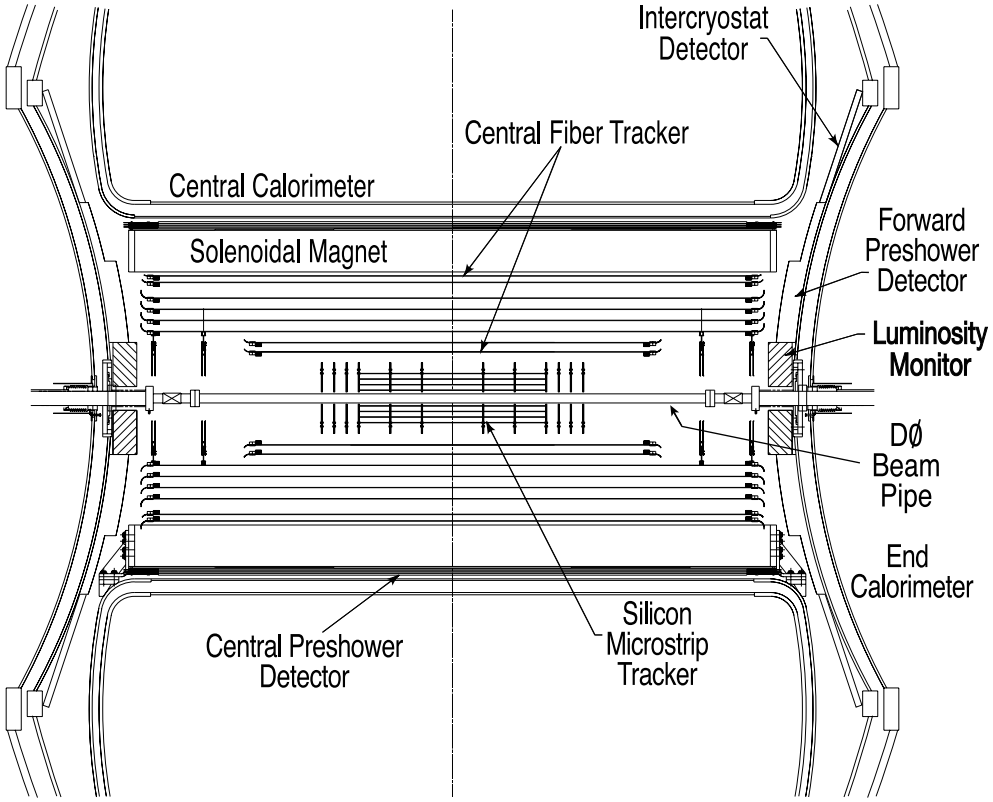

Figure 2.2: *A schematic overview of the DØ central tracking system.*

2.2.2 Central tracking system

The central tracking system consists of a silicon microstrip tracker (SMT) and a central fiber tracker (CFT) enclosed by a superconducting solenoid producing a 2 T magnetic field in the z-direction. A schematic overview of the central tracking system is shown in Fig. 2.2.

The solenoidal field

The SMT and CFT are enclosed in a superconducting solenoidal magnet in order to extract the momentum of charged particles from the measurement of the curvature of the tracks. The solenoid was designed to create a 2 T magnetic field using 4750 A of current.

To monitor the solenoidal field, a set of 48 Hall heads are located in the field

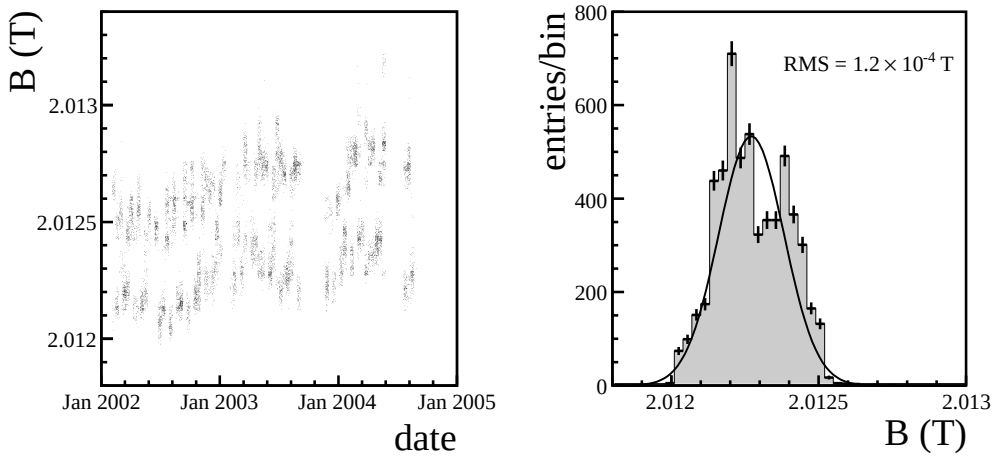

Figure 2.3: *The absolute value of the magnetic field as measured by the Hall head at $z = -1$ cm and $\phi = 337.5°$. The left plot shows the measurements as a function of time. The upper (lower) band corresponds to negative (positive) polarity of the field. The right plot shows the distribution of the measurements for positive polarities of the solenoid.*

volume. Thirty six are located on the inner bore of the solenoid cryostat. Six heads are mounted on each side on the faces of the barrel liquid argon cryostat. Each Hall head comprises three orthogonal Hall probes to measure the three components of the magnetic field and a temperature sensor. They are read out every hour.

The results obtained with the Hall probes confirm an earlier magnetic field measurement performed before the SMT, the CFT, and the calorimeter end caps were installed. They are also consistent with a computed field map.

To study the stability of the solenoidal field the data taken by the Hall heads from the start of Run II in 2001 until November 2004 are used. Figure 2.3 shows the measurements of a typical Hall head near $z = 0$. The root mean square variation at the level of 1.2 Gauss (0.06 ‰) as shown in Fig. 2.3 is comfortably small for this analysis.

Because of several quenches of the solenoid in the autumn of 2004, the current was lowered from 4749 A to 4550 A in November 2004. The magnetic field ought to scale down with a factor 0.9580. The ratio of the measurement of the magnetic field during the period November 2004–June 2005 and the magnetic field as observed before the current decrease is 0.9581, which is in agreement with the expectation and the precision of the magnetic field measurement.

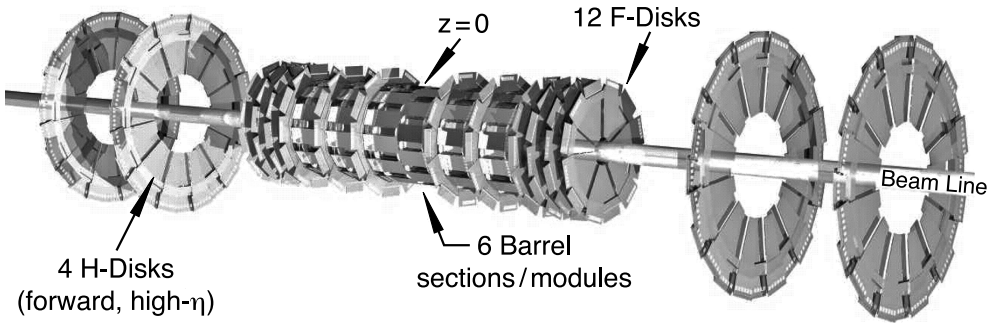

Figure 2.4: *A lay-out of the SMT with its six barrels, twelve F-disks, and four H-disks.*

Silicon Microstrip Tracker

The SMT consists of six barrels interspersed with twelve F-disks. It has two H-disks on either side as shown in Fig. 2.4. The barrel and F-disk assembly has a total length of 1.2 m with an inner radius of 2.7 cm and an outer radius of 10.5 cm. Each barrel consists of four layers of silicon sensors. The first and the second layer have twelve silicon modules in azimuth, called ladders. The third and the fourth layer both have 24 ladders. Each F-disk is equipped with twelve double-sided wedge shaped silicon modules (wedges). On each H-disk 24 wedges, each consisting of two single-sided 'half' wedges, are mounted. The pitch of the silicon read-out strips is between 50 μm and 153.5 μm in the barrels and between 50 μm and 80 μm in the disks.

The silicon is read out by 128-channel SVXIIe chips. These chips amplify the input signal, integrate the delivered current and digitize it with 8 bits. The silicon is operated at a temperature of 5° C. The SMT has 792, 576 read-out channels.

Central Fiber Tracker

The CFT has an inner radius of 20 cm and an outer radius of 52 cm and consists of eight concentric support structures on which scintillating fibers have been mounted. The two innermost cylinders are 1.66 m long. The other six are 2.52 m long. On each support cylinder two doublet layers are mounted. Each doublet layer consists of two layers of scintillating fibers. On every cylinder the orientation of the fibers in the innermost doublet layer is along the beam axis. These are called axial layers. The orientation of the fibers in the outermost doublet layer on each cylinder has a stereo angle in ϕ of $+3°$ or $-3°$. These are referred to as stereo layers. The first, third, fifth and seventh stereo doublet layers have a stereo angle in ϕ of $+3°$. The others have a stereo angle in ϕ of $-3°$. There is a total of 32 layers of scintillating fibers in the CFT. A doublet layer of the CFT has a spatial resolution in the r-ϕ plane of 100 μm.

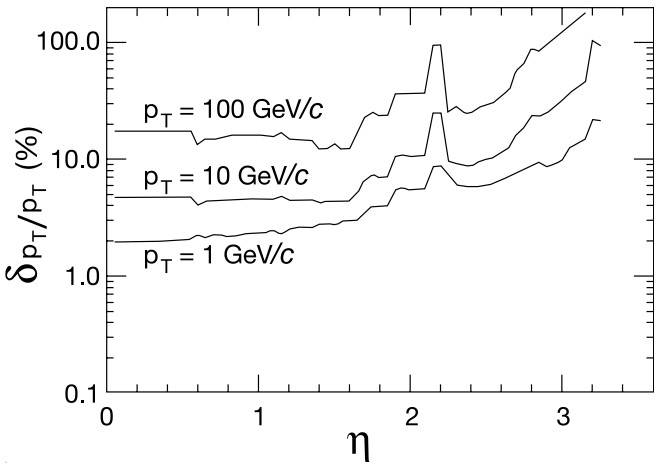

Figure 2.5: *The expected relative transverse momentum resolution of the central tracking system as a function of η for tracks with p_T =1, 10, and 100 GeV/c.*

Clear fiber waveguides transport the scintillation light to visible light photon counters for read-out. The CFT has a total of 76,800 read-out channels.

Figure 2.5 shows the expected track resolution of the central tracking system. The central tracking system reaches a resolution on the impact parameter of 15 μm at $\eta = 0$ for particles with a transverse momentum above 10 GeV/c.

2.2.3 Calorimeter system

The calorimeter, of which a cut-out view is shown in Fig. 2.6, consists of a central calorimeter (CC) ranging to $|\eta| < 1.1$, two forward calorimeters (FC) covering $0.7 < |\eta| < 4.2$, a massless-gap detector and an intercryostat detector. The central and forward calorimeters are all enclosed by their own cryostats, maintaining a temperature of 90 K. The calorimeters consist of an electromagnetic (EM) section, a fine hadronic (FH) section and a coarse hadronic (CH) section. The active material of the calorimeter is liquid argon. It is interspersed with absorber plates. In the EM and FH sections depleted uranium is used. In the CH sections copper is used in the central calorimeter and stainless steel in the forward calorimeters.

A slice of a quadrant of the calorimeter is shown in Fig. 2.7. Several read-out pads are grouped together to form a cell. The cells are ordered in layers. The EM section has four read-out layers. The fine hadronic section has three layers in the central calorimeter and four layers in the forward calorimeters and the coarse hadronic section has one layer. The cells are $\Delta\eta = 0.1$ by $\Delta\phi = 2\pi/64 \approx 0.1$ radians wide, except in the third EM layer, where the granularity is twice as fine in both η

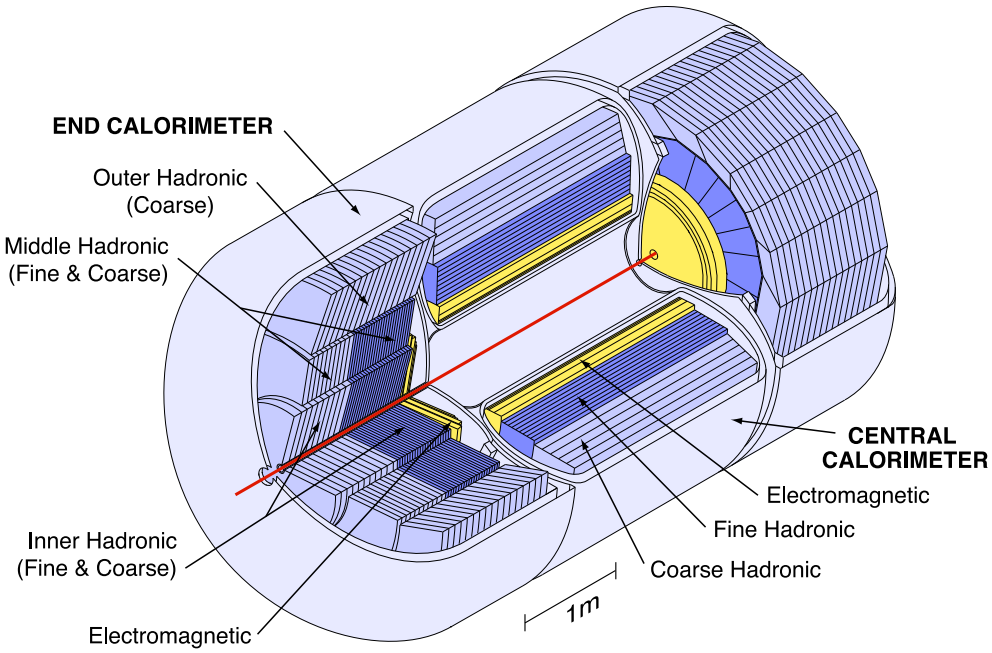

Figure 2.6: *A cut-out view of the calorimeter. Going outward from the interaction point, one can distinguish the electromagnetic section (light grey), the fine hadronic section (dark grey), and the coarse hadronic section (grey).*

and ϕ. Above $|\eta| = 3.2$ the cells are twice as large. Cells aligned in η and ϕ form a so called tower.

As can be seen from Fig. 2.7, in the region $0.8 < |\eta| < 1.4$ there is more inactive material early in the shower development than in the rest of the calorimeter due to the fact that both the central and the forward calorimeter are contained in their own cryostats. This region is called the intercryostat region (ICR). In order to improve the energy resolution in the intercryostat region extra sampling material has been added. This forms the massless-gap detector and the intercryostat detector (ICD). The massless-gap detector is a single-layer structure of calorimeter read-out cells located inside the central and end cryostats. The intercryostat detector consists of scintillator tiles mounted on the outside of the cryostat of the forward calorimeter.

The resolution, σ, of the energy measurement of the calorimeter is parametrized as a function of the energy, E, using a noise term, a sampling term, and a constant term:

$$\frac{\sigma^2}{E^2} = \frac{N^2}{E^2} + \frac{S^2}{E} + C^2 \,. \tag{2.3}$$

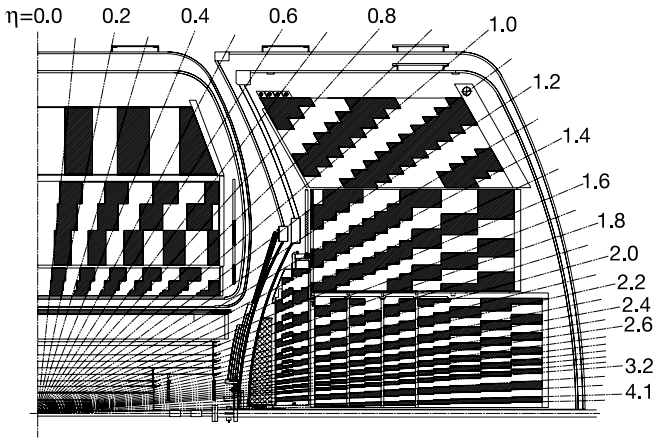

Figure 2.7: *A cross section of a quadrant of the calorimeter. The pseudo-projective read-out segmentation is indicated. The figure also shows the intercryostat detector (black line) mounted on the surface of the forward calorimeter cryostat at* $1.1 < |\eta| < 1.4$ *and the massless-gap detectors inside the central cryostat at* $0.8 < |\eta| < 1.2$ *and inside the forward cryostat at* $1. < |\eta| < 1.3$.

For photons and electrons $N = 0.14$ GeV, $S = 0.148\ \sqrt{\text{GeV}}$ and $C = 0.003$. For charged pions $N = 1.28$ GeV, $S = 0.446\ \sqrt{\text{GeV}}$ and $C = 0.039$.

In order to improve the electron identification and position measurement of energy depositions in the calorimeter a preshower is located in front of the calorimeter. The central preshower fills the gap between the cryostat of the solenoid and the central calorimeter with $|\eta| < 1.3$. The forward preshower covers $1.5 < |\eta| < 2.5$. The preshower consists of triangular scintillating strips and has 22,564 read-out channels.

2.2.4 Muon system

The muon system consists of a central muon system which ranges to $|\eta| = 1$ and a forward muon system which extends the coverage to $|\eta| = 2$. Each system comprises three multi-layers of drift tubes and scintillating counters. The drift tubes are proportional drift tubes (PDTs) in the central muon system and mini drift tubes (MDTs) in the forward muon system. The innermost multi-layer (A) has four layers of drift tubes. The two outer multi-layers (B and C) have three layers of drift tubes each. The presence of several layers within a multi-layer makes it possible to reconstruct a track segment within a multi-layer.

Due to the support structure of the calorimeter at the bottom of the detector, there is no full coverage of the central muon system. The central muon system has 55% coverage by PDTs from all three multi-layers and 90% coverage by PDTs from

at least two multi-layers.

An iron core toroidal magnet between the A multi-layer and the B multi-layer creates a field of 1.8 T. The innermost and the outermost multi-layers of the central muon system also contain scintillation counters of size $0.1 \times 4.5°$ in η and ϕ. These are used for triggering and cosmic muon rejection.

The transverse momentum resolution that can be achieved with the muon system is so much worse than the resolution of the track transverse momentum measurement obtained with the central tracker that only the latter is used for the momentum determination of muons.

2.2.5 Trigger system

The average bunch crossing rate is 1.7 MHz. With an event at each bunch crossing, it would be impossible to record every event on tape. Therefore, while taking data, a fast decision is made whether an event is interesting enough to be recorded. This is done by three levels of triggers, of which Fig. 2.8 shows a schematic overview. The first trigger level (L1) is a hardware trigger. It reduces the event rate from 1.7 MHz to 2 kHz. The rate of 2 kHz is the input for the second level (L2), which reduces the rate to 1 kHz. The third level (L3) brings this back to 50 Hz of data which are stored on tape to be analyzed.

If the output rate of any of the trigger levels is too high at a certain luminosity, a trigger can be prescaled, which means that the trigger accepts at L1 for certain triggers are scaled down.

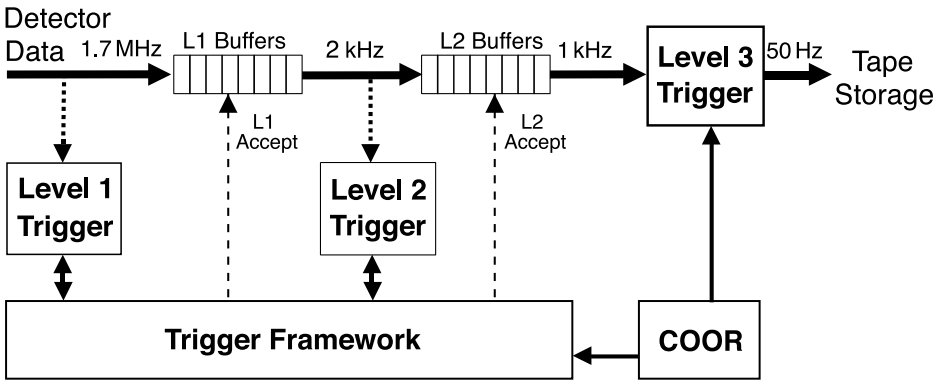

Figure 2.8: *A schematic overview of the trigger system, with its three layers of triggering from left to right. COOR is the program that coordinates the trigger framework.*

First trigger level (L1)

The first trigger level is a hardware based trigger. It uses the hardware information from the detector subsystems to coarsely reconstruct physics objects. The presence of such objects or combination of objects sets a particular L1 term. If any of the L1 conditions is met, the event is accepted and sent to level 2 (L2). The combination of L1 terms is done by the trigger framework, a designated computer system. The L1 trigger system temporarily stores every event in a large buffer. This way the time to decide whether to accept an event is increased to 3.3 μs. L1 causes a dead time of approximately 5% due to the read-out time of especially the silicon.

Level 1 central track trigger The L1 central track trigger (L1CTT) combines inputs from the axial layers of the CFT and the central and forward preshowers to form tracks. While optimized for making fast L1 trigger decisions, the electronics also store more detailed event data such as sorted lists of tracks and preshower clusters to be used later at L2 and L3 or as seeds for other trigger systems.

Level 1 calorimeter trigger The L1 calorimeter trigger combines 2×2 calorimeter cells to form L1 towers with a size of 0.2×0.2 in η and ϕ. An L1 tower contains either only the energy deposited in the electromagnetic section of the calorimeter or the energy deposited in both the electromagnetic and the fine hadronic sections. The coarse hadronic section is not used at L1. A typical L1 calorimeter term requires a certain number of towers with an energy deposition above a threshold.

The input for the L1 calorimeter trigger follows a different path than the signal used for precision read-out. The input for the L1 calorimeter trigger is split off from the read-out of the calorimeter information after it is amplified, but before it is shaped. It is digitized separately.

For the largest part of the data used in this analysis the L1 calorimeter trigger was operational up to $|\eta| < 3.2$, but for a small subset of the data taken at an early stage, it was operational up to $|\eta| < 2.4$ only.

Level 1 muon trigger The L1 muon trigger uses information from the muon system and L1CTT. It either matches central tracks with muon scintillation hits or it matches scintillation counter confirmed drift tube tracks from different muon layers. In order to reject cosmic muons, the coincidence of two scintillation counters must be within a restricted time window.

Second trigger level (L2)

At level 2 more information is available to reconstruct objects in different detector subsystems. At a global level an L2 processor, called L2Global, combines these reconstructed objects and might accept an event based on preset trigger conditions. Events

are stored in a 16 events large buffer. The total decision time of L2 is approximately 100 μs. The dead time due to L2 is negligible. The L2 preprocessors are described separately.

Level 2 silicon track trigger The L2 silicon track trigger (L2STT) preprocessor takes reconstructed tracks from the L1CTT and refits those including SMT hits.

Level 2 central track trigger The L2 central track trigger (L2CTT) preprocessor can take inputs from the L1CTT or L2STT. It refits the tracks adding information from the CFT and the preshower. The L2CTT sends sorted lists of tracks and clusters to other L2 preprocessors and to L3.

Level 2 calorimeter trigger The L2 calorimeter (L2Cal) preprocessor identifies jets and electrons or photons and calculates the $\not\!\!E_T$, which is described in Section 3.2.5, per event. As input it takes the calorimeter trigger towers.

The jet algorithm clusters 5×5 trigger towers centered around a seed tower coming from a list of sorted seed towers with $E_T > 2$ GeV. A list of jet candidates is passed to L2Global which applies jet requirements.

The electron/photon algorithm defines an E_T-ordered list of EM towers with $E_T > 1$ GeV. For each seed tower the neighbouring tower with the largest E_T is combined with the seed to make an EM cluster. The ratio of the transverse energies of these two towers and the total E_T in a 3×3 tower array surrounding the seed tower are used to reduce background. The list of electron/photon candidates is passed to L2Global where trigger requirements are applied to them.

The $\not\!\!E_T$ is calculated from the vector sum of the E_T of the trigger towers. This is done for different minimum values of E_T and different η ranges.

Level 2 muon trigger The level 2 muon (L2Muon) preprocessor forms muon candidates from the level 1 muon trigger and the muon system itself. Due to the availability of calibration and timing information the track quality is better than at L1.

Third trigger level (L3)

If an event has been accepted by L2, it is sent to L3 where, on a collection of processors, a limited event reconstruction is performed with reconstruction code similar to the code used for offline reconstruction. This reconstruction takes approximately 50 ms per event. After this reconstruction, events are accepted if they fulfil certain requirements for specific physics channels. The specific trigger conditions relevant for this analysis are described in chapter 4. L3 has a negligible dead time.

Chapter 3

Event simulation and reconstruction

To test and calibrate the analysis described in this thesis, simulated events are needed. To produce these events, a so called Monte Carlo technique, which is described in Section 3.1 is used. The reconstruction of physics objects from the detector measurements is described in Section 3.2. The goal of the event reconstruction is to reconstruct all the physics objects in the event as accurately as possible, while at the same time the effects of noise are minimized. Section 3.3 describes the smearing of reconstructed objects in Monte Carlo events.

3.1 Monte Carlo simulation

In the analysis described in this thesis, Monte Carlo events are used for several purposes. The generation of particles in Monte Carlo events encompasses the simulation of the hard scattering process, the showering of the incoming and outgoing partons, the hadronization of the partons and the decay of unstable resonances [44].

For semi-leptonic $t\bar{t}$ events, the simulation of the hard process is done using version 6.2 of the Monte Carlo generator Pythia [45]. One of the W bosons is forced to decay leptonically and the other hadronically. A set of hypothetical top quark masses of 155, 160, 165, 170, 180, 185, 190 and 195 GeV/c^2 is selected for the generation of Monte Carlo events. The parton distribution functions in Eq. 1.9 are the CTEQ6L distributions taken from the program LHAPDF [46]. The parton shower, which splits the incoming and outgoing partons according to splitting functions, the hadronization and the decay of unstable particles are also modelled by Pythia.

The main source of background in the data sample comes from events where a W boson is produced in association with four or more jets. The hard process of these

events is simulated by version 2.10 of the Monte Carlo generator ALPGEN [47]. The W boson is forced to decay leptonically. For showering, hadronization and particle decays of these events, Pythia is used again.

If a gluon from either ISR or FSR is sufficiently energetic, and well separated from the parton it is radiated from, it gives rise to an additional jet in the event. The simulation of additional energetic gluons can be described either by computation of the matrix element for the hard process with an additional hard gluon or by using the afore mentioned technique based on parton showers. The matrix element for the hard process with additional gluons contains the interference terms. When the additional gluons are generated by the showering of the partons, however, these interference terms are not accounted for [48]. Therefore, it is better to have the matrix element computed for the hard process plus additional gluons instead of having them generated by the showering. To obtain a consistent sample of W+jets Monte Carlo events, the samples in which a W boson was generated together with 1, 2, 3, 4, and 5 additional partons, are combined, using the so called MLM matching [49] procedure to avoid double counting.[1]

Both ALPGEN and Pythia compute matrix elements at leading order (LO), meaning that they only take Feynman diagrams into account that contain the minimum number of vertices necessary for the desired final state. Higher order matrix elements may lead to a different fraction of events in which a W boson is generated together with two b quarks or two c quarks, plus light (non-c and non-b) partons in the W+jets background sample. A comparison of the Monte Carlo sample with data events shows that the ALPGEN generator underestimates the fraction of events in which a W boson is generated together with two b quarks or two c quarks, plus light (non-c and non-b) partons [50]. The event weights of these Monte Carlo events are multiplied by a heavy flavour scale factor of 1.17 to account for this effect.

The detector response to the particles is simulated by letting the Monte Carlo generated particles pass through a detector simulation. The detector response is simulated with the program dØgstar, which uses the GEANT package [51].

The event generation in Monte Carlo only simulates a hard scatter. On top of this in data events there are multiple interactions per beam crossing, pile-up of energy from previous beam crossings, and noise. To add these effects to the Monte Carlo simulation, minimum-bias events are overlaid on the Monte Carlo. A minimum-bias event is an event triggered on by the luminosity counters, indicating a soft interaction. The number of inelastic scatters per beam crossing follows a Poisson distribution. At an instantaneous luminosity of 10^{32} cm^{-2}s^{-1}, which was often reached during the recording of the data used for this analysis, the mean of this distribution is 3.5.

[1] The phase space filled by the sample generated with computation of the matrix element of W boson production plus one hard parton is also occupied by the sample generated with the computation of the matrix element of the production of only a W boson with an additional hard parton generated by the hadronization. To avoid double counting events with additional partons generated by the hadronization above a scale which are well separated from jets are removed. The samples are then combined using event weights.

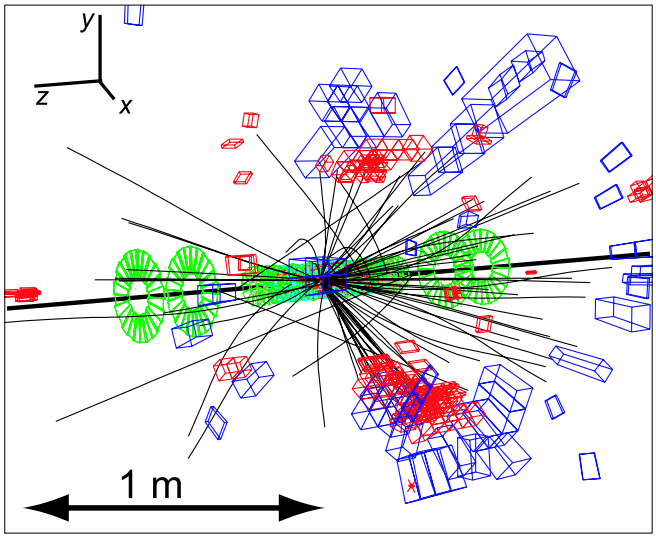

Figure 3.1: *Event number 3501889 from data taking run 193796 (a $t\bar{t}$ candidate event). Shown are the beam pipe (thick black line), the reconstructed tracks (black lines), the SMT geometry (grey lines) and the calorimeter cells with deposited energy above 0.2 GeV.*

3.2 Event reconstruction

Figure 3.1 shows an example of a data event. It shows the beam line, the SMT geometry, reconstructed tracks, and calorimeter cells with energy depositions above 0.2 GeV. The reconstruction of the physics objects used in this analysis is described in the following sections.

For the reconstruction of physics objects version `p17.09` of the standard DØ reconstruction software is used.

3.2.1 Muon reconstruction

Muons are identified with the tracking system and the muon system, but their transverse momentum is measured with the central tracker only. The event shown in Fig. 3.1 contains a muon. The information this muon leaves in the detector is shown in Fig. 3.2. The following requirements, which are described in detail in Ref. [52], are imposed on muons:

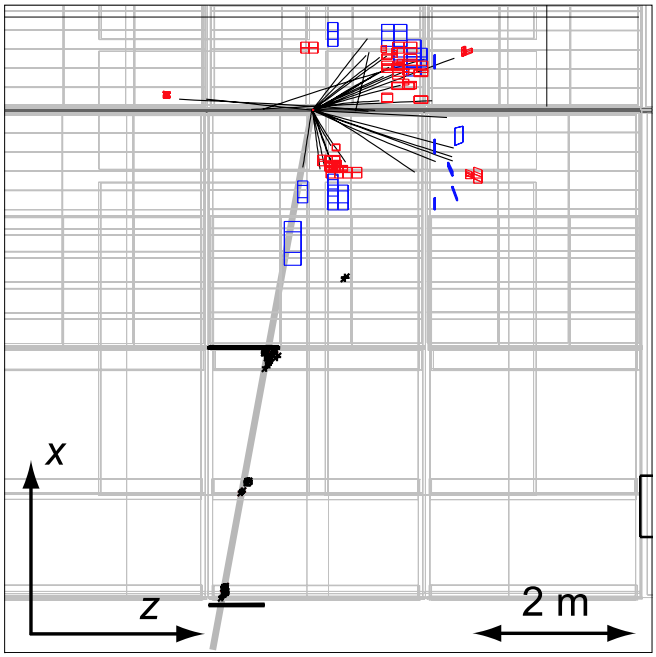

Figure 3.2: *The reconstructed isolated muon in the data event shown in Fig. 3.1 is here indicated with the thick light grey line. The beam pipe is indicated with the horizontal thick grey line. The plot shows the reconstructed tracks in the inner tracker and the scintillator and PDT hits in the muons system. The muon has scintillator hits in the A and C multi-layers and PDT hits in all three multi-layers.*

- A muon is required to have matching track segments reconstructed in both the A multi-layer and at least one of the multi-layers behind the toroid;
- The timing information of the scintillator hits must be inconsistent with that of a cosmic ray muon;
- The track in the muon system is required to match a track in the central tracking system which points towards the event vertex.

For this analysis the muon (and also the electron) is produced by a decaying W boson and is expected to be produced with a relatively large opening angle with respect to other particles. Therefore, the following isolation criteria are used:

- The muon may not be inside a cone of $\Delta R = 0.5$ from a jet;

- The calorimeter transverse energy in a hollow cone $0.1 < \Delta R < 0.4$ around the muon must be less than 8% of the muon transverse momentum;
- The sum of the transverse momenta of all other tracks in a cone $\Delta R = 0.5$ around the muon must be below 6% of the muon transverse momentum.

3.2.2 Electron reconstruction

To reduce the effect of noise, calorimeter cells are removed for reconstruction of physics objects by the `T42` algorithm, if [53]–[55]:

- the cell has a negative measured energy;
- the cell has a measured energy below 2.5 σ^{cell}, where σ^{cell} is the energy corresponding to the measured width of the signal due to electronics noise;
- the cell has a measured energy below 4 σ^{cell} and does not neighbour a cell with a measured energy above 4 σ^{cell}.

An electron or a positron is expected to deposit most of its energy in the electromagnetic calorimeter in a narrow cone and to have a track in the inner tracker. An electron or positron candidate, reconstructed with calorimeter information with a simple clustering algorithm, must pass the following cuts to be identified as an electron/positron:

- an electron must deposit 90% of its energy in the EM layer of the calorimeter in a cone with radius $\Delta R = 0.2$ around the shower axis;
- the transverse and longitudinal shower shapes must be consistent with those expected for an electron, based on Monte Carlo events;
- a good spatial match between a reconstructed track in the inner tracker and the calorimeter energy deposition must be present;
- an electron must be isolated, i.e. the ratio of the energy in a hollow cone $0.2 < \Delta R < 0.4$ and the total electron energy may not exceed 0.15;
- a discriminant is constructed combining information used for the four requirements listed above with the impact parameter of the matched track with respect to the primary vertex and the number and p_T's of the tracks close to the electron candidate. The value of this discriminant is required to be consistent with expectation for high-p_T isolated electrons.

The energy of an electron is measured by the calorimeter only.

Figures 3.3 and 3.4 show an electron in a data event. The calorimeter cells in which the electron deposited energy are indicated with an arrow. The corresponding track in Fig. 3.3 is marked with the thick black line. The E_T of this electron is 81.2 GeV.

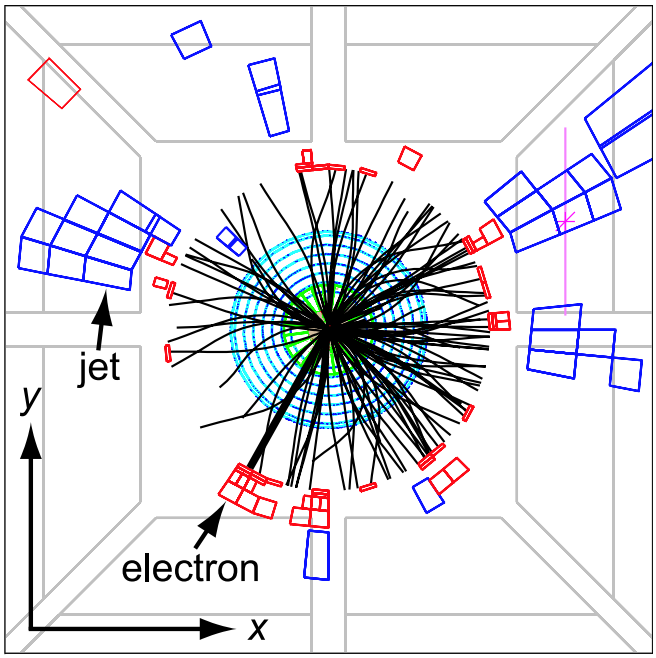

Figure 3.3: *A frontal view in the negative z direction of a data event containing an isolated electron and several jets. The calorimeter hits of the electron and one of the jets are indicated by the arrows. The track of the electron is indicted by the thick black line.*

3.2.3 Jet reconstruction

After noise reduction using the `T42` algorithm, jets are reconstructed using a cone algorithm with a cone radius of $\Delta R = 0.5$, as described in Ref. [56], and a minimum p_T of the seed of 0.5 GeV/c. The jet energy is measured with the calorimeter only. The raw jet p_T is required to be at least 6 GeV/c. To be identified as a jet, the jet candidate must pass a set of cuts, the choice of which is motivated in Ref. [57]:

- a cut on its coarse hadronic fraction (< 0.4), defined as the ratio of the jet energy deposited in the CH layer of the calorimeter over the total jet energy. This cut reduces the number of fake jets coming from electronics noise in the CH layer of the calorimeter. For specific η_{det} this value is adapted to optimize the reconstruction. η_{det} is the η of the jet in the calorimeter measured from the nominal interaction point at $z = 0$;

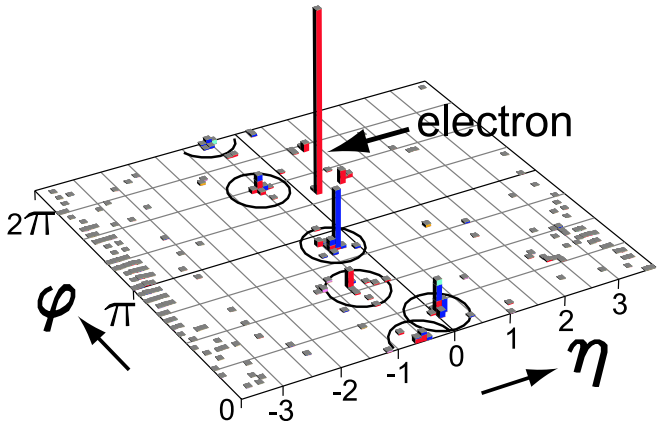

Figure 3.4: *A view of the calorimeter information in η-ϕ space of a data event containing an isolated electron.The calorimeter hits of the electron are indicated by the arrow. Several jets are also visible indicated by circles to guide the eye.*

- a cut on the electromagnetic fraction (> 0.05), defined as the ratio of the jet energy deposited in the EM layer of the calorimeter over the total jet energy. This cut reduces the amount of fake jets coming from electronics noise in the hadronic layers of the calorimeter. For specific η_{det} regions this value is adapted to optimize its effect;

- a cut on the ratio of the L1 trigger read-out and the precision read-out (> 0.05). If there is noise in the ADCs for the calorimeter precision read-out, the energy measurements in all channels connected to one ADC shift up coherently. The creation of jets by this coherent noise is reduced by comparing the precision read-out of the calorimeter with the L1 trigger read-out. The calorimeter read-out signal used for the L1 trigger is split off from the signal used for the precision read-out before it is digitized, so it is not affected by the noise in the ADCs which only affects the precision read-out. The variable $L1_{\text{ratio}}$ is defined as the ratio of the trigger and the precision energies of the jet, in which the energies (both from the trigger and the precision read-out) in the massless gap are not taken into account. In most regions an accepted jet is required to have $L1_{\text{ratio}} > 0.05$, but the cut is varied for specific η_{det} regions.

The event shown in Fig. 3.3 and 3.4 contains, apart from an electron, also several jets. In Fig. 3.4 these are indicated by the circles around the energy depositions. The

reconstructed jet indicated by the arrow in Fig. 3.3 has $E_T = 55$ GeV.

Jet energy scale

The raw jet energy is the calorimeter energy in a cone with $\Delta R < 0.5$. The raw jet energy is not equal to the energy of the original jet of particles in a 0.5 cone (the *particle jet*), due to several effects:

- **offset energy:** Multiple interactions, energy pile-up from previous bunch crossings, electronics noise and uranium noise 'deposit energy' (E_0) which does not come from the particle jet;
- **calorimeter response:** The calorimeter has a response (A_{jet} and R_{jet}) to the deposited energy in a cell, which is η dependent;
- **out of cone showering:** Particles enter or leave the jet cone due to e.g. showering in the calorimeter and bending in the magnetic field. The energy correction is R_{cone}.

The raw jet energy is corrected for these three effects in order to represent the particle jet energy. This correction is called the jet energy scale (JES) correction. The energy of the particle jet ($E_{\text{particle jet}}$) is obtained from the raw jet energy ($E_{\text{jet}}^{\text{raw}}$) as follows:

$$E_{\text{particle jet}} = \frac{E_{\text{jet}}^{\text{raw}} - E_0}{A_{\text{jet}} \times R_{\text{jet}} \times R_{\text{cone}}}\,, \tag{3.1}$$

The factors and offset in Eq. 3.1 are determined as described below:

Offset The offset is determined from minimum-bias events. These are events triggered by the luminosity counters, indicating the occurance of an inelastic collision. The average energy deposited per cell is computed. For a hypothetical jet at η_{det} with a cone size of $\Delta R = 0.5$ the total average energy deposited in that jet is calculated by summing over all average cell energies of the cells within the jet cone. This is done as a function of the number of vertices in the event to account for the instantaneous luminosity dependency of the offset;

Relative response correction The response of the calorimeter is not uniform in η_{det}. The relative response correction (R_{jet}) corrects the response to the response in the CC. It is determined with the Missing Transverse Energy Projection Fraction (MPF) method, which is a tag and probe method using photon+jet and dijet events. The tag object (a jet in the case of a dijet event and the photon in a photon+jet event) is required to be at $|\eta_{\text{det}}| < 0.5$. The probe jet may be anywhere. For photon+jet events at particle level the momentum of the photon, $\vec{p}^{\,\gamma}$, and the momentum of the hadrons, $\vec{p}^{\,\text{had}}$, must balance in the transverse plane:

$$\vec{p}_T^{\,\gamma} + \vec{p}_T^{\,\text{had}} = \vec{0}\,. \tag{3.2}$$

If one assumes perfect reconstruction of $\vec{p}^{\,\gamma}$, at detector level, $\vec{p}_T^{\,\gamma}$, the $\not\!\!E_T$ which is the missing transverse energy described in Section 3.2.5, and the momentum of the jet, which is the response factor times the momentum of the hadrons, must balance in the transverse plane[2]:

$$\vec{p}_T^{\,\gamma} + R_{\rm jet}\vec{p}_T^{\,\rm had} = -\vec{\not\!\!E}_T\,. \tag{3.3}$$

From these two equations it follows that the jet response is given by:

$$R_{\rm jet} = 1 + \frac{\vec{\not\!\!E}_T \cdot \vec{p}_T^{\,\gamma}}{|\vec{p}_T^{\,\gamma}|^2}\,. \tag{3.4}$$

A similar procedure is used for dijet events;

Absolute response correction For the determination of the absolute response correction ($A_{\rm jet}$), the MPF method is applied to photon+jet events after the application of the offset correction and the relative response correction. The selection requires a single photon with $|\eta_{\rm det}| < 1.0$ or $1.5 < |\eta_{\rm det}| < 2.5$ and at least one jet. The leading jet must be back-to-back with the photon in the transverse plane: $\Delta\phi_{\gamma,\text{leading jet}} > 3.0$. The absolute response is parametrized as a function of the transverse energy of the jet. This is done separately for data and Monte Carlo events;

Showering correction The showering correction ($R_{\rm cone}$) is determined for data and Monte Carlo events separately on photon+jet events with a single photon and exactly one jet. Only events with exactly one reconstructed primary vertex are selected to reduce the impact of multiple interactions. The average energy due to noise and pile-up is subtracted from the calorimeter energies. The procedure is performed for jets in bins of η and p_T. The first step in the determination of the showering correction is making a transverse energy density profile, $P^{\rm data}$, from the calorimeter towers as a function of the distance in rapidity-ϕ space to the jet axis. Also a transverse energy profile, $P^{\text{particle jet}}$, is created for all particles that belong to a particle jet in Monte Carlo events. The integral of the profile $P^{\text{particle jet}}$ is the particle jet energy. The same way a profile, $P^{\text{non}-\text{particle jet}}$, is created for all energy in Monte Carlo events not coming from particles of the particle jet. These are particles that bend or shower into the jet cone. The profiles $P^{\text{particle jet}}$ and $P^{\text{non}-\text{particle jet}}$ are fitted to the profile $P^{\rm data}$ to get the ratio of the true jet energy and the deposited jet energy in the jet cone. The same is done for jets in Monte Carlo events.

The JES used in this analysis is applied using `jetcorr v07.02.50`. It is different for data and Monte Carlo events. The version of the JES is a preliminary version.

[2]Note here that $\not\!\!E_T$ is computed by summing the calorimeter cell energies and not by summing the object energies.

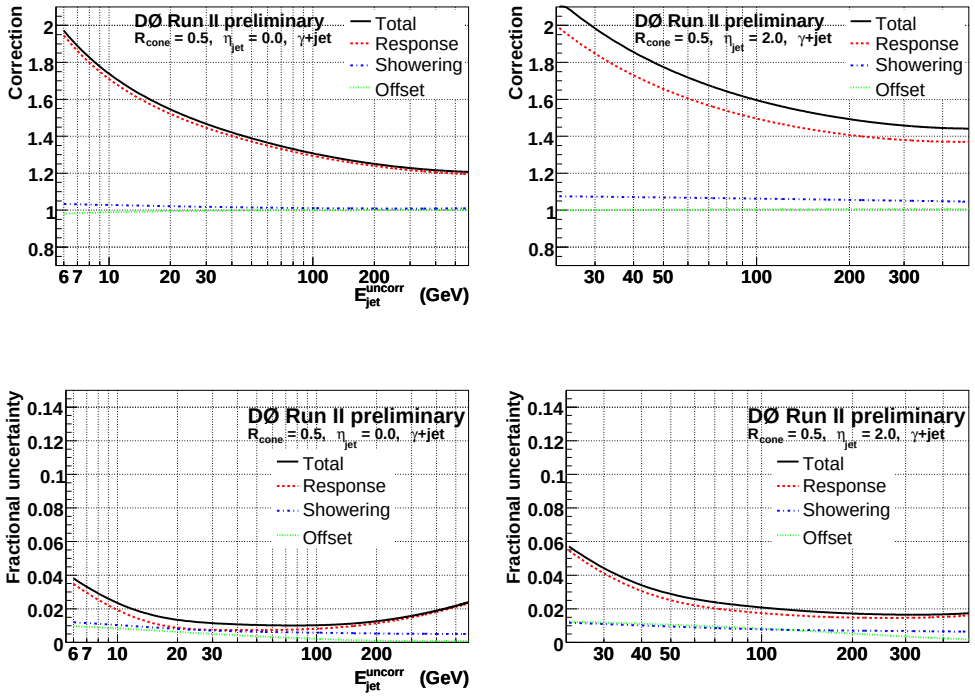

Figure 3.5: *The JES correction (upper plots) and the relative uncertainty on the JES (lower plots) for jets in data events with* $|\eta_{\text{det}}| = 0$ *(left plots) and* $|\eta_{\text{det}}| = 2$ *(right plots). The offset* E_0 *in Eq. 3.1 is here included in the multiplicative factor.*

Chapter 7 will describe how a systematic uncertainty is assigned for the difference between the final and the preliminary version of the JES. As an illustration, the JES for data and its relative uncertainty are shown in Fig. 3.5 for jets with $|\eta_{\text{det}}| = 0$ and $|\eta_{\text{det}}| = 2$.

3.2.4 *b*-Jet identification

Jets that originate from a b quark are called b jets. Among the particles produced by the hadronization of a b quark, a B hadron is formed. Due to their relative long lifetime, B hadrons travel typically several millimetres, before they decay. The tracks coming from the B hadron decay thus come from a displaced vertex. Figure 3.6 illustrates a displaced vertex in a b jet. The technique to identify b jets is called 'b

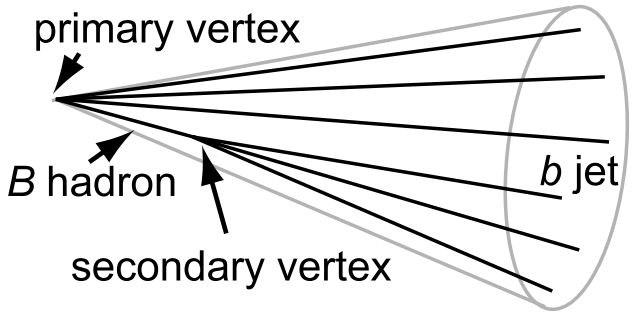

Figure 3.6: *A schematic view of a displaced vertex in a b jet.*

tagging'.

The neural network b tagging algorithm [58, 59] is used to identify jets containing B hadrons, or b jets. It uses as input variables:

- the decay length significance of the reconstructed secondary vertex, which is the distance between the primary and the secondary vertex in the x, y plane divided by its uncertainty;
- a variable based on the numbers of tracks with specific values of the track impact parameter significances;
- the probability that the jet originates from the primary vertex;
- the goodness-of-fit, χ^2, per degree of freedom of the secondary vertex;
- the number of tracks used to reconstruct the secondary vertex;
- the mass assigned to the secondary vertex;
- and the number of secondary vertices found in the jet.

The neural network b tagger combines these input variables to obtain an output per jet which is a value between zero and one.

Twelve operating points are defined. In this analysis operating point MEDIUM is used. If the output value of the neural network is higher than the value belonging to the operating point, the jet is tagged as b jet. For each operating point the tag rate function, which is the probability to tag a b jet, is parametrized as a function of the p_T and η of the jet. Also, the fake rate, which is the probability to assign a b tag to a non-b jet is parametrized as a function of p_T and η of the jet. Because hadrons

containing a c quark also live relatively long it is more probable to mistag a c jet than a jet without any c or B hadrons and there are separate fake rates for c jets and jets without B or c hadrons.

Not only by having a displaced vertex do b jets differ from non-c quark light jets, also by often containing a soft lepton in the jet. In 11% of the b jets the W boson from the B hadron decay decays directly to a muon and a neutrino. This percentage is increased by the potential successive decay of c quarks and muons from τ decays. The presence of soft muons in b jets is used in the procedure to determine the tag rate functions for the neural network b tagger, but is not used to tag b jets directly in this analysis.

If a muon is identified in a b jet, the jet energy is corrected for its presence. Furthermore, due to their different particle content, b jets could have a different energy response than light jets. In this analysis, no separate jet energy scale is applied to b jets: b jets are corrected with the inclusive jet energy scale described in Section 3.2.3. However, when computing the parton energies described in Section 5.2, separate corrections are derived for b jets and light jets. A possible systematic effect of the difference between light jets and b jets is incorporated in the systematic uncertainty.

3.2.5 Missing transverse energy

Neutrino's leave the detector undetected. However, the neutrino's transverse momentum is measured as the missing transverse energy ($\not\!\!E_T$), whose calculation is described in Ref. [60]. The missing transverse energy is the vector sum of the transverse energies of all the calorimeter cells excluding those in the CH section multiplied by -1. Only the transverse component has meaning, because energy escapes detection via the beam pipe in the longitudinal direction. This is the raw $\not\!\!E_T$. Two corrections are applied:

- muons deposit only a small fraction of their energy in the calorimeter, so the energy imbalance has to be corrected for the presence of muons in the event;
- cells in the CH section of the calorimeter are not taken into account for the calculation of the raw $\not\!\!E_T$. The raw $\not\!\!E_T$ is corrected for the energy that the jets deposit in the CH section;
- the $\not\!\!E_T$ is corrected for the JES and the EM energy scale applied to the jets and EM objects present.

3.3 Smearing of Monte Carlo objects

Due to approximations in the Monte Carlo simulations and especially the simulation of the detector material in dØgstar, observed physics objects in Monte Carlo events do

not always agree well with those in data events. Therefore, the following corrections are applied to Monte Carlo events:

- The hadronization of the b quarks and the energy and momentum fraction taken by the B hadrons are modelled by Pythia with the default Peterson b fragmentation scheme [61]. A b fragmentation parameter set has been tuned to describe the LEP e^+e^- data. This tuning is described in Ref. [62]. The Monte Carlo events are reweighted according to this tuned parameter set;

- Because the distribution of the instantaneous luminosity of minimum bias overlays in Monte Carlo events does not agree with the instantaneous luminosity distribution of the data set, the Monte Carlo events are reweighted to make the data and Monte Carlo distributions agree;

- Due to a simplified description of inactive material in the detector simulation of the Monte Carlo events and mis-alignments of the tracker, the resolution of reconstructed objects in Monte Carlo events is in general better than in data events. Therefore, energies and angles of jets, muons and electrons in Monte Carlo events are smeared to have the same resolutions as observed in data events [63]–[52];

- The jet identification efficiency is slightly higher in Monte Carlo than in data. Therefore, in Monte Carlo events jets are randomly removed to make the efficiencies agree;

- The Monte Carlo events are not selected by the trigger. To model the effect of triggering, Monte Carlo events get a weight, giving the probability that they would pass a trigger described in Section 4.1. For the determination of this weight, the efficiency for an object in an event to pass a requirement at a certain trigger level is parametrized. These parametrizations are called 'trigger turn-on curves'. The probability to pass a set of requirements is computed by multiplying the trigger turn-on curves.

The event weight distribution for a sample of approximately 27000 semi-leptonic $t\bar{t}$ events after the reweighting is shown in Fig. 3.7. Only event weights up to 4 are shown. There are some outliers, including three events with an event weight of approximately 70. These large weights are mostly due to the luminosity reweighting.

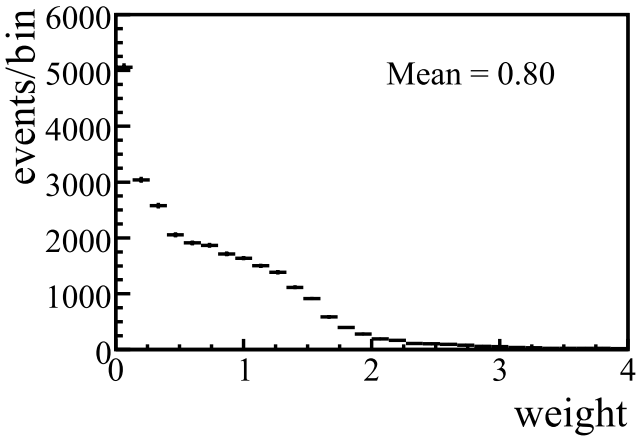

Figure 3.7: *The distribution of event weights of approximately 27000 semi-leptonic $t\bar{t}$ Monte Carlo events.*

Chapter 4

Data sample

Section 4.1 describes the selection of events, which aims to select the events useful for this analysis, while rejecting background events. In Section 4.2 the composition of the selected data sample is estimated and in Section 4.3 properties of the selected data events are compared with the prediction from Monte Carlo simulations.

4.1 Event selection

4.1.1 The semi-leptonic channel

For this analysis semi-leptonic $t\bar{t}$ candidate events are selected. The experimental signature of top quark pair events in the semi-leptonic channel consists of a highly energetic isolated charged lepton, large missing transverse energy arising from the neutrino escaping detection and at least four jets of which two are b jets. The event displayed in Figs. 3.1 and 3.2 is a candidate $t\bar{t}$ event. The calorimeter information in η-ϕ space of this event is shown in Fig. 4.1. The four jets indicated by the circles are clearly visible. Also the position and energy of the muon (at $\eta = -0.1$ and $\phi = 2.5$ radians) and the $\not\!\!E_T$ (at $\phi = 1.1$ radians) are shown in this plot. The jets at $\phi = 0.7$ radians and $\phi = 5.2$ radians have been b tagged and the first of these also contains a low-p_T muon. Figure 4.2 displays the same event again, but this time it is viewed in the direction of the negative z-axis.

Only events with an electron or a muon are considered. τ leptons are hard to reconstruct and have a poor energy resolution, which makes them less useful than electrons and muons. Events with tau leptons are discarded, but, if the tau lepton decays to an electron or a muon, they may contribute to the measurement as so called background.

There are other events with the same experimental signature as semi-leptonic $t\bar{t}$ events in which no top quark pair is present: the background events. The two main

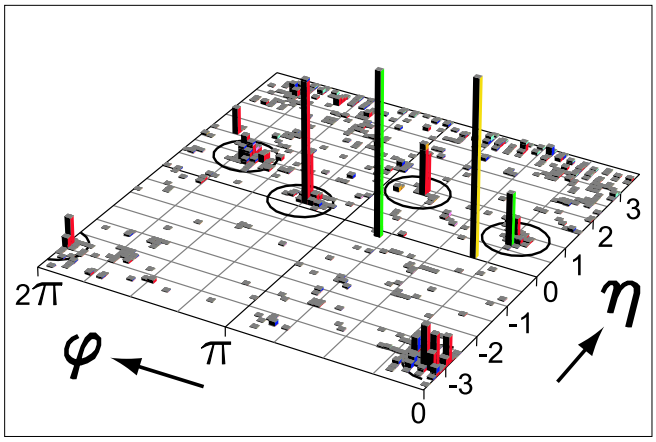

Figure 4.1: *The calorimeter information in η-ϕ space of a data event. The jets are marked with circles. The muon and $\not\!\!E_T$ are shown as the spikes at $\phi = 2.5$ radians and $\phi = 1.1$ radians, respectively.*

sources of background are W+jets events, in which a W boson is produced together with at least four jets with the W boson decaying leptonically, and QCD events, in which several jets are produced and one of the jets is mis-identified as an electron, or a charged lepton in a jet is reconstructed as an isolated lepton.

Muonic and electronic semi-leptonic decays constitute only 30% of all $t\bar{t}$ events, whereas 44% of the $t\bar{t}$ events decay fully-hadronically. However, there are two reasons why obtaining a large, pure sample of semi-leptonic events is easier than obtaining a large, pure sample of fully-hadronic events:

- The highly energetic isolated muon or electron in a semi-leptonic $t\bar{t}$ event provides a robust trigger signal;
- The background in the semi-leptonic channel is manageable. The main background in fully-hadronic events is formed by QCD events in which a large (≥ 6) number of jets are created. The cross section of this background overwhelmes the fully-hadronic $t\bar{t}$ cross section.

An additional advantage of the semi-leptonic channel over the fully-hadronic channel is that a mass analysis in the semi-leptonic channel is easier due to the smaller combinatorics when combining jets to compute a top quark mass.

One can obtain a high purity when selecting fully leptonic $t\bar{t}$ events, especially in the $\mu + e$ channel. The disadvantage of using fully leptonic $t\bar{t}$ events, however, is the limited statistics in that channel, due to the low branching fraction, as can be

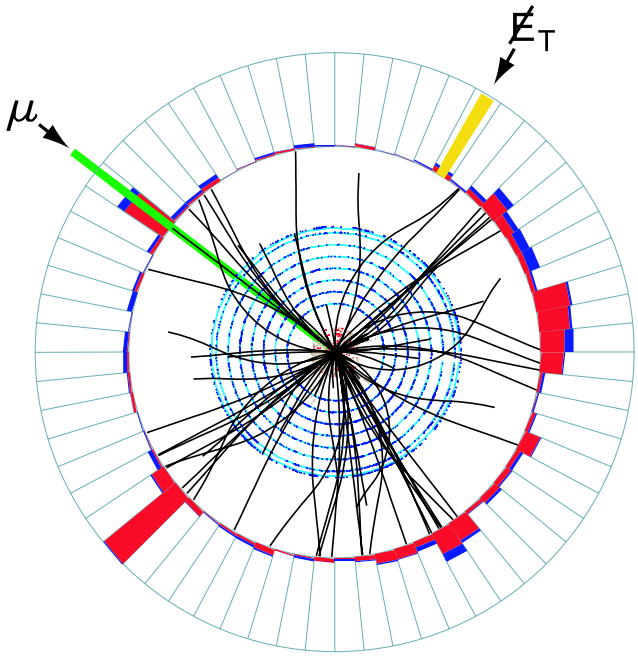

Figure 4.2: *Display of a data event passing the event selection. Shown are the reconstructed tracks and the energy deposited in the calorimeter. Calorimeter energy depositions aligned in ϕ are summed.*

seen in Fig. 1.5. Another disadvantage of the fully leptonic channel for a top quark mass analysis is the presence of two neutrino's, which complicates a mass analysis considerably.

4.1.2 Semi-leptonic event selection

The data used for this analysis were collected between August 2002 and February 2006 and correspond to approximately 1 fb^{-1} of integrated luminosity. To select a sample of semi-leptonic $t\bar{t}$ events with as little background as possible, an event selection is applied.

Only events firing one of the triggers described in Ref. [65] are selected. At L3 the triggers designed to trigger on e+jets events require at least one EM object with $p_T > 15$ GeV/c and at least two jets with $p_T > 15$ GeV/c or $p_T > 20$ GeV/c, depending on the time period. For some time periods there was a tighter requirement on

the most energetic jet. The μ+jets triggers require at least one medium muon at L2. During most time periods also a loose muon is required at L3, which in one trigger list was required to be isolated. At L3 the μ+jets triggers require at least one jet with $p_T > 20$ GeV/c, $p_T > 25$ GeV/c, $p_T > 30$ GeV/c, or $p_T > 35$ GeV/c, depending on the time period.

Quality requirements are imposed on the selected data. Runs or parts of runs in which detector systems essential to this analysis had problems or had significant noise are discarded. This procedure, which is described in Ref. [66], leaves 97.14% of the integrated luminosity. After application of the quality requirements the integrated luminosity of the data sample selected with the triggers described before is 1036 pb^{-1} for the e+jets sample and 994 pb^{-1} for the μ+jets sample.

To reduce the large amount of data, first a loose skim is applied by requiring at least one jet with $p_T > 15$ GeV/c and $|\eta_{\rm det}| < 2.5$, at least one loose electron or muon with $p_T > 15$ GeV/c, $\Delta R(\mu, \text{jet}) > 0.5$ (muon events only) and $\not\!\!E_T >$15 GeV. This loose skim is not applied to Monte Carlo events, but because the cuts in the event selection are more stringent than the cuts in the loose skimming of the data events, the skimming causes no discrepancy between the selection of data events and the selection of Monte Carlo events.

On the skimmed sample of events the following event selection is applied in order to obtain a sample enriched in $t\bar{t}$ events, but still of reasonable size:

- at least four jets with $p_T > 20$ GeV/c and $|\eta_{\rm det}| < 2.5$;
- exactly one isolated electron or muon with $p_T > 20$ GeV/c and $|\eta_{\rm det}| < 1.1$ for electrons or $|\eta_{\rm det}| < 2$ for muons;
- $\not\!\!E_T >$ 20 GeV;
- $\Delta\phi(\text{lepton}, \not\!\!E_T) > a \cdot \pi - b \cdot \not\!\!E_T$ with $a = 0.7$ (0.48) and $b = 0.045$ GeV^{-1} (0.033 GeV^{-1}) for electrons (muons).

The last two cuts remove much QCD background, which often has no $\not\!\!E_T$ or is low in $\not\!\!E_T$ with the $\not\!\!E_T$ pointing in the same direction as the charged lepton. There are also a number of selection cuts on e.g. the position of the primary vertex, which is required to have $|z| < 60$ cm. Apart from the isolation requirements described in Section 3.2.2 and 3.2.1, the distance between the lepton and the nearest jet, is also required to be larger than 0.5 in ΔR. These are all described in Ref. [67].

The selection cuts together with the number of events after each cut, the cut efficiency ε and the cumulative efficiency $\varepsilon^{\rm cum}$ can be viewed in Table 4.1 for e+jets events and in Table 4.2 for μ+jets events. In total, 446 electron and 409 muon events are selected. The event shown in Figs. 4.1 and 4.2 passes the event selection. Distributions of characteristics of these events are shown in Section 4.3.

Figures 4.3–4.5 show the distributions of several event variables of the selected events. The figures show the distribution of data events and the Monte Carlo predictions. The contribution of $t\bar{t}$, W+jets, and QCD events to the Monte Carlo prediction

cut	N_{evt}	$\varepsilon_{\text{data}}$ (%)	$\varepsilon^{\text{cum}}_{\text{data}}$ (%)	ε_{MC} (%)	$\varepsilon^{\text{cum}}_{\text{MC}}$ (%)
after skimming	1346749				
≥ 4 jets with					
$p_T \geq 15$ GeV/c and $\lvert\eta_{\text{det}}\rvert < 2.5$	22034	1.6	1.64	74.0	74.00
≥ 1 e with					
$p_T \geq 20$ GeV/c and $\lvert\eta_{\text{det}}\rvert < 1.1$	18080	82.1	1.34	7.7	5.70
μ veto	17572	97.2	1.30	98.7	5.63
second e veto	17501	99.6	1.30	99.5	5.60
PV selection	17501	100.0	1.30	98.4	5.52
$\not\!\!E_T \geq 20$ GeV	5448	31.1	0.40	88.7	4.89
triangular cut on $\Delta\phi(e, \not\!\!E_T)$ and $\not\!\!E_T$	2644	48.5	0.20	92.2	4.51
e is tight	1223	46.3	0.09	79.3	3.58
≥ 4 jets with					
$p_T \geq 20$ GeV/c and $\lvert\eta\rvert < 2.5$	446	36.5	0.03	73.4	2.63

Table 4.1: *The flow of e+jets events after each applied cut. Shown are the cuts, the number of events that pass the cut, the efficiency of the cut on data, $\varepsilon_{\text{data}}$, the cumulative efficiency on data, $\varepsilon^{\text{cum}}_{\text{data}}$, and the efficiency ($\varepsilon_{\text{MC}}$) and cumulative efficiency ($\varepsilon^{\text{cum}}_{\text{MC}}$) on semi-leptonic $t\bar{t}$ Monte Carlo with an input top quark mass of 170 GeV/c^2. The cut efficiency is the percentage of the number of events remaining after the cut(s).*

is described in the next section. Additional data – Monte Carlo comparisons are shown in Section 4.3.

cut	N_{evt}	$\varepsilon_{\text{data}}$ (%)	$\varepsilon^{\text{cum}}_{\text{data}}$ (%)	ε_{MC} (%)	$\varepsilon^{\text{cum}}_{\text{MC}}$ (%)
after skimming	234094				
≥ 4 jets with					
$p_T \geq 15$ GeV/c and $\lvert\eta_{\text{det}}\rvert < 2.5$	8198	1.3	1.26	73.7	73.66
≥ 1 medium isolated μ with					
$p_T \geq 20$ GeV/c and $\lvert\eta_{\text{det}}\rvert < 2$	3093	37.7	1.32	6.6	4.89
e veto	2986	99.9	1.32	98.9	4.83
second μ veto	2990	96.7	1.28	99.5	4.81
PV selection	2986	100.0	1.28	98.7	4.75
$\not\!\!E_T \geq 20$ GeV	1766	59.1	0.75	89.6	4.25
triangular cut on $\Delta\phi(\mu, \not\!\!E_T)$ and $\not\!\!E_T$	1239	70.2	0.53	90.9	3.87
μ is tight	918	77.0	0.17	86.6	3.35
≥ 4 jets with					
$p_T \geq 20$ GeV/c and $\lvert\eta\rvert < 2.5$	409	44.6	0.17	75.7	2.54

Table 4.2: *The flow of μ+jets events after each cut. Shown are the cuts, the number of events that pass the cut, the efficiency of the cut on data, $\varepsilon_{\text{data}}$, the cumulative efficiency on data, $\varepsilon^{\text{cum}}_{\text{data}}$, and the efficiency ($\varepsilon_{\text{MC}}$) and cumulative efficiency ($\varepsilon^{\text{cum}}_{\text{MC}}$) on semi-leptonic $t\bar{t}$ Monte Carlo with an input top quark mass of 170 GeV/c^2. The cut efficiency is the percentage of the number of events remaining after the cut(s).*

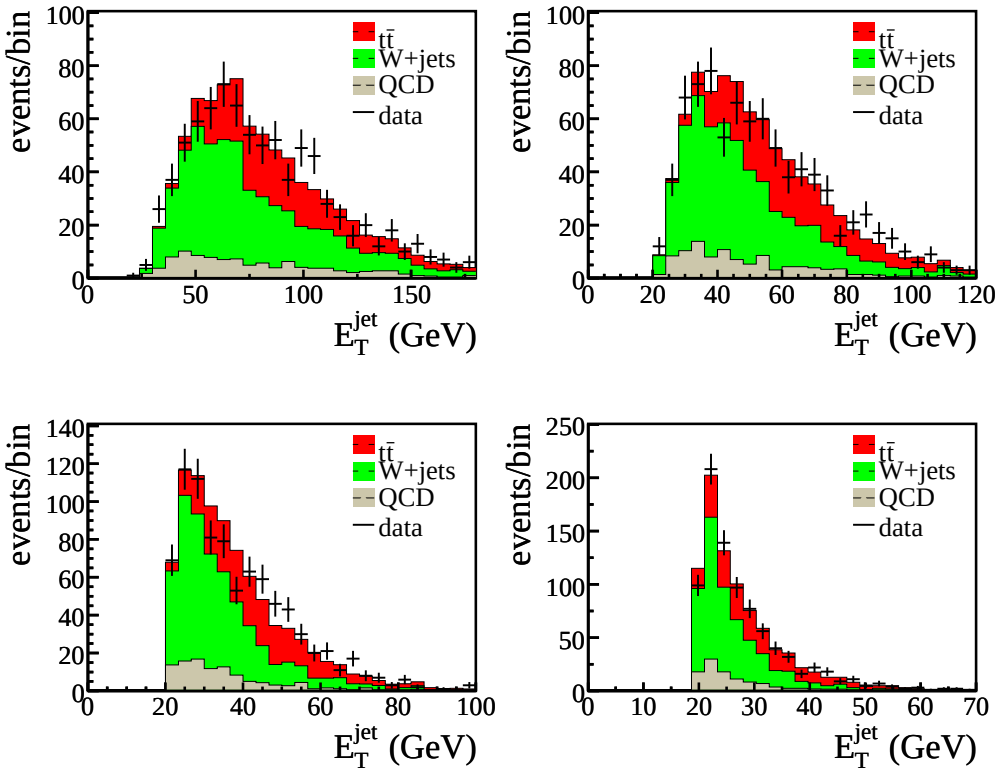

Figure 4.3: *Comparison of the distribution of the E_T of the leading (upper left), second leading (upper right), third leading (lower left), and fourth leading jet (lower right plot) between data and Monte Carlo events.*

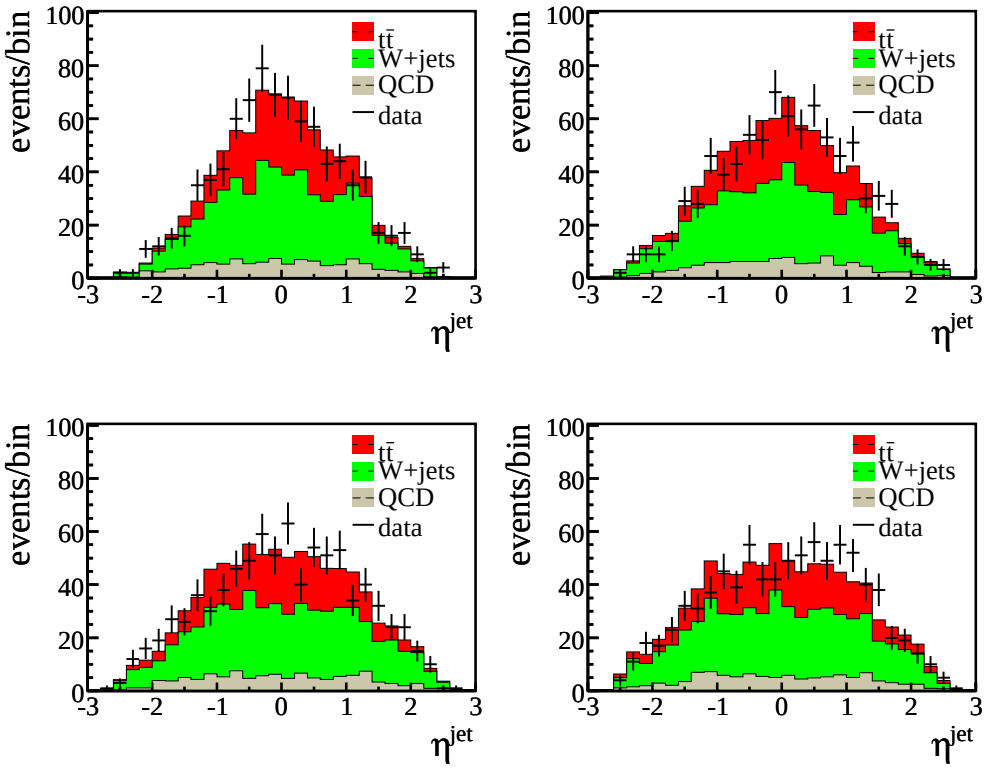

Figure 4.4: *Comparison of the distribution of η_{det} of the leading (upper left), second leading (upper right), third leading (lower left), and fourth leading jet (lower right plot) between data and Monte Carlo events.*

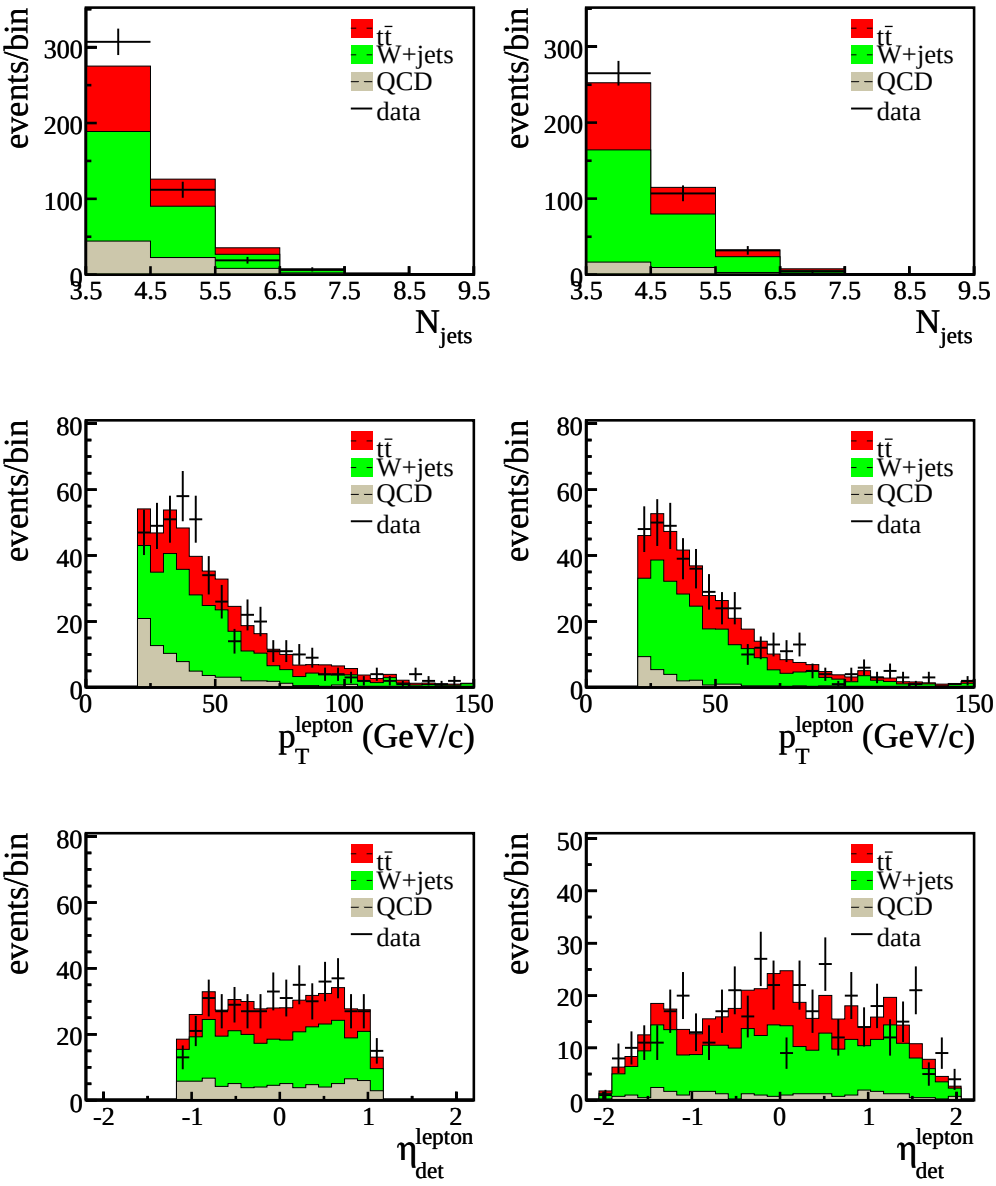

Figure 4.5: *Comparison of the distribution of the number of jets (upper row), the p_T of the lepton (middle row), and η_{det} of the lepton (bottom row) between data and Monte Carlo events for e+jets (left) and μ+jets (right).*

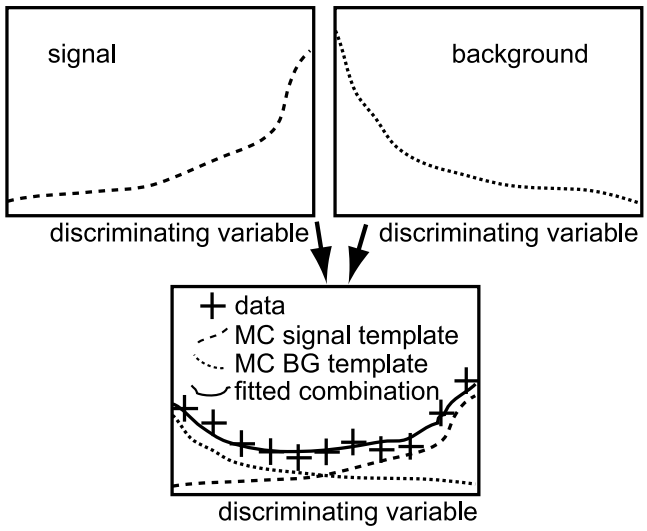

Figure 4.6: *A graphical illustration of the template fitting procedure to estimate the amount of signal and the amount of background in the data sample.*

4.2 Sample composition

For later purpose it is necessary to know how many $t\bar{t}$, W+jets, and QCD events the selected data sample contains. To estimate the sample composition, a template fit is performed. As an illustration, an example of a template fit is shown in Fig. 4.6. First, an event variable, which discriminates between signal and background events is searched for. This is called the discriminant. The distribution of the discriminant is plotted separately for signal and background Monte Carlo events. These two normalized distributions are used as templates: one for signal events and one for background events. The templates are fitted to the distribution of the discriminant observed in data, as illustrated in Fig. 4.6. The contributions of the two templates give the estimated amount of signal and background in the data sample.

In the following, the construction of the discriminant and the details of the template fit are explained in more detail.

4.2.1 Discriminant

The discriminant to be used in the template fit, is designed to differentiate between top quark pair events and background events. It uses six variables:

- aplanarity, which is defined as 3/2 times the smallest eigenvalue of the normal-

ized momentum tensor of the jets and the charged lepton [68];

- missing transverse energy, $\not\!\!E_T$;
- $H'_{T2} \equiv H_{T2}/H_{\parallel}$. This event variable measures the event centrality. H_{T2} is the scalar sum of the transverse momenta of the jets excluding the leading jet and $H_{\parallel}$ is the sum of the magnitudes of the longitudinal momenta of the jets, the isolated lepton and the neutrino. The longitudinal neutrino momentum is estimated requiring that the mass computed from the measured lepton momentum, $\not\!\!E_T$ and unknown longitudinal neutrino momentum is the mass of the W boson, 80.4 GeV/c^2. If more than one solution for $p_{\parallel}^{\nu}$ is found, the one smallest in absolute value is used;
- $K_T^{-\prime} \equiv (\Delta R_{ij}^{\min} \cdot E_T^{\text{lesser } j})/(E_T^W)$. This event variable is a measure of the jet separation normalized by the transverse energy of the reconstructed W boson. $\Delta R_{ij}^{\min}$ is the smallest distance in $\eta-\phi$ space between any two of the four leading jets. $E_T^{\text{lesser } j}$ is the smaller of the two jet E_Ts. The transverse energy of the W boson is defined as $E_T^W \equiv p_T^{\text{lepton}} + \not\!\!E_T$;
- absolute pseudorapidity difference of the two leading jets, $|\Delta\eta|$;
- number of b tagged jets (N_{tags}). In data the b tagging procedure as explained in Section 3.2.4 is used. Jets in Monte Carlo events are not b tagged directly. Instead, depending on the true jet flavour, f_i, the tag rate function or the fake rate is applied to the jet to assign a probability, $P^{f_i}(p_{T\,i}, \eta_i)$, that it is b tagged. For each event the probability is calculated that it has zero, one or two or more b tags according to:

$$P_{\text{event}}^{\text{tag}}(N_{\text{tags}} = 0) = \prod_{i=1}^{N_{\text{jets}}} (1 - P^{f_i}(p_{T\,i}, \eta_i)), \tag{4.1}$$

$$P_{\text{event}}^{\text{tag}}(N_{\text{tags}} = 1) = \sum_{j=1}^{N_{\text{jets}}} P^{f_j}(p_{T\,j}, \eta_j) \prod_{i=1; i\neq j}^{N_{jets}} (1 - P^{f_i}(p_{T\,i}, \eta_i)), \tag{4.2}$$

$$P_{\text{event}}^{\text{tag}}(N_{\text{tags}} \geq 2) = 1 - P_{\text{event}}^{\text{tag}}(N_{\text{tags}} = 0) - P_{\text{event}}^{\text{tag}}(N_{\text{tags}} = 1). \tag{4.3}$$

Figure 4.7 shows the distributions of the variables that are used in the discriminant. For the distributions of the $t\bar{t}$ and W+jets events, the $t\bar{t}$ Monte Carlo sample with an input top quark mass of 170 GeV/c^2 and the W+jets Monte Carlo sample are used. Monte Carlo simulation can, however, not be used for QCD events. Since the probability to misreconstruct a jet as an electron or to reconstruct a soft lepton in a jet as an isolated lepton is extremely small, a near infinite number of Monte Carlo events would have to be generated in order to obtain a sizable QCD background sample. Therefore, data events are used. The selection of the QCD events is equal to the

selection of $t\bar{t}$ events, except that for muon events the lepton isolation cut is inverted and for electron events the electron is required to be loose but not tight. With these cuts inverted the fraction of $t\bar{t}$ events in the sample is small. A data sample of 541 QCD events is selected.

The $t\bar{t}$ events look distinguishably different from the background events, which makes it possible to separate signal from background. The W+jets and QCD distributions look similar for most of the variables, but it is not critical to separate these two backgrounds for the purpose of this analysis. Because the distributions of the six variables look similar for W+jets events and QCD events, a discriminant constructed from these six variables will also be similar for the two sources of background and the discriminant cannot be used to fit the two sources of background separately. The solution to this problem is presented later, when the template fit is described.

The probability for a signal event to have value x_i for variable i is the corresponding distribution in Fig. 4.7, but normalized to unity. It is denoted by $s_i(x_i)$, or for readability s_i. Similarly, the probability for a W+jets event to have value x_i for variable i is the normalized corresponding distribution, which is denoted by $b_i(x_i)$ or b_i. If the variables are uncorrelated, the probability to observe a set of variables, $\{x_i\}$, in a signal event is:

$$S(\{x_i\}) = \prod_{i=1}^{6} s_i \,, \tag{4.4}$$

and for W+jets events it is:

$$B(\{x_i\}) = \prod_{i=1}^{6} b_i \,. \tag{4.5}$$

The discriminant is constructed so that it is the probability that an event with certain values for the six variables is a signal event, assuming that 50% of the events are $t\bar{t}$ events and 50% are W+jets events. Here, the presence of QCD events is ignored. The probability for an event with the set of six variables $\{x_i\}$ to be a signal event, is:

$$D = \frac{S(\{x_i\})}{S(\{x_i\}) + B(\{x_i\})} \,, \tag{4.6}$$

Substitution of Eq. 4.4 and 4.5 in Eq. 4.6 gives:

$$\begin{aligned} D &= \frac{\prod_i s_i}{\prod_i s_i + \prod_i b_i} \\ &= \frac{\prod_i s_i/b_i}{\prod_i s_i/b_i + 1} \,. \end{aligned} \tag{4.7}$$

Construction of the discriminant now boils down to finding parametrizations of s_i/b_i. Instead of parametrizing s_i/b_i directly, the ratio $s_i/(s_i + b_i)$, from which the former

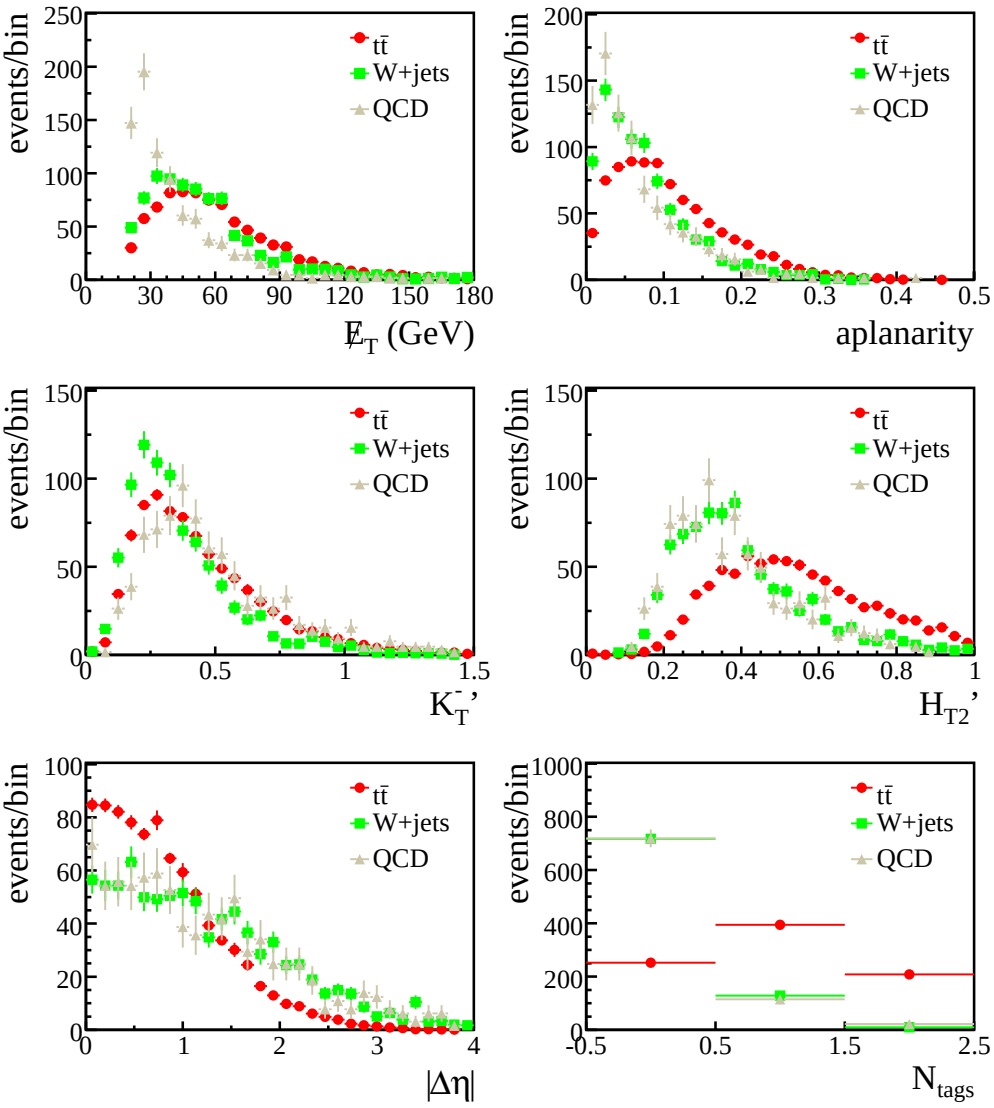

Figure 4.7: *Distributions of the variables used in the event discriminant (see text for their definition). Three samples are shown: $t\bar{t}$, W+jets and QCD. Each sample is normalized to the same number of observed events in data. The plots are for the combined samples of e+jets and μ+jets events.*

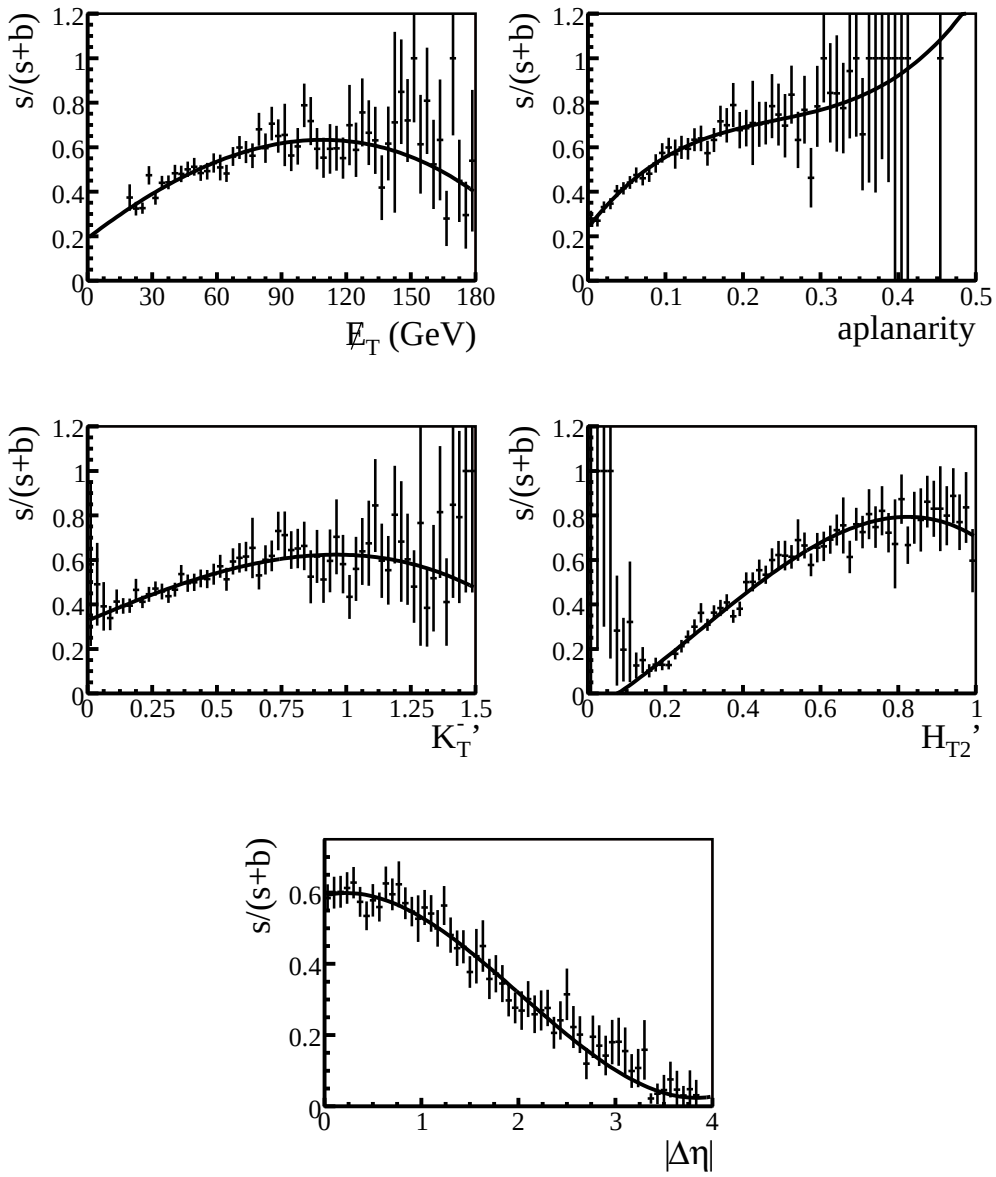

Figure 4.8: *Fits to $s/(s+b)$ for the event variables entering the discriminant (see text for details).*

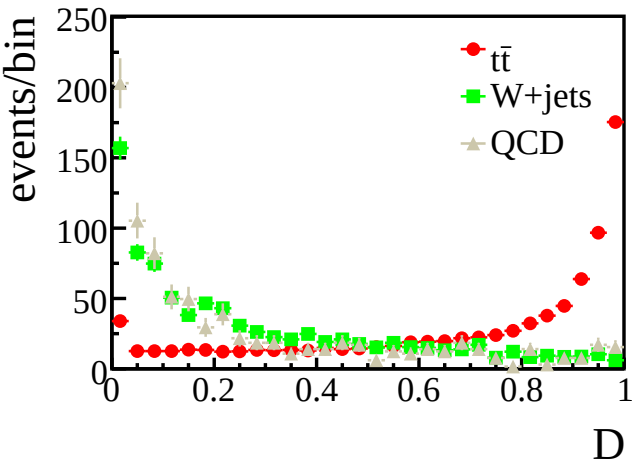

Figure 4.9: *Discriminant distributions for $t\bar{t}$, W+jets and QCD events. These distributions are for combined samples including μ+jets and e+jets events.*

ratio can be computed via a trivial transformation, will be parametrized. This is done because the ratio $s_i/(s_i + b_i)$ is bounded between 0 and 1 by construction.

The plots in Fig. 4.8 show fits to the distributions of $s/(s+b)$ for the five topological variables. The fit functions are third order polynomials. The fitted parametrizations instead of the actual distributions are used to form the discriminant. Especially for $\not\!\!E_T$, $K_T^{-\prime}$ and H'_{T2} the third order polynomials do not fit the distributions well in the high, the high and the low bins, respectively. However, these bins have low statistics as indicated by the large error bars and a perfect fit is not critical. The ratio $s/(s+b)$ cannot be larger than unity or smaller than zero. If the fit gets larger (smaller) than one (zero), it is set to this boundary value.

For the number of b tags, the ratio $s/(s+b)$ is 0.26, 0.75, and 0.96 for respectively 0, 1, and ≥ 2 b tags. These numbers are computed from Monte Carlo using Eq. 4.1, 4.2 and 4.3 and the tag rate functions.

The discriminant distributions for signal and backgound are shown in Fig. 4.9.

Equation 4.7 only gives a proper probability in case the variables x_i are uncorrelated. There are correlations between the variables x_i, which are listed in Table 4.3. To construct a probability from D, $P(D)$, the ratio $s(D)/(s(D)+b(D))$ is calculated, where $s(D)$ and $b(D)$ are the normalized signal and background distributions of the discriminant D, as shown in Fig. 4.9. $P(D)$ is shown in Fig. 4.10 as a function of D. Also here a third order polynomial is fitted to the distribution of $s(D)/(s(D)+b(D))$. The fitted polynomial is used to obtain the templates for the distribution of $P(D)$

	Aplanarity	$\not\!\!E_T$	H'_{T2}	$K_T^{-\prime}$	$\lvert\Delta\eta\rvert$
Aplanarity	1.000	-0.047	0.321	0.136	-0.308
$\not\!\!E_T$		1.000	-0.068	-0.068	-0.025
H'_{T2}			1.000	0.110	-0.406
$K_T^{-\prime}$				1.000	0.030
$\lvert\Delta\eta\rvert$					1.000

Table 4.3: *Correlation coefficients between the input variables of the discriminant.*

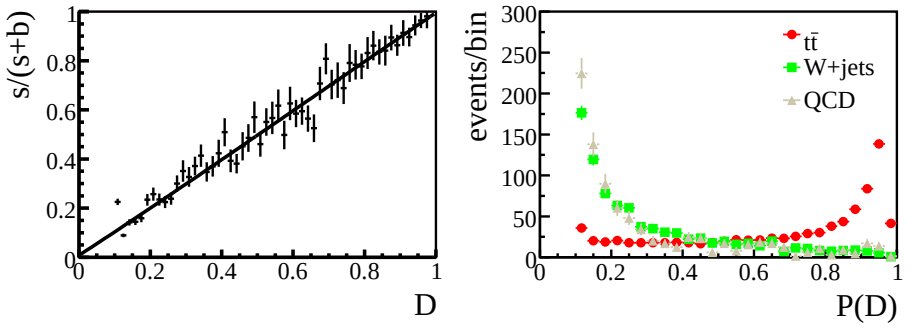

Figure 4.10: *A third order polynomial fit to the purity, $s(D)/(s(D)+b(D))$, as a function of D (left plot). This parametrization defines the discriminant probability, $P(D)$, used in the analysis. Templates of the discriminant probability, $P(D)$, used to fit the composition of the data sample (right plot).*

for $t\bar{t}$, W+jets and QCD events as shown in Fig. 4.10. As can be seen, there are no entries for $P(D)$ between 0 and 0.1. This is due to the fact that there is no set of variables x_i for which the purity is 0.

4.2.2 Estimation of the sample composition

The templates for the distribution of $P(D)$ for $t\bar{t}$, W+jets and QCD events, as shown in Fig. 4.10, are fitted to the distribution in data to estimate the sample composition. Because the distributions for W+jets and QCD events are similar, they cannot be fitted independently. The fraction of QCD in the data sample is taken from Ref. [69] and is 17.5% for e+jets, 7.3% for μ+jets and 12.6% for the combined channel. The cross section analyses described in Ref. [69] do not use the same jet energy scale as applied here. However, it is not expected that the minor differences change the

fractions of QCD significantly.

The fits are shown in Fig. 4.11 and Table 4.4 shows the fitted fractions. Note that the composition of the combined sample is an additional fit and not simply the sum of the e+jets and μ+jets channels.

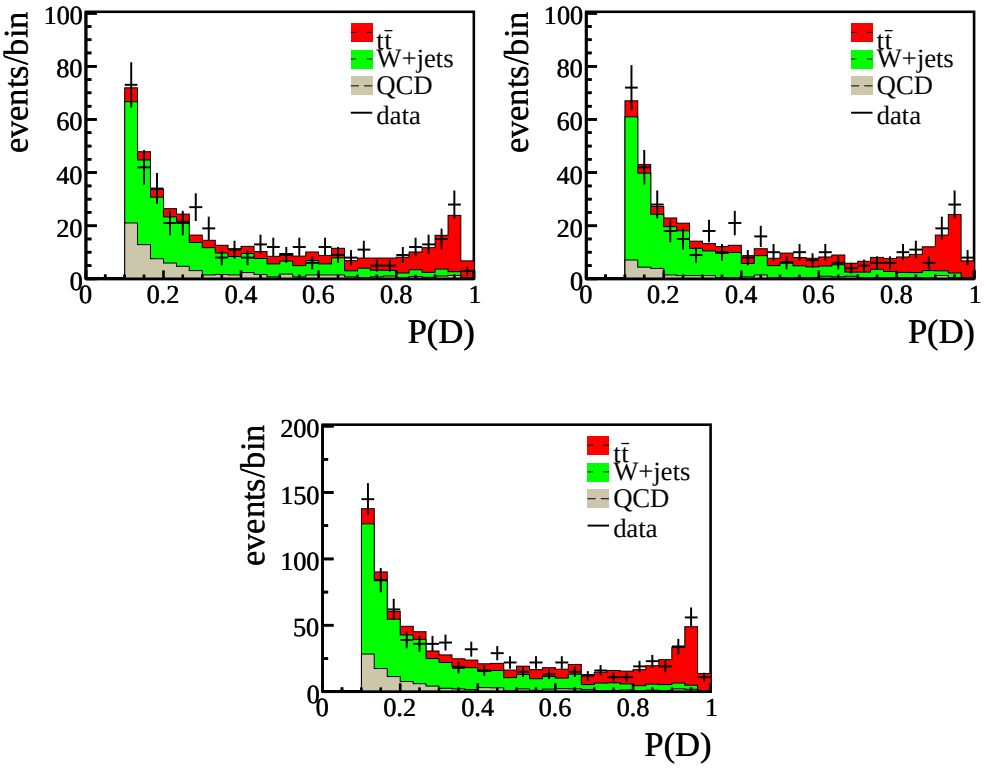

Figure 4.11: *Fit to extract the sample composition in data. The top left plot is for e+jets with the QCD template fraction fixed to 17.5%. The top right plot is for μ+jets with the QCD template fraction fixed to 7.3%. The lower plot is for the combined sample with the QCD template fraction fixed to 12.6%.*

	e+jets		μ+jets		combined	
$N_{\text{observed in data}}$	446		409		855	
$t\bar{t}$	136.5	(30.6%)	136.2	(33.3%)	277.0	(32.4%)
W + jets	231.5	(51.9%)	242.9	(59.4%)	470.3	(55.0%)
QCD	78.0	(17.5%)	29.9	(7.3%)	107.7	(12.6%)

Table 4.4: *Estimated composition of the data sample.*

4.3 Data and Monte Carlo comparison

For the Monte Carlo events to be useful for calibrating the analysis, it is important that distributions of (topological) quantities in data and Monte Carlo events agree. Figures 4.3–4.5 showed the agreement for several topological variables. Figures 4.12 and 4.13 show the agreement for the six variables used for the discriminant. The total number of Monte Carlo events is normalized to the number of events observed in data. The fractions are taken from Table 4.4. Within statistics the Monte Carlo simulation represents the data well.

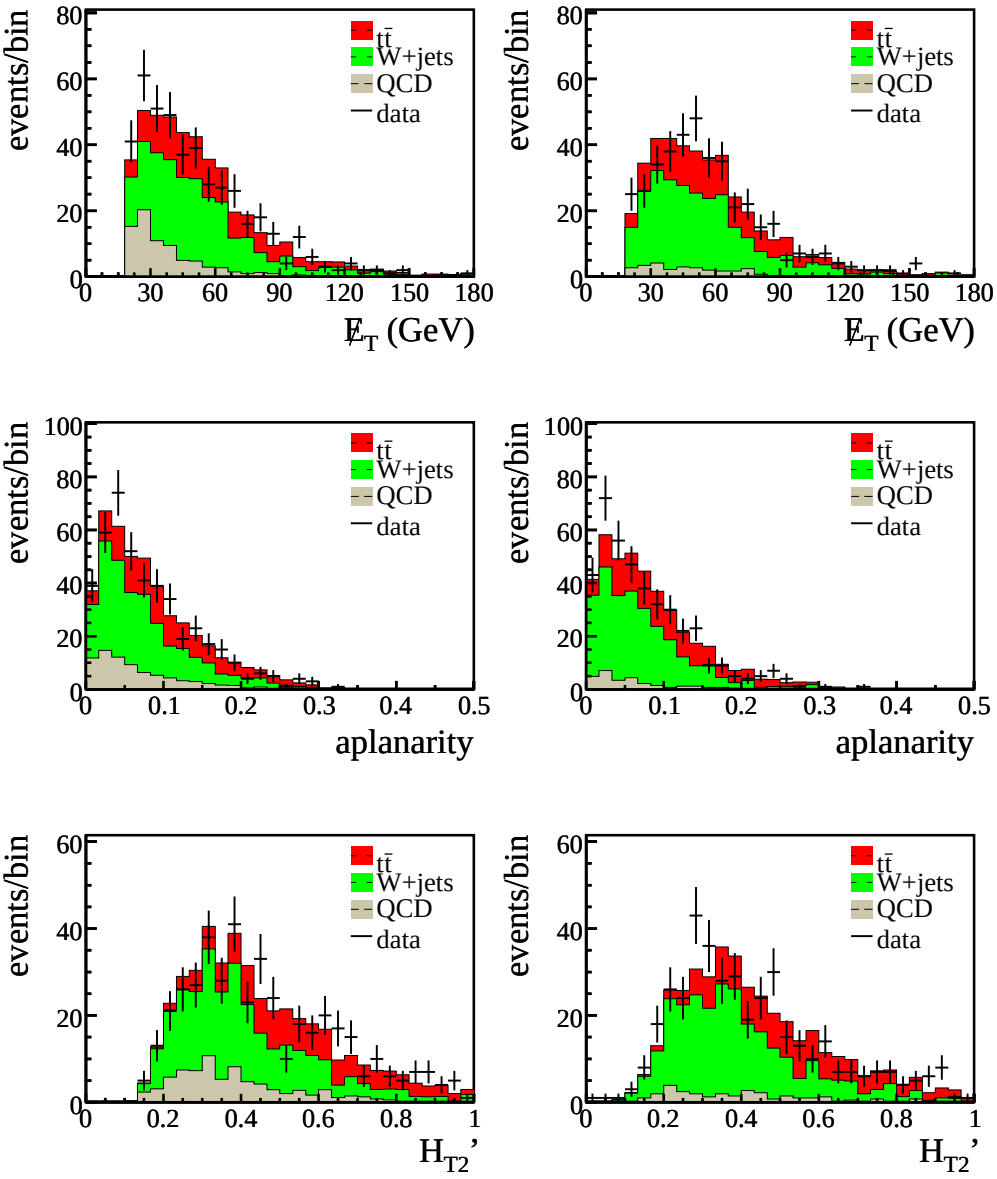

Figure 4.12: *Comparison of the distribution of $\not\!\!E_T$ (upper row), aplanarity (middle row), and H'_{T2} (bottom row) between data and Monte Carlo events for e+jets (left) and μ+jets (right).*

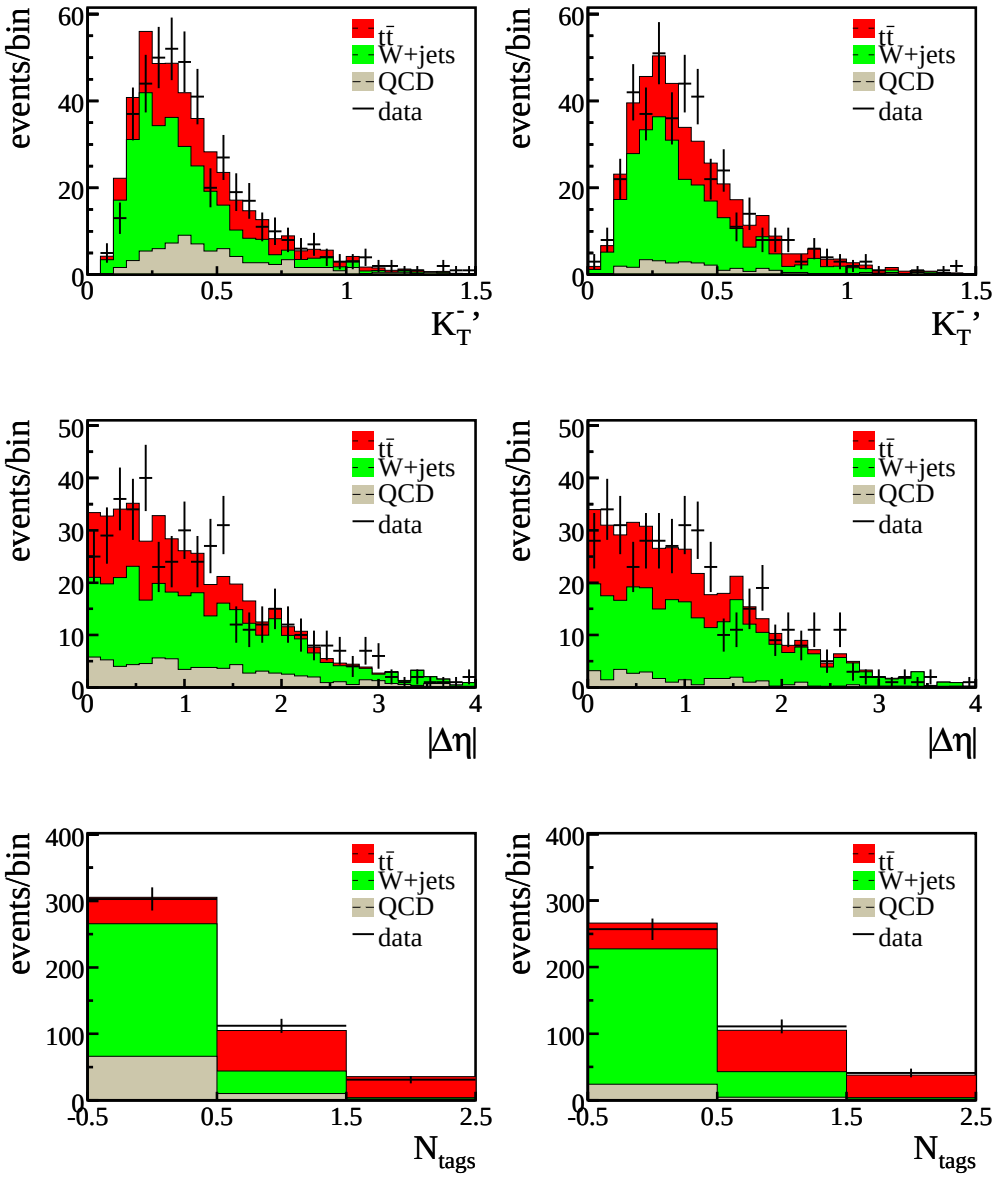

Figure 4.13: *Comparison of the distribution of $K_T^{-\prime}$ (upper row), $|\Delta\eta|$ (middle row), and the number of b tags (bottom row) between data and Monte Carlo events for e+jets (left) and μ+jets (right).*

Chapter 5

The ideogram method

This chapter describes how the top quark mass is determined from the sample of selected events. The measurement of the top quark mass is complicated by three causes:

- The momenta of the jets are measured. These, however, are not equal to the momenta of the partons due to QCD radiation and need to be corrected. Because the neutrino escapes detection, its momentum is not known. The $\not\!\!E_T$ can be used for the transverse component of the neutrino momentum, but it has a large uncertainty;

- It is not known which objects should be combined as the decay products of the (anti-)top quarks and the hadronically decaying W boson. This leads to combinatorial problems. The assumption which jets come from which top quark and which come from the hadronically decaying W boson is called a jet-parton assignment;

- As shown in the previous chapter, the event sample contains background events. For the sample used in this analysis the $t\bar{t}$ fraction is measured within uncertainties, but of an individual event it is unknown whether it is a signal or a background event.

Section 5.1 describes several methods used to treat the difficulties of a top quark mass measurement in the semi-leptonic channel. In Sections 5.2 and 5.3 some tools are developed for the analysis. Section 5.4 describes the way a sample likelihood is constructed to fit the top quark mass. Finally, Section 5.5 describes how the top quark mass is extracted from the likelihood.

5.1 Overview of analysis methods

During Run I and Run II both CDF and DØ have used several analysis methods to optimize the top quark mass measurement in the semi-leptonic channel:

Template fitting method: A template fit uses an event variable which is correlated with the top quark mass. The distributions of this event variable in Monte Carlo samples with different top quark input masses are used as templates. These templates and a template for background events are fitted to the distribution observed in data to get a measurement of the top quark mass. The top quark mass and the fitted numbers of signal and background events are combined in a likelihood function. The template fitting method was used by both DØ and CDF during Run I and Run II [70]–[81];

Matrix element method: The matrix element method was first used by DØ on the Run I data [82]. On Run II data it is used by both DØ and CDF [83]–[86]. The matrix element method computes the full Bayesian likelihood for the top quark mass, given the observed data set. It computes an event likelihood and takes into account the probability that a background event leads to the observed kinematics and the probability that a $t\bar{t}$ event leads to these kinematics, given a certain top quark mass. The probability for an event to have the observed kinematics, is given by the differential cross section, which depends on the matrix element. The leading order matrix element is computed for every event. Transfer functions giving the probability that a parton or lepton energy or angle is observed as a certain jet or parton energy or angle, are used. In the end, all event likelihoods are combined to obtain a sample likelihood and the top quark mass for which the sample likelihood is maximal, is the most probable top quark mass;

Ideogram method: The ideogram method, which is the method used in this analysis, was first used for a top quark mass measurement by DØ in the semi-leptonic channel [87]. CDF has published a result with the ideogram method in the fully-hadronic channel [88]. The method was developed at the LEP experiment Delphi for the measurement of the W boson mass [89]–[91]. It computes, like the matrix element method, event likelihoods, which are multiplied to form a likelihood for the sample. In contrast to the matrix element method, the ideogram method does not get the probability for a signal or background event to produce the observed kinematics, by computing the full matrix element, but it uses a more heuristic approach. The idea of the ideogram technique is that the distribution of the reconstructed top quark masses, which will be described in Section 5.3, for the correct jet-parton assignments in signal events peaks at the true top quark mass, whereas the wrong jet-parton assignments and background events have a different fitted top quark mass distribution. To enhance the signal peak each jet-parton assignment is weighted depending on its goodness-of-fit.

The ideogram method explicitly takes signal and background events into account and also accounts for the wrong jet-parton assignments in signal events.

A technical description of the ideogram method, which is used for the measurement presented here, is given in Section 5.4. To tackle the difficulties explained before, several pieces of information and tools are needed:

- Correction functions that correct reconstructed jet energies to parton energies and the resolutions on the reconstructed objects;
- a tool which quantifies how well a certain jet-parton assignment is described by a $t\bar{t}$ hypothesis. For this a kinematic fit is used.

These tools are explained first.

5.2 Energy of the partons

The jet energy scale corrects the jet energy observed in the detector to the energy of a jet of particles, as described in Section 3.2. To reconstruct the top quark mass from the top decay products, the parton energies are needed. The energy of a parton differs from the energy of a particle jet due to particles coming from the parton that do not end up in a 0.5 cone. Therefore, a set of corrections, that corrects the reconstructed particle jet energy to the parton energy, is derived. These are called parton level corrections and the procedure of their derivation is described in Ref. [92]. They are derived from Monte Carlo $t\bar{t}$ events with top quark input masses ranging from 155 GeV/c^2 to 195 GeV/c^2 in steps of 5 GeV/c^2.

A jet-parton matching algorithm is applied to the jets in the Monte Carlo events. A jet is called matched if it has exactly one of the four original quarks from the (anti-)top quark or W boson decay within a cone of 0.5 in ΔR. An event is called matched, if its four leading jets are all matched to different partons. Of the events in the Monte Carlo sample with an input top quark mass of 170 GeV/c^2 51% is matched. Of the events with exactly four jets with $p_T > 20$ GeV/c this is 61%. For the derivation of the parton level corrections only matched events are used.

The parton level corrections are derived separately for b jets and light jets, depending on the true Monte Carlo flavour of the jets. A jet is a b jet, if it contains a B hadron within a cone of $\Delta R < 0.5$. Light jets are all jets not containing a B hadron. The parton level corrections are derived for four different regions in $|\eta_{\text{det}}|$.

In bins of parton energy (E^{parton}) a Gaussian shape is fitted to the distribution of the jet energy (E^{jet}). The mean of the fitted Gaussians is plotted versus E^{parton} and a second order polynomial is fitted to it, as shown in Fig. 5.1. Below E^{parton}= 100 GeV, the fitted curves have an uncertainty of approximately 1 GeV. For higher E^{parton}, statistics are decreasing, leading to an increase of the fit uncertainty. The second

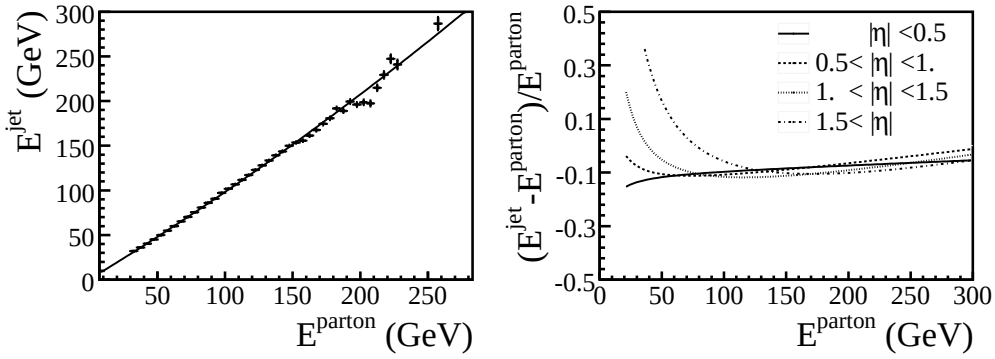

Figure 5.1: E^{jet} *versus* E^{parton} *with a second order polynomial fit for light jets with* $|\eta_{\text{det}}| \leq 0.5$*(left) and the fits to* E^{jet}*-*E^{parton} *divided by* E^{parton} *for b jets (right).*

order polynomial is rewritten as

$$E^{\text{parton}} = \frac{-p_1 + \sqrt{p_1^2 - 4p_2(p_0 - E^{\text{jet}})}}{2p_2}, \tag{5.1}$$

to parametrize E^{parton} as a function of E^{jet}. The fit parameters p_0, p_1, and p_2 are listed in Table 5.1.

	light jets			*b* jets		
η region	p_0(GeV)	p_1	$p_2(\text{GeV}^{-1})$	p_0(GeV)	p_1	$p_2(\text{GeV}^{-1})$
$\lvert\eta_{\text{det}}\rvert \leq 0.5$	0.75	0.92	0.00059	-1.13	0.90	0.00018
$0.5 < \lvert\eta_{\text{det}}\rvert \leq 1.0$	2.01	0.90	0.00055	3.13	0.80	0.00058
$1.0 < \lvert\eta_{\text{det}}\rvert \leq 1.5$	9.65	0.79	0.00083	10.22	0.71	0.00076
$\lvert\eta_{\text{det}}\rvert > 1.5$	21.30	0.72	0.00063	27.27	0.58	0.00093

Table 5.1: *Parameters for the parton level corrections.*

5.2.1 Resolutions

Resolutions of transverse energies and angles of jets

The resolutions of the parton energies are a convolution of the resolution of the parton level corrections and the detector resolution. For previous analyses, the resolutions on the jet momenta were derived on dijet and trijet events in data. However, using those resolutions is incorrect for two reasons:

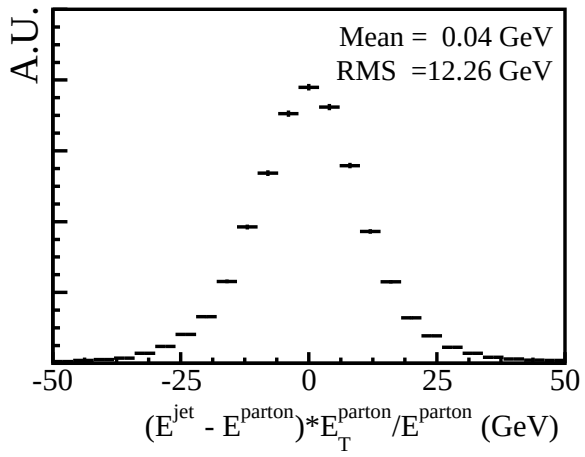

Figure 5.2: *The distribution of* $(E^{\text{parton}}_{\text{comp}} - E^{\text{parton}}_{\text{true}}) \frac{E^{\text{parton}}_{T\ \text{true}}}{E^{\text{parton}}_{\text{true}}}$ *for light jets with* $|\eta_{\text{det}}| < 0.4$.

- the resolutions of jet energies in dijet events are different from the resolutions in semi-leptonic $t\bar{t}$ events. For example dijet events contain more gluon jets which on average are wider than quark jets and have a worse resolution;

- jet energy resolutions derived on data only take into account the detector resolution, but not the resolution on the parton level corrections.

Both objections are avoided by deriving the resolutions on Monte Carlo events, which is legitimate if instrumental resolutions in Monte Carlo events are taken from data. An additional advantage of resolutions derived on Monte Carlo events is that separate resolution functions can be derived for true light jets and b jets, independent of whether or not the jet has a b tag.

For the parametrization of the transverse jet energy resolutions, matched Monte Carlo events, as described in Section 5.2, with an input top quark mass of 165, 170, 175 or 180 GeV/c^2 are used.

The resolutions are parametrized in five $|\eta_{\text{det}}|$ bins. A histogram is filled with $(E^{\text{parton}}_{\text{comp}} - E^{\text{parton}}_{\text{true}}) \frac{E^{\text{parton}}_{T\ \text{true}}}{E^{\text{parton}}_{\text{true}}}$, where $E^{\text{parton}}_{\text{comp}}$ is the parton energy computed by applying the parton level corrections to the observed jet energy and $E^{\text{parton}}_{\text{true}}$ is the true parton energy. This distribution for light jets with $|\eta_{\text{det}}| < 0.4$ is shown in Fig. 5.2 as an illustration. The width of this distribution is used as the resolution on the transverse energy of the partons. This distribution is used instead of the distribution of $E^{\text{parton}}_{T\ \text{comp}} - E^{\text{parton}}_{T\ \text{true}}$ to be independent on a mismeasurement of the jet angles as appropriate.

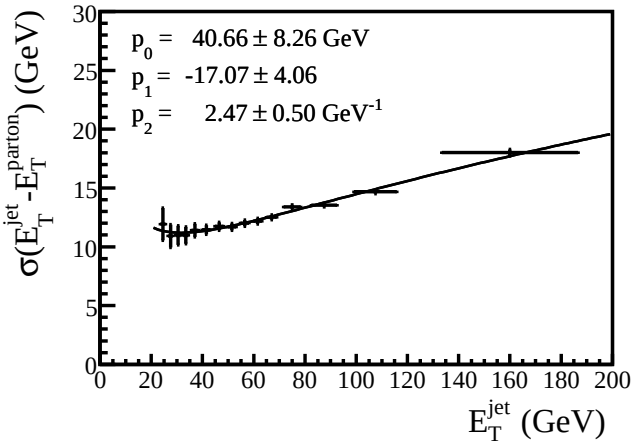

Figure 5.3: *The width of the distribution of* $(E_{\rm comp}^{\rm parton} - E_{\rm true}^{\rm parton})\frac{E_{T\ \rm true}^{\rm parton}}{E_{\rm true}^{\rm parton}}$ *versus* $E_{T\ \rm comp}^{\rm parton}$ *for b jets with* $|\eta_{\rm det}| < 0.4$*. A second order polynomial in* $\ln(E_{T\ \rm comp}^{\rm parton})$ *is fitted.*

The width of this distribution is calculated after removing the highest and lowest percent of events in the distribution to decrease the influence of 'outliers'. This procedure is performed in bins of $E_{T\ \rm comp}^{\rm parton}$. The width is plotted versus $E_{T\ \rm comp}^{\rm parton}$. A second order polynomial in $\ln(E_{T\ \rm comp}^{\rm parton})$ is fitted to this distribution as shown in Fig. 5.3 for light jets with $|\eta_{\rm det}| < 0.4$. The fit is used as the parametrization of the resolution on E_T of the jets. The fit parameters are listed in Table 5.2. The parameters for light jets are highly correlated and give approximately the same curves for $|\eta_{\rm det}| < 1.6$. The fit with $|\eta_{\rm det}| > 1.6$ differs from the others. The same holds for b jets.

In this analysis the resolutions are assumed to be Gaussian. The distribution of the reconstructed minus the true jet η and jet ϕ is not Gaussian, though. To parametrize the uncertainty on jet η, the distribution of the reconstructed jet $\eta_{\rm det}$ minus the true jet $\eta_{\rm det}$ is plotted. Half the interval in which 68% of the jets are, is used as the uncertainty on the jet η. This is done in bins of $\eta_{\rm det}$ on a sample of both light and b jets in matched $t\bar{t}$ events. The uncertainties on ϕ are derived the same way. The uncertainties on jet η and jet ϕ are listed in Table 5.3.

Resolutions of transverse momenta and angles of electrons

The resolutions of the transverse energies of the electrons are parametrized as [93]:

$$\sigma(E_T) = \sqrt{C^2 E_T^2 + S^2 E_T + N^2}\,, \tag{5.2}$$

	light jets			b jets		
η region	p_0 (GeV)	p_1	p_2 (GeV^{-1})	p_0 (GeV)	p_1	p_2 (GeV^{-1})
$\|\eta\| < 0.4$	40.01	-19.61	3.047	40.66	-17.07	2.473
$0.4 \leq \|\eta\| < 0.8$	31.94	-15.31	2.472	26.66	-10.24	1.640
$0.8 \leq \|\eta\| < 1.2$	25.58	-11.79	2.004	18.92	-6.67	1.234
$1.2 \leq \|\eta\| < 1.6$	23.63	-10.94	1.912	15.95	-5.51	1.083
$\|\eta\| \geq 1.6$	26.43	-11.73	1.853	23.04	-9.05	1.433

Table 5.2: *Parameters of the fit to the E_T resolution after the parton level corrections have been applied.*

η region	$\sigma(\eta)$	$\sigma(\phi)$ (radians)
$\|\eta\| < 0.4$	0.039	0.0405
$0.4 \leq \|\eta\| < 0.8$	0.0395	0.04
$0.8 \leq \|\eta\| < 1.2$	0.046	0.047
$1.2 \leq \|\eta\| < 1.6$	0.0605	0.0545
$\|\eta\| \geq 1.6$	0.0525	0.0475

Table 5.3: *The resolutions of the jet angles.*

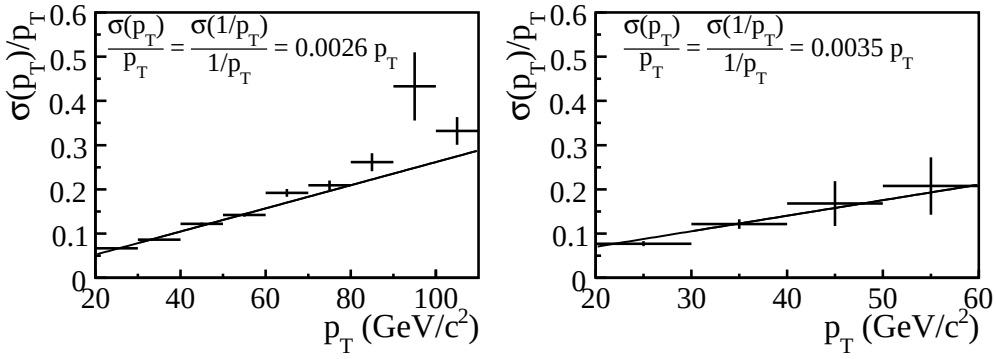

Figure 5.4: *The width of the distribution of* $\frac{p_T^{\text{reco}}-p_T^{\text{true}}}{p_T^{\text{true}}}$ *versus* p_T^{true} *for muons with* $|\eta_{\text{det}}| < 1.6$ *(left) and* $|\eta_{\text{det}}| > 1.6$ *(right plot). The function in Eq. 5.3 is fitted not taking into account the muons with* $p_T < 30$ *GeV/c to avoid a selection bias.*

with $C = 0.44$, $S = 0.23\ \sqrt{\text{GeV}}$ and $N = 0.21$ GeV for electrons with $|\eta_{\text{det}}| < 1.1$ and $C = 0.32$, $S = 0.26\ \sqrt{\text{GeV}}$ and $N = 0.20$ GeV for electrons with $|\eta_{\text{det}}| > 1.1$. For the resolutions of η and ϕ of the electrons 0.0071 and 0.006 radians are used, respectively.

Resolutions of transverse momenta and angles of muons

The transverse momentum of muons is measured with the inner tracker. The relative resolution of $1/p_T$ of the muon is given by:

$$\frac{\sigma(1/p_T)}{1/p_T} = \frac{\sigma(p_T)}{p_T} = \sqrt{C^2 + N^2 p_T^2}\,. \tag{5.3}$$

The resolution of $1/p$ comes from the resolution of $1/p_T$ via:

$$\sigma(1/p) = \sin(\theta)\ \sigma(1/p_T)\,. \tag{5.4}$$

The parameters C and N are determined on $t\bar{t}$ Monte Carlo events with an input top quark mass of 170 GeV/c^2. The distribution of $\frac{p_T^{\text{reco}}-p_T^{\text{true}}}{p_T^{\text{true}}}$, in which p_T^{reco} is the reconstructed and p_T^{true} is the true muon transverse momentum, is plotted in bins of p_T^{true}. Gaussians are fitted to these distributions and the widths of these Gaussians are used as $\frac{\sigma(p_T)}{p_T}$, which is plotted versus p_T^{true}, as shown in Fig. 5.4. The function from Eq. 5.3 is fitted. In the fit the lowest bin in p_T is not used to avoid a selection bias due to the cut $p_T^{\text{reco}} > 20$ GeV/c. The constant parameter C is found to be 0. The noise parameter N is 0.0026 (GeV/c)$^{-1}$ for $|\eta_{\text{det}}| < 1.6$ and 0.0035 (GeV/c)$^{-1}$ for $|\eta_{\text{det}}| > 1.6$.

Because the muon angles are measured with the inner tracker, the angles are known very well and the angular resolutions are set to very small numbers: $1 \cdot 10^{-4}$ radians and 0.003 for the resolution on ϕ and η, respectively.

5.3 Kinematic fit

5.3.1 Jet-parton assignments

It is not known which jet originates from which parton, but a specific jet-parton assignment can be assumed. In an event with four jets, there are twelve jet-parton assignments that lead to different reconstructed invariant top quark and W boson masses. In an event with five or more jets, only the leading four jets are used in this analysis.

Longitudinal momentum of the neutrino

The longitudinal momentum of the neutrino, p_z^ν, is unknown. It can be solved, however, from the constraint that the reconstructed hadronic top quark mass and the reconstructed leptonic top quark mass be equal when taking $\not\!\!E_T$ as the transverse momentum of the neutrino. This leads to a quadratic equation for p_z^ν, which in general has two solutions, which are both used as initial values before the fit. If the solution is complex, only the real part is used. Therefore, there are two solutions per jet-parton assignment.

5.3.2 Kinematic fit

For both solutions of every jet-parton assignment, a kinematic fit is performed of the jet energies, jet angles and the energy and angles of the charged lepton and the direction and size of $\not\!\!E_T$ under the following constraints:

$$m_t^{\text{had}} = m_t^{\text{lep}} \tag{5.5}$$

and:

$$M_W^{\text{had}} = M_W^{\text{lep}} = 80.4 \text{ GeV}/c^2\,, \tag{5.6}$$

in which m_t^{had}, M_W^{had}, m_t^{lep} and M_W^{lep} are the reconstructed masses of the hadronically decaying top quark and W boson and the leptonically decaying top quark and W boson, respectively. The kinematic fit minimizes:

$$\chi^2 = \sum \frac{(x_f - x_m)^2}{\sigma^2(x_m)}\,, \tag{5.7}$$

where the sum runs over the observables x, x_m is the measured value of x, x_f its fitted value, and $\sigma(x_m)$ the uncertainty on x_m. The observables x are:

- energies of the jets;
- azimuthal angles of the jets;
- pseudo-rapidities of the jets;
- energy of the electron or $1/p$ of the muon;
- azimuthal angle of the charged lepton;
- pseudo-rapidity of the charged lepton;
- components of $\vec{k}_T$.

The two components in the last item above are the last two observables and come from $\not\!\!E_T$, which should represent the transverse momentum of the neutrino. Because the missing energy can be caused by a mismeasurement of the energies of the lepton or the jets, in order to decrease the correlation between the used observable and the jet energies and lepton energy, the following quantity is constructed:

$$\vec{k}_T = \vec{E}_T^{\text{lepton}} + \vec{\not\!\!E}_T + \sum \vec{E}_T^{\text{jet}}, \tag{5.8}$$

of which the components are used as observables in the fit with an uncertainty of 8 GeV. This variable is explained in more detail in Ref. [93].

Before the fit, the jet energies are corrected using the parton level correction, depending on the assumed parton flavour in the jet-parton assignment. The jet mass is set to 5 GeV/c^2 for assumed b jets and 0 GeV/c^2 for assumed light jets. The jet momenta are scaled to keep the jet mass constant.

With the fit values x_f for which the χ^2 defined in Eq. 5.7, is minimal, the fitted top quark mass, m_i, and its uncertainty, σ_i, are computed. The fit is described in detail in Ref. [93]. During the fitting procedure, p_z^ν is recalculated to match the constraints.

5.3.3 Performance of the kinematic fit

To study the performance of the fit, the matching algorithm described in Section 5.2 is used. In matched events it is known which jet-parton assignment is the correct one. Figures 5.5–5.9 show the performance of the parton level corrections and the kinematic fit. The plots only show information from the correct jet-parton assignment for Monte Carlo events with an input top quark mass of 170 GeV/c^2.

Figure 5.5 shows the distribution of the reconstructed mass of the hadronically decaying W boson after application of the parton level corrections, but before fitting. There are some bins with large uncertainties. These are due to the large event weights.

Figure 5.6 shows the distribution of the χ^2 probability. For this fit with two degrees of freedom the probability is $e^{-\frac{1}{2}\chi^2}$. In case the resolution parametrizations mimic the true resolutions and these are Gaussian, this distribution is flat between 0 and 1.

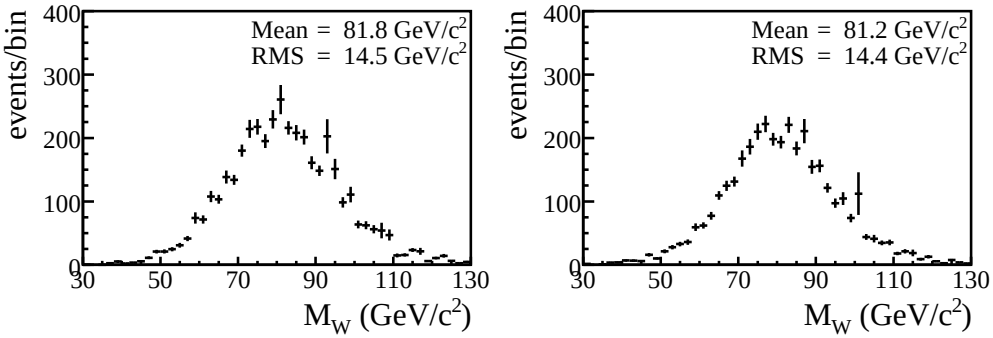

Figure 5.5: *The distribution of the mass of the W boson of the correct jet-parton assignment after application of the parton level corrections in matched Monte Carlo e+jets (left) and μ+jets (right plot) events with an input top quark mass of 170 GeV/c^2.*

As can be seen, it is rather flat, except for the rise at $e^{-\frac{1}{2}\chi^2} \approx 0$, indicating events with large χ^2. It is known that the detector resolutions have large non-Gaussian tails, which probably cause this rise.

Figure 5.7 shows the rank of the correct jet-parton assignment. All jet-parton assignments of an event are sorted according to χ^2. The position in this sorted list is the rank of the jet-parton assignment, with the jet-parton assignment with the lowest χ^2 having rank 0, the one with the second lowest χ^2 having rank 1, etc. Because there are two p_z^ν solutions per correct jet-parton assignment of an event, the distribution of the rank of the correct jet-parton assignment comes in pairs.

Figure 5.8 shows the distribution of the reconstructed mass of the top quark in the correct jet-parton assignment after the fit. The means of the distributions and the means of the fitted Gaussians are higher than the input top quark mass. This is due to imperfect parton level corrections.

Figure 5.9 shows the distribution of the pull of the reconstructed mass of the top quark in the correct jet-parton assignment after the kinematic fit. For a Monte Carlo input top quark mass of 170 GeV/c^2, which is used here, the pull is defined as $\frac{m_i - 170\ \mathrm{GeV}/c^2}{\sigma(m_i)}$, where m_i is the reconstructed mass of the top quark and $\sigma(m_i)$ is the computed uncertainty on the reconstructed mass of the top quark. The width of the pull distribution is larger than unity. Because both the parton level corrections and the jet resolutions were derived from the same sample, the pull width of the jet energies is close to unity. Still the pull width of the top quark mass can differ from unity. This happens if the energies of jets in an event do not shift in an uncorrelated way. If there is a positive correlation between the shifts in jet energies, the pull of the top quark mass tends to be wider than unity. In the rest of this analysis the

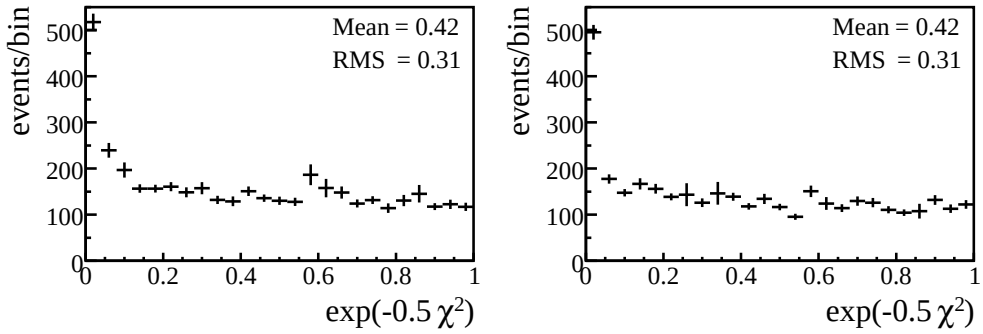

Figure 5.6: *The distribution of the χ^2 probability, $e^{-\frac{1}{2}\chi^2}$, of the correct jet-parton assignments in matched Monte Carlo e+jets (left) and μ+jets (right plot) events with an input top quark mass of 170 GeV/c^2.*

uncertainty on the top quark mass coming from the kinematic fit is increased by the width of the Gaussian fit to the pull distribution, i.e. 1.23 for e+jets events and 1.18 for μ+jets events. The χ^2 coming from the fit is scaled down accordingly by a factor $1/\sqrt{1.23}$ for e+jets events and $1/\sqrt{1.18}$ for μ+jets events. This procedure gives the same result as scaling up all momentum and angle resolutions by the same factors before the fit.

5.3.4 Additional event selection cut

An additional event selection cut is applied at this stage. Events with no jet-parton assignment with $\chi^2 < 10$ are rejected. These are poorly measured events which should not have much influence on the measurement. This cut removes 6 e+jets and 4 μ+jets data events. The percentage of events removed by this cut per sample is shown in Table 5.4.

sample	e+jets	μ+jets
data	1.3%	1.0%
$t\bar{t}$ (170 GeV/c^2)	0.9%	0.8%
W+jets	0.9%	0.5%
QCD	0.7%	0.6%

Table 5.4: *The percentage of events removed by the χ^2 event cut.*

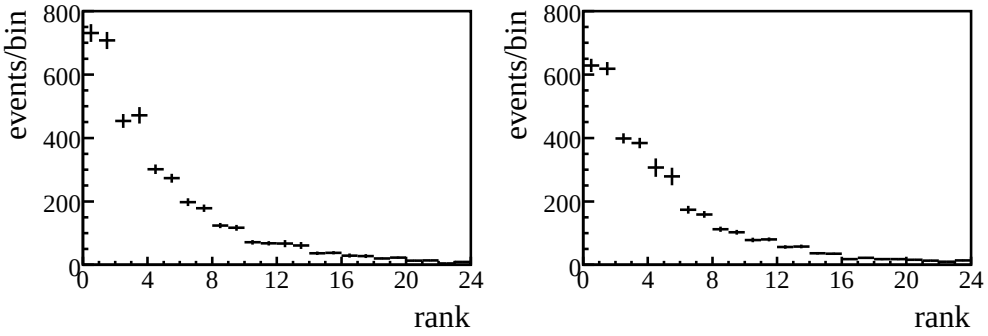

Figure 5.7: *The distribution of the rank of the correct jet-parton assignment in matched Monte Carlo e+jets (left) and μ+jets (right plot) events with an input top quark mass of 170 GeV/c^2. The rank is the place in a list sorted according to χ^2, starting with a rank of 0 for the jet-parton assignment with the lowest χ^2.*

5.4 The ideogram method

The jet energy scale uncertainty leads to a large systematic uncertainty on the measured top quark mass. In semi-leptonic $t\bar{t}$ events the jet energy scale can be calibrated using the hadronically decaying W boson. Several analyses have introduced a parameter, the JES factor, by which all jet energies are scaled. This parameter is extracted simultaneously with the top quark mass. This shifts part of the systematic uncertainty to the statistical uncertainty, but decreases the total uncertainty. An additional advantage of an in situ fit of an overall JES factor is that it is fitted on the same sample that is used for the top quark mass measurement and thus removes the sample dependence of the JES. However, the JES factor and the top quark mass are to a large extent correlated, giving rise to additional systematic uncertainties.

Recently the uncertainty on the JES determination has been decreased considerably to typically 1%. The gain of an in situ JES calibration is no longer expected to be significant and is not used in this analysis. The fraction of $t\bar{t}$ events in the data sample, f_t, is fitted together with the top quark mass, as is done in Ref. [87].

Bayes's theorem claims that the probability $P(m_t, f_t|\text{data})$ for top quark mass, m_t, and signal fraction, f_t, in the theory to be correct, given an observed data set, is given by:

$$P(m_t, f_t|\text{data}) = \frac{P(\text{data}|m_t, f_t)}{P(\text{data})} P(m_t, f_t), \tag{5.9}$$

where $P(\text{data}|m_t, f_t)$ is the probability to observe the data given m_t and f_t, and $P(m_t, f_t)$ and $P(\text{data})$ represent the prior knowledge of the set (m_t, f_t) and the experimental outcome. The most likely values of m_t and f_t, given the data, are those

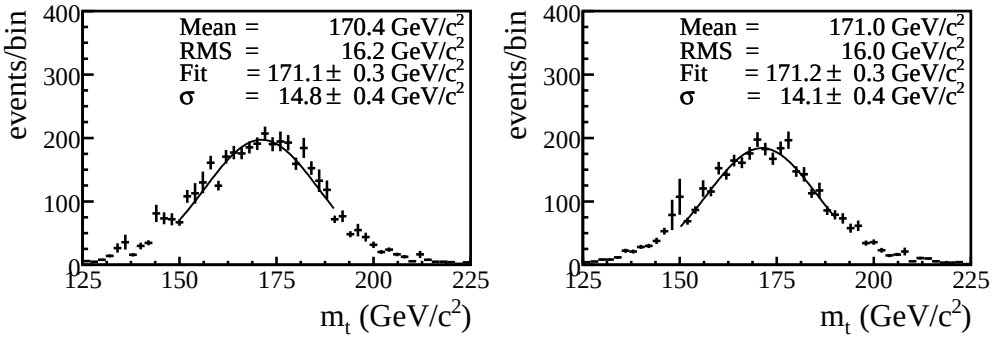

Figure 5.8: *The distribution of the mass of the top quark for the correct jet-parton assignment in matched Monte Carlo e+jets (left) and μ+jets (right plot) events with an input top quark mass of 170 GeV/c^2 after the kinematic fit was applied. A Gaussian fit is performed between 150 GeV/c^2 and 190 GeV/c^2.*

where the probability in Eq. 5.9 is maximal. The goal of the ideogram method is to find these values of m_t and f_t.

If one assumes no prior knowledge about m_t, f_t and the outcome of the experiment, $P(m_t, f_t)$ and $P(\text{data})$ should be taken flat in m_t and f_t and data. $P(\text{data})$ and $P(m_t, f_t)$ then only yield a constant factor in the total probability. Because the value of $P(m_t, f_t|\text{data})$ is not important, but only the position of the maximum is, an overall factor can be dropped. From now on the priors in Eq. 5.9 are left out. Because this destroys the normalization of the right hand side of Eq. 5.9, we no longer calculate a probability, but a likelihood, $\mathcal{L}$. The problem has been reduced to finding the probability $P(\text{data}|m_t, f_t)$.

It is reasonable to assume all events to be independent, so the probability to observe a data set, $P_{\text{sample}}(\text{data}|m_t, f_t)$ is the product of the probabilities to observe the individual events, $P_{\text{event}}(x_{\text{obs}}|m_t, f_t)$:

$$P_{\text{sample}}(\text{data}|m_t, f_t) = \prod_{\text{events}} P_{\text{event}}(x_{\text{obs}}|m_t, f_t)\,. \tag{5.10}$$

x_{obs} denotes all the observations in an event. The probability for an event in a sample with signal fraction f_t to have the observed state x_{obs} is:

$$P_{\text{event}}(x_{\text{obs}}|m_t, f_t) = f_t P_{\text{sgn}}(x_{\text{obs}}|m_t) + (1 - f_t) P_{\text{bg}}(x_{\text{obs}})\,, \tag{5.11}$$

in which $P_{\text{sgn}}(x_{\text{obs}}|m_t)$ is the probability that a signal event gives the observation x_{obs} and $P_{\text{bg}}(x_{\text{obs}})$ is the probability that a background event gives x_{obs}. $P_{\text{bg}}(x_{\text{obs}})$ is independent of m_t.

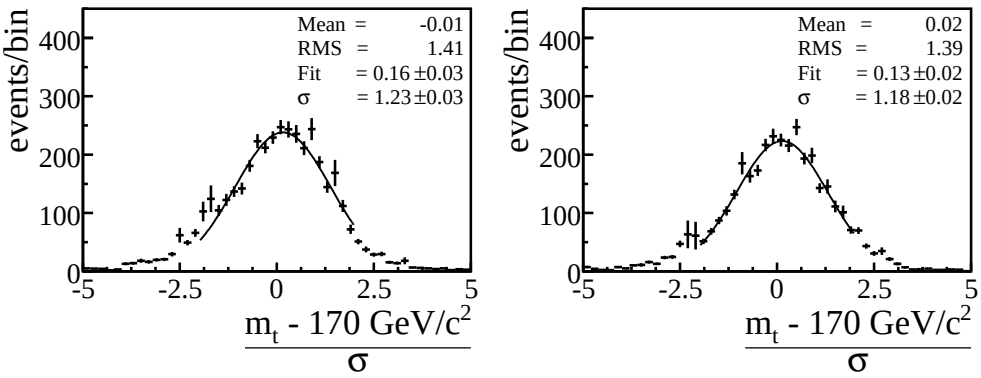

Figure 5.9: *The distribution of the pull of the top quark mass for the correct jet-parton assignment in matched Monte Carlo e+jets (left) and μ+jets (right plot) events with an input top quark mass of 170 GeV/c^2 after the kinematic fit was applied. A Gaussian is fitted between −2 and +2.*

In the analysis described in this thesis, $x_{\rm obs}$ is approximated by the observed discriminant, D, which was introduced in Section 4.2.1, and $x_{\rm fit}$, which is the information coming from applying the kinematic fit, described in Section 5.3, to every jet-parton assignment, together with the b tag information.

The discriminant and $x_{\rm fit}$ are assumed uncorrelated. In Monte Carlo events with an input top quark mass of 170 GeV/c^2 the correlation between the fitted top quark mass of the jet-parton assignment with the lowest χ^2 and the discriminant is -1.3% for e+jets events and -2.0% for μ+jets events, which justifies the approximation of taking them as uncorrelated. The probabilities in Eq. 5.11 then factorize:

$$P_{\rm sgn}(x_{\rm obs}|m_t) = P_{\rm sgn}(D, x_{\rm fit}|m_t) = P_{\rm sgn}(D)P_{\rm sgn}(x_{\rm fit}|m_t) \tag{5.12}$$

and

$$P_{\rm bg}(x_{\rm obs}) = P_{\rm bg}(D, x_{\rm fit}) = P_{\rm bg}(D)P_{\rm bg}(x_{\rm fit})\,, \tag{5.13}$$

with $P_{\rm sgn}(D)$ and $P_{\rm bg}(D)$ the probabilities that, respectively, a signal or a background event has discriminant D, and $P_{\rm sgn}(x_{\rm fit}|m_t)$ and $P_{\rm bg}(x_{\rm fit})$ the probability that, respectively, a signal or a background event has $x_{\rm fit}$.

The discriminant is designed to be uncorrelated with the top quark mass. The correlation between the discriminant and the top quark mass for a Monte Carlo sample with various input top quark masses is 0.7% for e+jets events and 1.9% for μ+jets events. Because of the independence of m_t and D, $P_{\rm sgn}(D)$ does not depend on m_t.

The probability $P_{\rm sgn}(D)$ for a signal event to have a value D for the discriminant is $s(D)$, where $s(D)$ is the normalized distribution of D in signal events, as introduced in Section 4.2.1. Likewise, the probability $P_{\rm bg}(D)$ is $b(D)$. As stated before, multiplying

the likelihood by a constant scale factor has no effect on the top quark mass fit. Multiplying the event probability of a specific event does not have an effect either. If $s(D)$ and $b(D)$ are divided by $s(D) + b(D)$, which per event is just a constant, the likelihoods $\mathcal{L}_{\mathrm{sgn}}(D) = \frac{s(D)}{s(D)+b(D)}$ and $\mathcal{L}_{\mathrm{bg}}(D) = \frac{b(D)}{s(D)+b(D)}$ are the discriminant probabilities introduced in Section 4.2.1. The parametrization derived in Section 4.2.1 is used for them.

The terms $P_{\mathrm{sgn}}(x_{\mathrm{fit}}|m_t)$ and $P_{\mathrm{bg}}(x_{\mathrm{fit}})$ are described hereafter.

5.4.1 Jet-parton assignment weight

The signal and background probabilities are calculated as a sum over both p_z^ν solutions of all jet-parton assignments. Every jet-parton assignment is weighted by the probability that it is correct. Without b tagging, the probability for a jet-parton assignment in a $t\bar{t}$ event to be the correct one, is $e^{-\frac{1}{2}\chi^2}$. With b tagging information, this probability has to be multiplied by the probability, p_{tags}, that this jet-parton assignment gives the observed b tags, if it is the correct jet-parton assignment:

$$p_{\mathrm{tags}} = \prod_{k=1}^{4} p_k^j \,, \tag{5.14}$$

with p_k^j the probability that jet k is b tagged or not, depending on whether it has a b tag, and on the assumed jet flavour j. E.g. for an assumed b jet, which is b tagged, p_k^j is the tag rate function, which is described in Section 3.2.4.

The total jet-parton assignment weight, w_i, for jet-parton assignment i is thus:

$$w_i = e^{-\frac{1}{2}\chi_i^2} \prod_{k=1}^{4} p_k^j \,. \tag{5.15}$$

Formally, this weight is not a probability, because it is not normalized. From here on the requirement that w_i be a probability is dropped.

5.4.2 Signal probability

The rightmost term in Eq. 5.12, $P_{\mathrm{sgn}}(x_{\mathrm{fit}}|m_t)$, is written as the sum over both solutions of all 12 jet-parton assignments, with each jet-parton assignment weighted by w_i as given by Eq. 5.15.

For the probability of jet-parton assignment i, the assumption is made that x_{fit} is represented by the fitted top quark mass (m_i), its uncertainty (σ_i), the χ_i^2 and the number of b tags. The probability is split into two terms. One term, containing $\mathbf{S}(x_i|m_t)$, represents the probability that the information of this jet-parton assignment is compatible with top quark mass m_t, assuming the jet-parton assignment is correct. The other term, containing $\mathbf{BG}_{\mathrm{comb}}(x_i|m_t)$, represents the probability that

the information is compatible with m_t, assuming that this is the wrong jet-parton assignment:

$$P_{\rm sgn}(x_{\rm fit}|m_t) = \sum_{i=1}^{24} w_i \left\{ f_{\rm correct}^{N_{\rm tags}}\ \mathbf{S}(x_i|m_t) + (1 - f_{\rm correct}^{N_{\rm tags}})\ \mathbf{BG}_{\rm comb}^{N_{\rm tags}}(x_i|m_t) \right\}. \quad (5.16)$$

Both terms are weighted by the factors $f_{\rm correct}^{N_{\rm tags}}$. $\mathbf{S}(x_i|m_t)$, $\mathbf{BG}_{\rm comb}(x_i|m_t)$ and $f_{\rm correct}^{N_{\rm tags}}$ are described hereafter.

Correct jet-parton assignments

The probability for a $t\bar{t}$ event to have a certain invariant top quark mass is given by a Breit-Wigner shape with its peak at the top quark mass, m_t, and a width equal to the top quark width. The probability that, if one deals with the correct jet-parton assignment, the top quark mass is reconstructed as m_i, when the true invariant top quark mass is m', is approximated by a Gaussian with its mean at m' and a width of σ_i. The probability that a $t\bar{t}$ event has a reconstructed top quark mass m_i in the correct jet-parton assignment is the convolution of the Breit-Wigner and the Gaussian:

$$\mathbf{S}(x_i|m_t) = \int \mathbf{BW}(m', m_t)\mathbf{G}(m_i, \sigma_i, m')dm' \,. \quad (5.17)$$

In this analysis the width of the Breit-Wigner is set to 2 GeV/c^2. The integration is performed from 100 GeV/c^2 to 300 GeV/c^2, which is large enough not to bias the final result.

Wrong jet-parton assignments

The combinatorial background term $\mathbf{BG}_{\rm comb}(x_i|m_t)$ in Eq. 5.16, which represents the probability that a wrong jet-parton assignment in a $t\bar{t}$ event leads to the observed experimental signature, depends on both the true top quark mass (m_t), the fitted top quark mass (m_i) and the number of b tags in the event.

This dependence is modelled using the wrong jet-parton assignments in parton matched $t\bar{t}$ events with various input top quark masses. It is done separately for events with 0, 1 and 2 or more b tags. Per top quark input mass, a histogram of the fitted top quark masses is created, in which every entry has been weighted with w_i. Double Gaussians are fitted to these histograms. The result for events with 0 b tags is shown in Fig. 5.10.

The widths, means and the ratio of the heights of the fitted Gaussians are plotted versus the input top quark mass and a linear fit is performed, as shown in Fig. 5.11 for events with 0 b tags. The parameters of the linear fits are shown in Table 5.5.

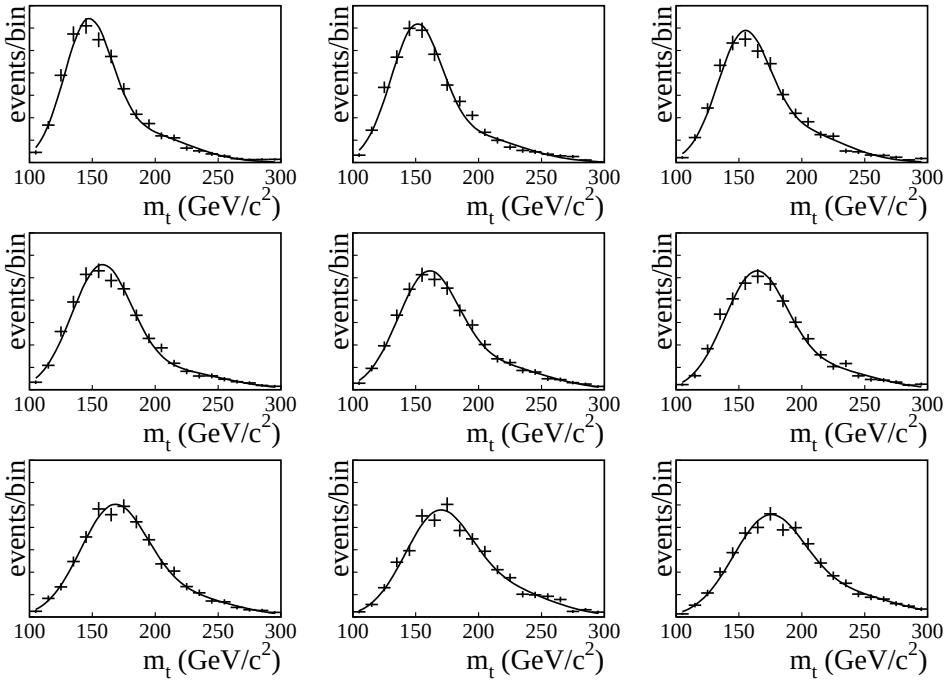

Figure 5.10: *Double Gaussians fitted to the distribution of the fitted top quark masses weighted by w_i for the wrong jet-parton assignments in matched Monte Carlo events with 0 b tags in a $t\bar{t}$ sample with an input top quark mass going in steps of 5 GeV/c^2 from 155 GeV/c^2 (left upper plot) to 195 GeV/c^2 (right lower plot).*

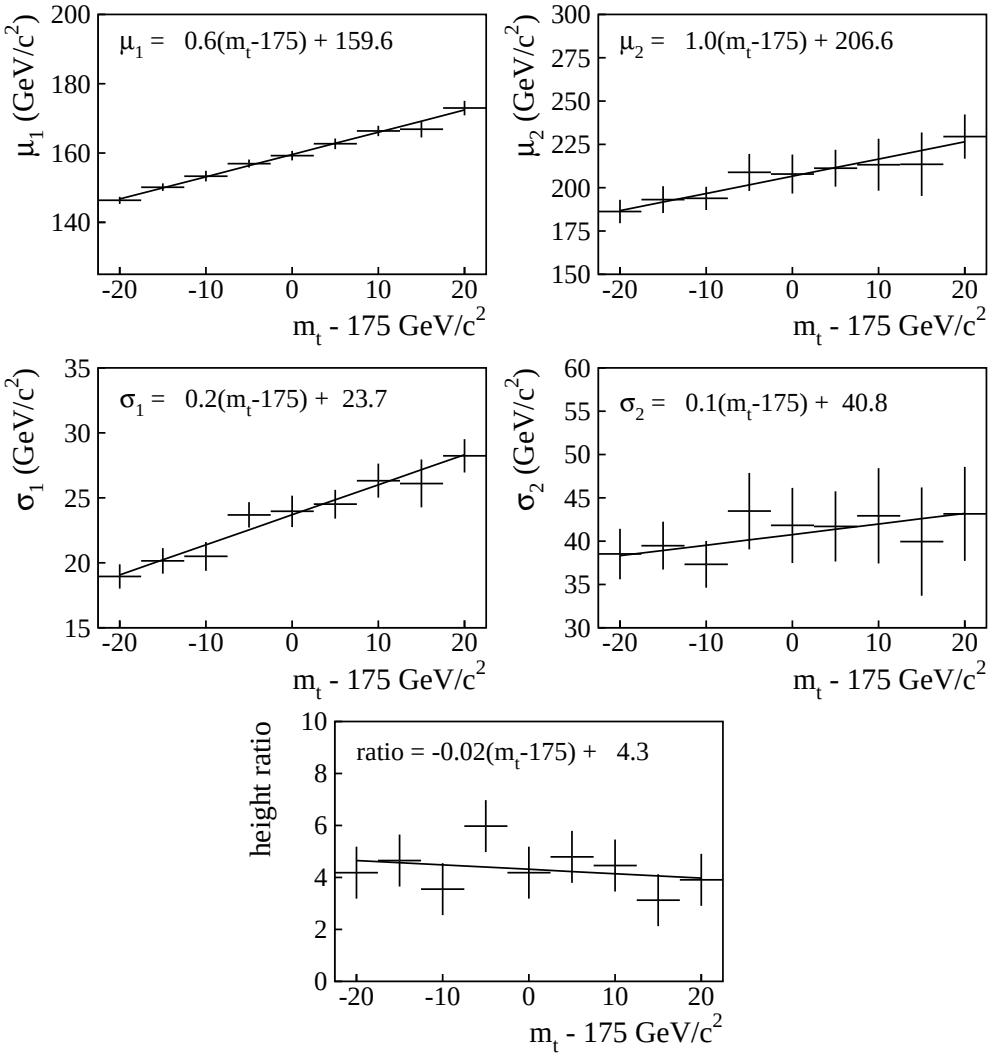

Figure 5.11: *Linear fits to the parameters of the double Gaussians shown in Fig. 5.10. The upper plots show the means of the two Gaussians. The middle plots show the widths of the two Gaussians and the bottom plot shows the ratio of the heights of the two Gaussians.*

		Gaussian 1		Gaussian 2	
	Parameter	p_0	$p1$	p_0	$p1$
0 b tags	a	4.3	-0.017	1	0
	μ	159.6	0.642	206.6	0.995
	σ	23.7	0.231	40.8	0.122
1 b tag	a	3.8	0.007	1	0
	μ	159.8	0.589	207.8	0.862
	σ	22.8	0.210	41.1	0.090
2 b tags	a	2.7	0.034	1	0
	μ	159.6	0.576	208.4	0.843
	σ	22.6	0.133	40.3	0.004

Table 5.5: *Parameters describing the wrong jet-parton assignment shape by the sum of two Gaussians* $G(m_{\text{fit}}) = a \cdot \exp\left[-(\mu - m_{\text{fit}})^2/2\sigma^2\right]$. *The three parameters* a, μ, *and* σ *evolve linearly as a function of the generated top quark mass* m_t *as* $p_0 + p_1 \cdot (m_t - 175\ GeV/c^2)$.

The factors $f_{\text{correct}}^{N_{\text{tags}}}$

Because there is no a priori procedure to compute the factors $f_{\text{correct}}^{N_{\text{tags}}}$, they are tuned so that both terms in Eq. 5.16 are weighted correctly. This is done by performing ensemble tests, as described in Chapter 6, on $t\bar{t}$ Monte Carlo events with various top quark input masses. The event likelihood, as given by Eq. 5.11, is computed for every event with f_t fixed at 1. Ensembles are created using only matched $t\bar{t}$ events. This is done for events with 0, 1 and 2 or more b tags separately. The factors $f_{\text{correct}}^{N_{\text{tags}}}$ are tuned such that the mean fitted top quark mass comes out as closely as possible to the input top quark mass. The result of this tuning is visible in Fig. 6.3. Factors of 0.35 (0 b tags), 0.7 (1 b tag) and 0.8 (≥ 2 b tags) are found.

5.4.3 Background shape

The background term in Eq. 5.13 is calculated as:

$$P_{\text{bg}}(x_{\text{fit}}) = \sum_{i=1}^{24} w_i \cdot \mathbf{BG}(m_i)\,, \tag{5.18}$$

where the background shape $\mathbf{BG}(m)$ is the shape of the fitted mass spectrum for background events. To obtain $\mathbf{BG}(m)$, the distribution of the fitted masses m_i for all possible jet-parton assignments i for the W+jets Monte Carlo sample is plotted.

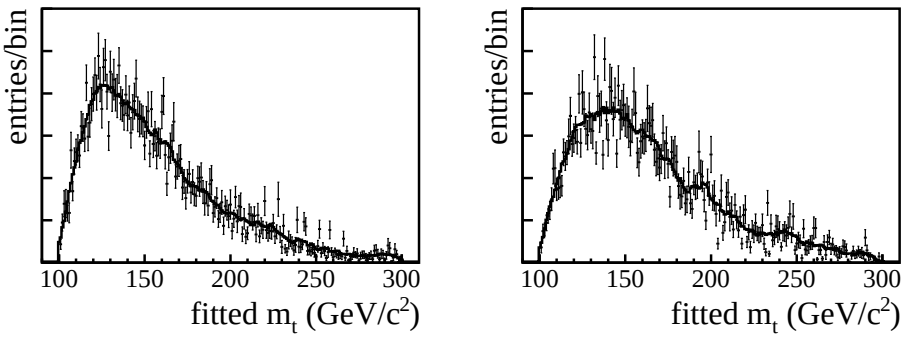

Figure 5.12: *Histograms of the fitted masses from the (W+jets) background sample (points with error bars), for the e+jets channel (left) and μ+jets channel (right). Every entry has been weighted by w_i. To reduce statistical fluctuations, the shapes are smoothened by averaging over a sliding window of ±5 GeV/c^2 around each fitted mass. The smoothened histogram is shown as a solid line, which denotes the* $\mathbf{BG}(m_i)$ *shape that is used in the ideogram likelihood.*

All entries are weighted by their weight w_i, defined in Eq. 5.15. Separate $\mathbf{BG}(m)$ for the e+jets and μ+jets channels are used. The distributions are shown in Fig. 5.12. Due to the fine 1 GeV/c^2 binning and the large fluctuations in the Monte Carlo event weights for events generated by Alpgen, there are large statistical fluctuations. To reduce the statistical fluctuations, the shapes are smoothened by averaging over a sliding window of ±5 GeV/c^2 around each fitted mass. This shape is normalized to unit area to form $\mathbf{BG}(m)$.

5.5 Maximization of the likelihood

The sample likelihood given by Eq. 5.10, is computed for the observed data sample for a set of hypothetical top quark masses, m_t, between 125 GeV/c^2 and 225 GeV/c^2 in steps of 1 GeV/c^2 and hypothetical purities, f_t, between 0 and 1 in steps of 0.05. This likelihood is normalized so that in the bin in m_t and f_t where it is maximal, it is 1. The values of m_t and f_t for which $-2\ln(\mathcal{L})$ is minimal, are searched. This is done as follows. First, for each fixed m_t, the value of f_t at which $-2\ln(\mathcal{L})$ is minimal, is searched. These values of f_t define a line in the f_t, m_t-plane. $-2\ln(\mathcal{L})$ along this line is projected onto the m_t axis. Then, the value of m_t for which the projected $-2\ln(\mathcal{L})$ is minimal, is searched. For this m_t and $m_t - 1$ GeV/c^2 and $m_t + 1$ GeV/c^2 a parabola is used to describe the projected $-2\ln(\mathcal{L})$. The position, m_t^{fit} of the minimum of the parabola is the fitted top quark mass in the sample.

The uncertainty on the fitted top quark mass is given by the standard deviation of

the distribution of the likelihood $\mathcal{L}$. If $\mathcal{L}$ is Gaussian, which it is to good approximation, the standard deviation is the width of the Gaussian, which is equal to the σ for which $-2\ln(\mathcal{L}(m_t^{\text{fit}}+\sigma)) + 2\ln(\mathcal{L}(m_t^{\text{fit}})) = 1$. This σ is computed from the parabola fit to the projected $-2\ln(\mathcal{L})$ and is the statistical uncertainty on the fitted top quark mass.

A method to extract the top quark mass from a data set has been presented in this chapter. Due to several approximations, the fitted top quark mass is not equal to the true top quark mass. It is only an estimator of the top quark mass. The relation between the fitted and the true top quark mass, which is the calibration of the method, is obtained in the next chapter. With the method and its calibration the top quark mass can be measured on data.

Chapter 6

Calibration of the method

The previous chapter describes the ideogram method, which determines the top quark mass with a likelihood function. Due to several approximations made in the construction of the likelihood, the fitted top quark mass may differ from the true top quark mass. By performing the analysis on Monte Carlo events, for which the true top quark mass is known, one can determine the bias, that is the fitted minus the true top quark mass, of the method. The bias is parametrized as a function of the top quark mass and used to calibrate the result obtained from data events. The calibration is obtained using several ensembles of event collections with an equal number of events as observed in data. From these ensemble tests also the uncertainty on the top quark mass is calibrated. The first section of this chapter introduces the adopted procedure. For illustration purposes Section 6.2 describes the results of ensemble tests in which only signal events are used. Section 6.3 describes ensemble tests that should mimic the data. These are used for the calibration of the measurement on data.

6.1 Ensemble tests

Pseudo-experiments are performed on Monte Carlo events with known top quark mass and each pseudo-experiment is treated as an independent experiment. This way it is known what would happen if the experiment were repeated many times. The average fitted mass in an ensemble of pseudo-experiments provides the calibration. The standard deviation of the calibrated fitted top quark masses of the pseudo-experiments gives the expected statistical uncertainty.

Per pseudo-experiment, an event collection containing $t\bar{t}$, W+jets and QCD events is created. The total collection size is fixed to 845 and the fractions of $t\bar{t}$, W+jets and QCD events are randomly taken from a Poisson distribution around the observed fractions in data, as listed in Table 4.4. To make optimal use of the available Monte Carlo statistics, standard resampling techniques are used, allowing Monte Carlo events

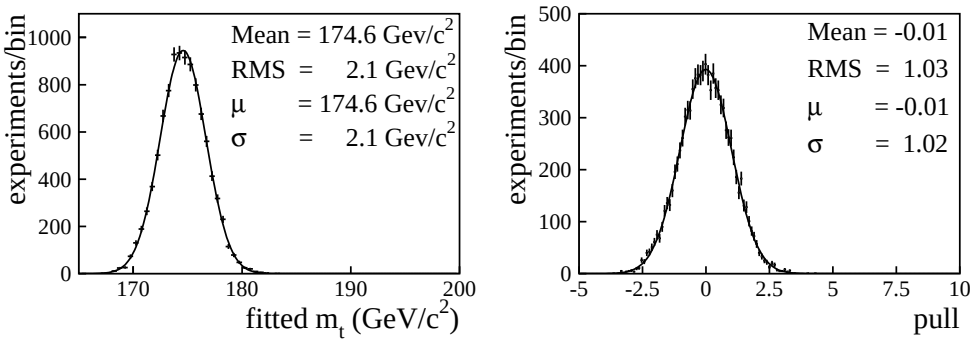

Figure 6.1: *An example of the Gaussian distribution of the fitted top quark masses (left plot) and the pull of the fitted top quark masses (right plot) of an ensemble of 10000 pseudo-experiments, fitted using a Gaussian shape. Each pseudo-experiment in this ensemble has signal and background events. The signal events have a true top quark mass of 175 GeV/c^2.*

to be selected multiple times when constructing the pseudo-experiments. Hence, the pseudo-experiments are correlated, but the correlation between the events in an individual pseudo-experiment is negligible.

Ensemble tests are performed for the e+jets, the μ+jets and the lepton+jets channel separately, on $t\bar{t}$ samples with input top quark masses of 155, 160, 165, 170, 175, 180, and 185 GeV/c^2. For each ensemble test with a certain input top quark mass, 10,000 pseudo-experiments are performed. As an illustration, the resulting fitted top quark mass and pull distributions for the test with an input top quark mass of 175 GeV/c^2 are shown in Fig. 6.1. Gaussian shapes are fitted to the distributions. The mean of the shape in the left plot is used as the average fitted top quark mass of the ensemble, which comes out just below the input top quark mass. The width of this distribution represents the expected statistical uncertainty. Note that this width is unbiased, because the correlation between events in one pseudo-experiment due to the resampling, is negligible. The width of the pull distribution is close to unity, which implies that the ideogram method correctly represents the statistical uncertainty.

6.1.1 Combining e+jets and μ+jets samples

The events used for the pseudo-experiments are picked from the Monte Carlo samples described in Section 3.1 and from the dedicated QCD sample. The ratio of e+jets and μ+jets events in these samples is not the same as in Table 4.4. For the dedicated QCD sample the e+jets and μ+jets event ratio is arbitrary. The e+jets and μ+jets ratio's in the $t\bar{t}$ and W+jets samples differ from those in Table 4.4 due to, for example,

statistical fluctuations, a mis-estimation of the electron reconstruction or selection efficiency, or a mis-estimation of the QCD contribution. Therefore, the μ+jets events in the QCD sample are weighted by a factor 1.35 and μ+jets events in both the $t\bar{t}$ and the W+jets samples are weighted with one common factor of 1.15. After this weighting, in an ensemble test on the combined sample, the ratio of e+jets and μ+jets QCD events is equal to that in Table 4.4 and the total ratio of e+jets and μ+jets events is equal to the ratio observed in data, by construction.

6.2 Signal events only

For illustration and to see the effect of including background events later, first, ensemble tests are performed on pseudo-experiments containing $N = 274$ $t\bar{t}$ events and no background events. The number 274 is the expected number of signal events after application of all selection cuts, including the χ^2 criterion.

Statistical uncertainties

The events used in the pseudo-experiments are drawn from samples of Monte Carlo events with weights (w_i). The effective number of generated Monte Carlo events in a sample is:

$$N_{\text{eff}} = \frac{(\sum_{i=1}^{\text{sample}} w_i)^2}{\sum_{i=1}^{\text{sample}} w_i^2}\,, \tag{6.1}$$

where the sums run over all events in the sample.

When creating event collections containing N events from a sample of N_{eff} effective events, the effective number of independent pseudo-experiments that can be performed, is N_{eff}/N. For signal Monte Carlo events, N_{eff} is of the order of 8000, significantly larger than the size of a pseudo-experiment. This leads to negligible correlation due to multiply selected events within an individual pseudo-experiment. In case of enough oversampling, i.e. if the number of created pseudo-experiments is much larger than the effective number of independent pseudo-experiments, the uncertainty on the fitted mean of an ensemble of pseudo-experiments is given by:

$$\sigma(\text{mean}) = \frac{\sigma}{\sqrt{\frac{N_{\text{eff}}}{N} - 1}}\,, \tag{6.2}$$

where σ is the width of the fitted Gaussian.

The correct jet-parton assignment only

To study the performance of the method, the first ensemble tests use only events that are fully parton-matched and in addition only the correct jet-parton assignment is considered in the computation of the likelihood. The background and combinatorial

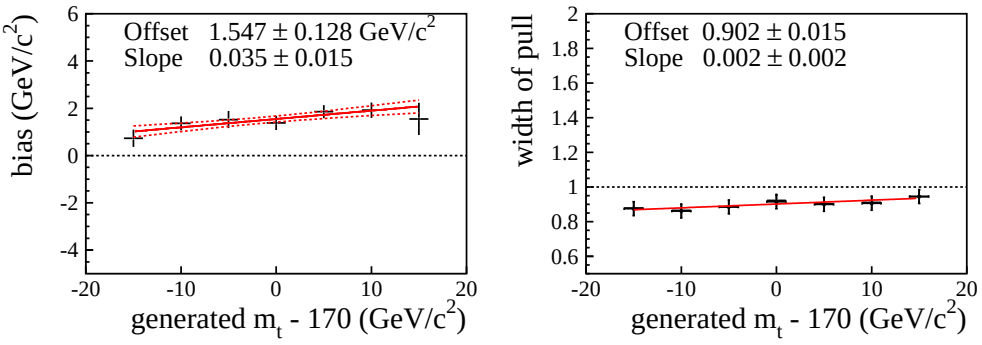

Figure 6.2: *The top quark mass bias (left plot) and the width of the pull of the top quark mass (right plot), when only matched $t\bar{t}$ events are used in the ensemble tests and the likelihood calculation only uses the correct jet-parton assignment and no combinatorial background term is present. The uncertainty band on the fit to the bias is shown by the dashed lines. The χ^2 per degree of freedom of the bias fit is 0.5.*

background terms in the event likelihood are switched off for this study. With these modifications only the term in Eq. 5.17 is left for the calculation of the likelihood.

The top quark mass bias, which is the mean fitted top quark mass minus the input top quark mass, is plotted versus the input top quark mass minus 170 GeV/c^2 in Fig. 6.2. The solid line in the left plot in Fig. 6.2 is a straight line fit. The uncertainty band on the fit, shown by the dashed lines, is computed taking the correlation between the offset and slope of the line into account. To estimate the effect of shifting the calibration curve up and down within its uncertainty, the edges of the error band on the calibration curve are parametrized with second order polynomials.

Even for the correct jet-parton assignment in these matched events, the signal term of the likelihood without the background terms yields a bias on the top quark mass. This bias is probably caused by the non-Gaussian behaviour of parton level corrections. The pull width being approximately 10% smaller than unity shows that the statistical uncertainty is overestimated by typically 10%.

Parton matched events only

Next, ensemble tests are performed on matched events again, but this time all jet-parton assignments are used. Now the wrong jet-parton assignments are included and the combinatorial background term in the likelihood is switched on. Figure 6.3 illustrates that using all jet-parton assignments in the likelihood calculation and including the combinatorial background term slightly decreases the slope of the fit to the bias.

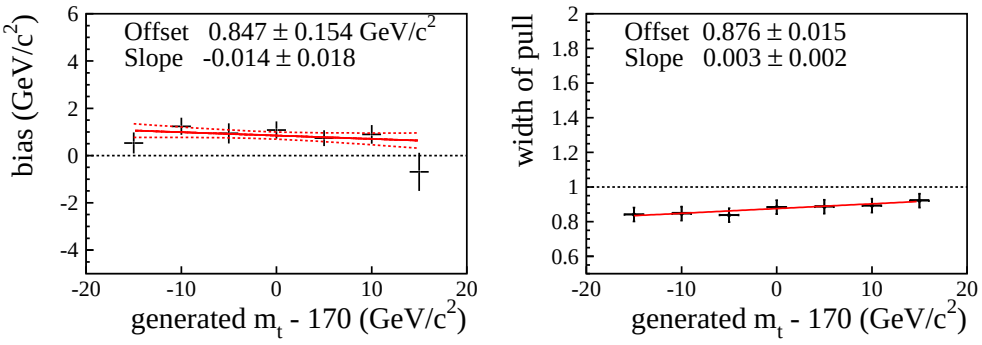

Figure 6.3: *The top quark mass bias (left plot) and the width of the pull of the top quark mass (right plot), when only matched $t\bar{t}$ events are used in the ensemble tests. All jet-parton assignments are used in the likelihood calculation and the combinatorial background term is present. The uncertainty band on the fit to the bias is shown by the dashed lines. The χ^2 per degree of freedom of the bias fit is 1.0.*

All signal events

As a last ensemble test with only signal events, all events are used, not only parton-matched events. The results can be seen in Fig. 6.4. The unmatched events have a

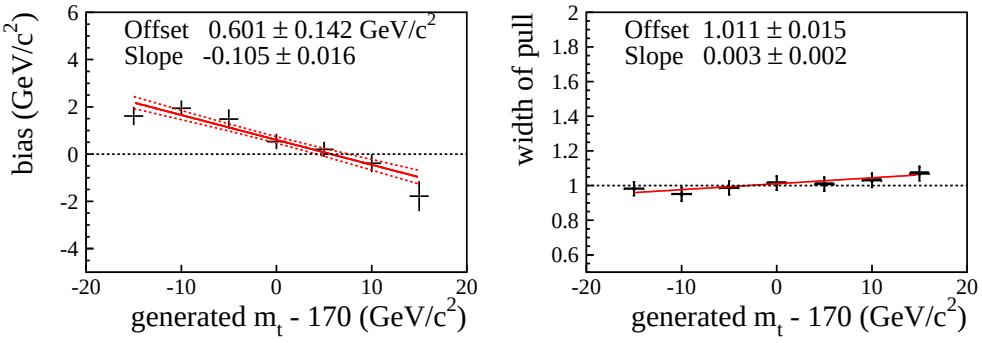

Figure 6.4: *The top quark mass bias (left plot) and the width of the pull of the top quark mass (right plot), when only $t\bar{t}$ events are used in the ensemble tests. The events are not required to be parton-matched. The uncertainty band on the fit to the bias is shown by the dashed lines. The χ^2 per degree of freedom of the bias fit is 1.1.*

significant impact on the top quark mass bias, which becomes more dependent on the top quark mass. This does not come as a surprise: the parton level corrections and resolutions used in the kinematic fit, have been derived on parton-matched events (which comprise only 50.5% of the $t\bar{t}$ sample) and do not have to hold for unmatched events.

6.3 Signal and background events

Finally, ensemble tests are performed using signal and background events in the pseudo-experiments. Each pseudo-experiment consists of 845 events, which is the number of observed data events after the χ^2 cut. Now, the sample purity is no longer fixed, but is fitted simultaneously with the top quark mass. The results of these ensemble tests with the full likelihood calculation can be seen in Fig. 6.5.

Because the events in a pseudo-experiment are now no longer drawn from the same sample and because signal events and background events have an unequal contribution to the likelihood, Eq. 6.2 is no longer valid. The uncertainty on the mean is now approximated by:

$$\sigma(\text{mean}) = \sqrt{\sigma^2_{\text{signal}} + \sigma^2_{\text{BG}}}\,. \tag{6.3}$$

The first term on the right hand side, σ_{signal}, comes from the ensemble tests with only signal events and is given by Eq. 6.2. The second term on the right hand side, σ_{BG}, is the uncertainty on the ensemble mean coming from the background events. It is determined as follows. The W+jets sample is cut in four subsamples. Then, an ensemble test containing $t\bar{t}$ events with an input top quark mass of 170 GeV/c^2, W+jets events, and QCD events is performed on each of the W+jets subsamples. The RMS of the set of 4 ensemble means is 0.9 GeV/c^2, implying an uncertainty on the sample mean of $0.9/\sqrt{3}$ =0.53 GeV/c^2 due to the W+jets events. Because the QCD contribution is small, it is neglected here.

Figure 6.6 shows the bias of the fitted purity in the ensemble tests versus the input top quark mass and versus the input purity. In the left plot the purity used in the ensemble tests is 32.4%, taken from Table 4.4. Events with a true top quark mass of 175 GeV/c^2 are used in the ensemble tests for the right plot of the figure. Figure 6.7 shows the calibrated top quark mass versus the input purity in ensemble tests on a sample with an input top quark mass of 175 GeV/c^2.

It should be noted that the input purity per pseudo-experiment is not equal to the input purity of the entire ensemble. The input purity of a pseudo-experiment is taken from a Poisson distribution around the input purity of the ensemble. Therefore, the widths of the purity fits in ensemble tests come from both the spread in input purities and the uncertainty on the purity fitting procedure.

Ultimately, the fitted top quark mass is calibrated using the straight line fit of the

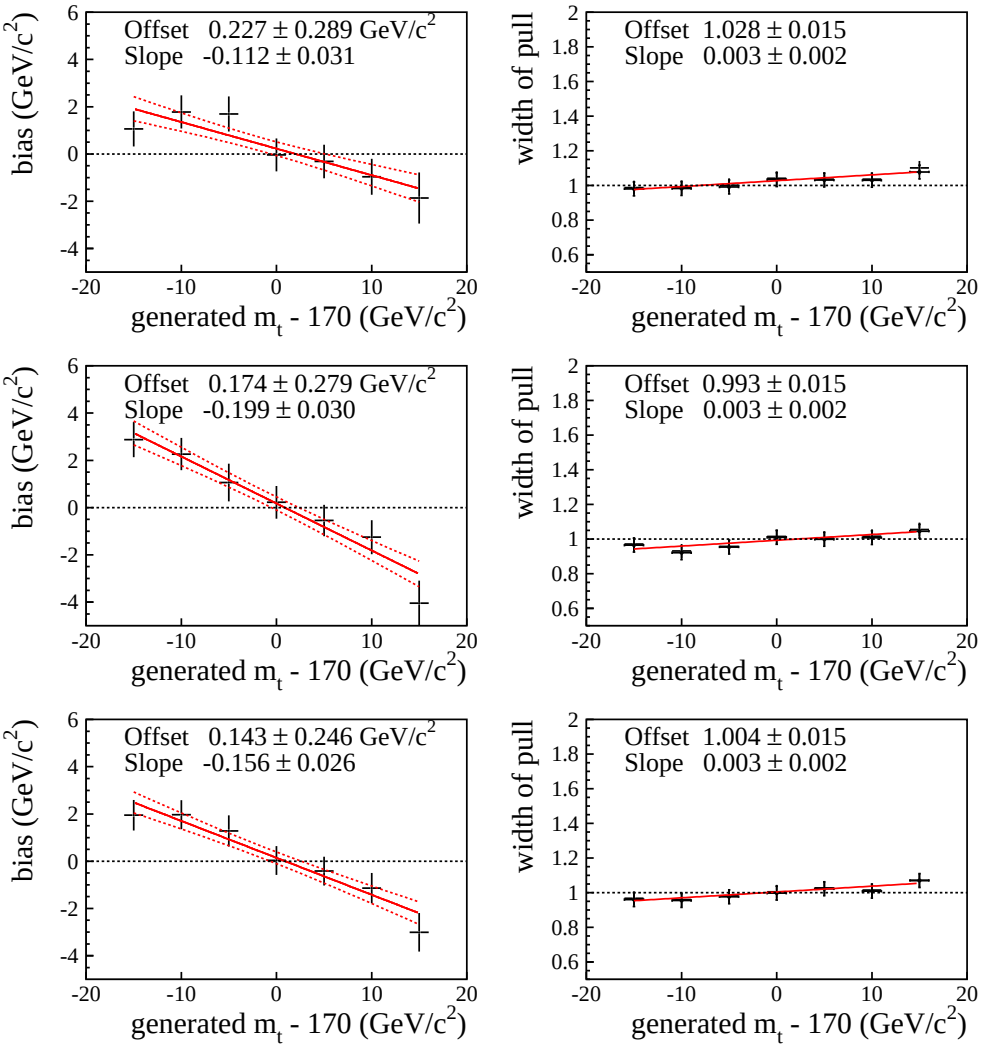

Figure 6.5: *The top quark mass bias (left plots) and the width of the pull of the top quark mass (right plots). The pseudo-experiments contain $t\bar{t}$, W+jets and QCD events. The purity is fitted simultaneously with the top quark mass. The uncertainty band on the fit to the bias is shown by the dashed lines. The upper plots show the e+jets channel; the middle plots show the μ+jets channel and the lower plots show the combined channel. The χ^2's per degree of freedom of the bias fits are 0.7 (e+jets), 0.5 (μ+jets), and 0.5 (combined).*

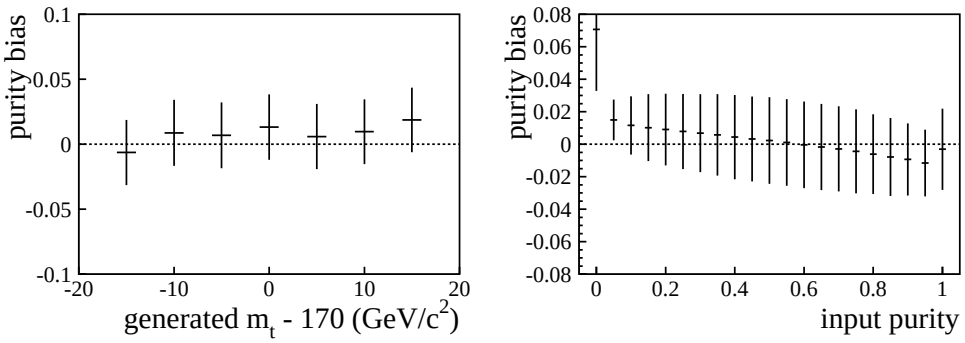

Figure 6.6: *The bias of the fitted purity versus the input top quark mass (left), in ensemble tests with an input purity of 32.4%, and versus the input purity for an input top quark mass of 175 GeV/c^2 (right). The uncertainty bars are the widths of the Gaussian fits to the fitted purity.*

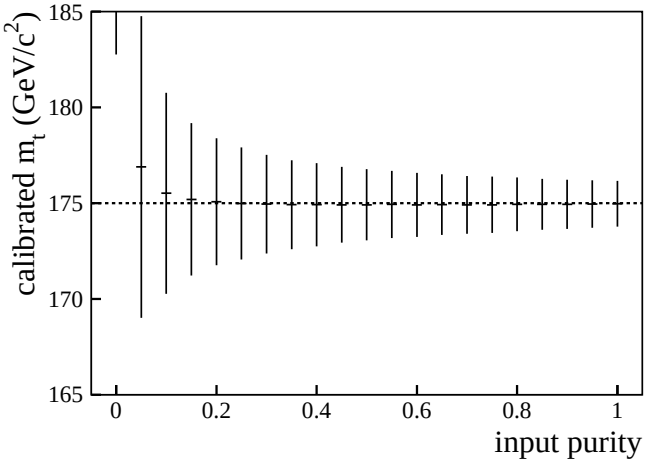

Figure 6.7: *The calibrated fitted top quark mass versus the input purity, in ensemble tests with an input top quark mass of 175 GeV/c^2. The uncertainty bars are the widths of the Gaussians fitted to the distributions of the fitted top quark mass.*

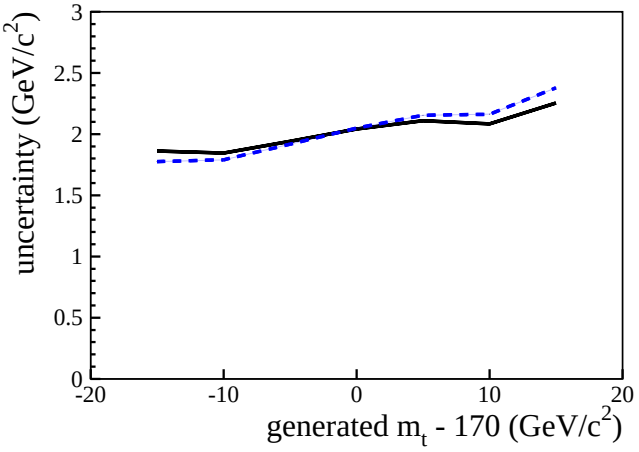

Figure 6.8: *The statistical uncertainty (solid) before correction versus top quark mass. The dashed line has been corrected for the width of the pull using the fit shown in Fig. 6.5, and represents the expected statistical uncertainty.*

combined sample in Fig. 6.5. The straight line fit to the bias is inverted to obtain:

$$m_t = \frac{m_{\rm fit} + S \cdot 170\,{\rm GeV}/c^2 - O}{1+S}\,, \tag{6.4}$$

where O is the offset and S is the slope. The second order polynomial fits to the edges of the uncertainty interval are inverted to obtain:

$$m_t = 170\ {\rm GeV}/c^2 + \frac{-p_1 - 1 + \sqrt{(p_1+1)^2 - 4p_2(p_0 - m_{\rm fit} + 170\ {\rm GeV}/c^2)}}{2p_2}, \tag{6.5}$$

with $p_0 = 0.40$ GeV/c^2, $p_1 = -0.15$ and $p_2 = 0.0010$ (GeV/c^2)$^{-1}$ for the calibration curve shifted up and $p_0 = -0.11$ GeV/c^2, $p_1 = -0.16$ and $p_2 = -0.0010$ (GeV/c^2)$^{-1}$ for the calibration curve shifted down.

In addition, the estimated statistical uncertainties are corrected for the pull width as a function of top quark mass, as shown in Fig. 6.8. The expected statistical uncertainty is 2.02 GeV/c^2 for a true top quark mass of 170 GeV/c^2.

Chapter 7

Result

In this chapter the measurement of the top quark mass from the data sample corresponding to 1 fb^{-1} (described in Chapter 4) is presented. In Section 7.1 the top quark mass is extracted using the ideogram algorithm (described in Chapter 5 and calibrated using the results described in Chapter 6. Some cross checks on the data sample are shown in Section 7.2, while Section 7.3 describes the sources of systematic uncertainties on the measurement. In Section 7.4 the result of this measurement is compared to other top quark mass measurements.

7.1 Result on data

The likelihood values, $\mathcal{L}$, obtained in data are shown as a function of the top quark mass in Fig. 7.1 (left) together with a Gaussian fit. Figure 7.1 (right) shows the quantity $-2\ln(\mathcal{L})$ as a histogram, together with a fitted parabola. The fit illustrates that the likelihood behaves Gaussian over a rather large range. The uncalibrated top quark mass is obtained as described in Section 5.5 using a parabola 'fitted' to the bin with the minimal value of $-2\ln(\mathcal{L})$ and its two neighbours, as is shown in Fig. 7.2.

Before calibration a fitted top quark mass of 175.57 ± 1.88 (stat.) GeV/c^2 is found. After full calibration using the curve displayed in Fig. 6.5, the result is:

$$m_t = 176.4 \pm 1.9 \text{ (stat.) GeV}/c^2 \,.$$

The top quark masses in the separate channels, calibrated individually, are:

$$m_t = 177.6 \pm 2.8 \text{ (stat.) GeV}/c^2 \qquad (e + \text{jets})$$

and

$$m_t = 175.2 \pm 2.6 \text{ (stat.) GeV}/c^2 \qquad (\mu + \text{jets}) \,.$$

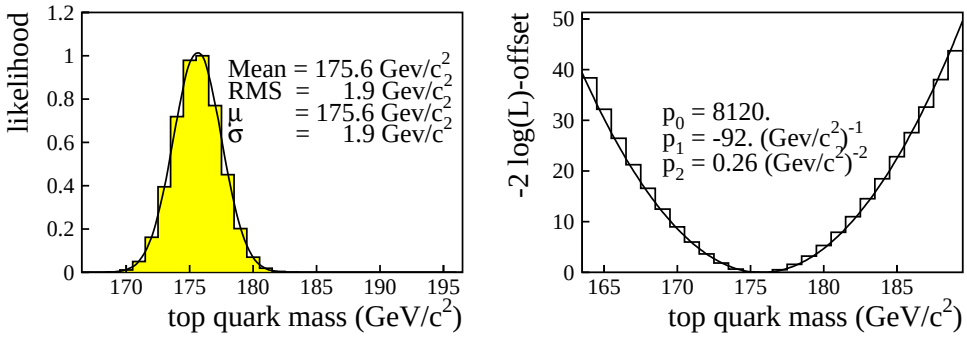

Figure 7.1: *The top quark mass likelihood observed in data. The left plot shows the likelihood peak with a Gaussian fit. The right plot shows* $-2\ln(\mathcal{L})$ *with a parabolic fit.*

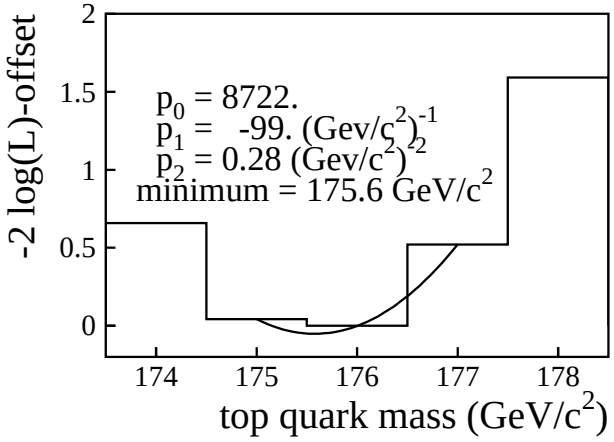

Figure 7.2: $-2\ln(\mathcal{L})$ *observed in data in the region of interest. A parabola is used to describe the shape of the histogram in the bin with the minimal value of* $-2\ln(\mathcal{L})$ *and its two neighbouring bins. The minimum of the parabola is the uncalibrated fitted top quark mass.*

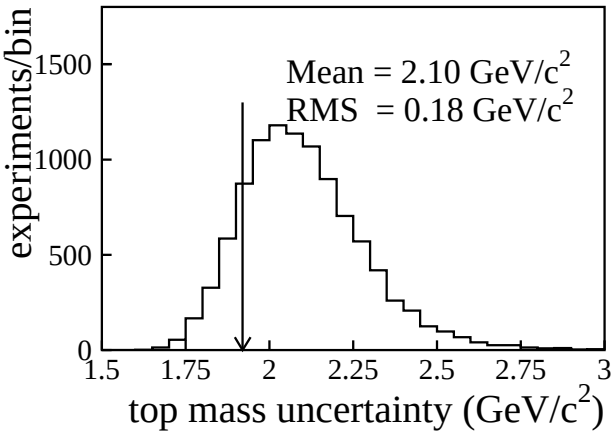

Figure 7.3: *The distribution of the expected calibrated statistical uncertainty for a top quark mass of 175 GeV/c^2. The arrow indicates the corrected statistical uncertainty observed in data.*

The purities, also obtained in the likelihood fit are 0.338 ± 0.035 (stat.) and 0.364 ± 0.036 (stat.) in the e+jets and μ+jets channel respectively. The fitted purity in the combined channel is 0.350 ± 0.025 (stat.), which is consistent with the result of the discriminant fit.

The statistical uncertainty observed in data is compared to the expected uncertainty from pseudo-experiments with an input top quark mass of 175 GeV/c^2 in Fig. 7.3. The statistical uncertainty observed in data is consistent with the expectation from Monte Carlo simulation.

7.2 Cross checks

As a cross check the top quark mass measurement is performed on events with exactly four jets with $p_T > 20$ GeV/c. There are 374 e+jets and 334 μ+jets events with four jets. New calibration curves are derived from pseudo-experiments with the fractions from Table 4.4. The result on 4-jets data events is:

$$\begin{aligned} m_t &= 176.8 \pm 3.2 \text{ (stat.) GeV}/c^2 \ (e\text{+jets}) \\ m_t &= 177.2 \pm 3.0 \text{ (stat.) GeV}/c^2 \ (\mu\text{+jets}) \\ m_t &= 177.0 \pm 2.1 \text{ (stat.) GeV}/c^2 \ \text{(combined)} \end{aligned}$$

These measurements are consistent with those on the full data sample. On the complementary sample, containing events with more than four jets with $p_T > 20$ GeV/c,

the measured top quark mass is:

$$\begin{aligned} m_t &= 186.4 \pm 7.4 \text{ (stat.) GeV}/c^2 \ (e\text{+jets}) \\ m_t &= 172.4 \pm 7.0 \text{ (stat.) GeV}/c^2 \ (\mu\text{+jets}) \\ m_t &= 175.0 \pm 4.7 \text{ (stat.) GeV}/c^2 \ \text{(combined)} \end{aligned}$$

Secondly, the data sample is split according to the number of b tags. The signal fractions cannot be taken from Table 4.4, because the signal fraction depends on the number of b tags required. Therefore, the estimated signal fractions in the different b tag bins in Fig. 4.13 are used in the ensemble tests. On the combined electron and muon sample, the top quark mass is measured to be:

$$\begin{aligned} m_t &= 174.6 \pm 2.1 \text{ (stat.) GeV}/c^2 \ (1\ b \text{ tag}) \\ m_t &= 178.1 \pm 4.0 \text{ (stat.) GeV}/c^2 \ (\geq 2\ b \text{ tags}) \end{aligned}$$

With 220 events with 1 b tag and 71 events with ≥ 2 b tags, statistics for these measurements are considerably smaller than in the total data sample. The measurements on the sample split according to the number of b tags are consistent with the measurement on the total data sample. For events with 0 b tags the maximum of the likelihood is at zero purity. At zero purity the likelihood is flat as a function of the top quark mass. Therefore, no top quark mass is measured on events with 0 b tags.

7.3 Systematic uncertainties

Because the analysis is calibrated with Monte Carlo events, the systematic uncertainty must include possible discrepancies between data and Monte Carlo simulation. As described in Section 3.3, the Monte Carlo events have been adjusted for known differences with data, such as additional smearing of jet energies and reweighting according to luminosity. To estimate the effect of the uncertainty on the Monte Carlo corrections, the corrections are varied within their 1 σ uncertainty. Ensemble tests are performed on these modified Monte Carlo events to obtain the corresponding calibration curves. The data is calibrated with the new calibration curves and the differences of the new result for m_t with the nominal value of 176.4 GeV/c^2 are taken as systematic uncertainties.

The sources of systematic uncertainties coming from the possible difference between data and Monte Carlo are:

- **Jet energy scale:** the jet energy scales for data and Monte Carlo events both have an uncertainty. Because both data and Monte Carlo events are used in this analysis, the data and Monte Carlo jet energy scale uncertainties are summed in quadrature to obtain the total jet energy scale uncertainty. To determine its effect on the top quark mass, ensemble tests are performed

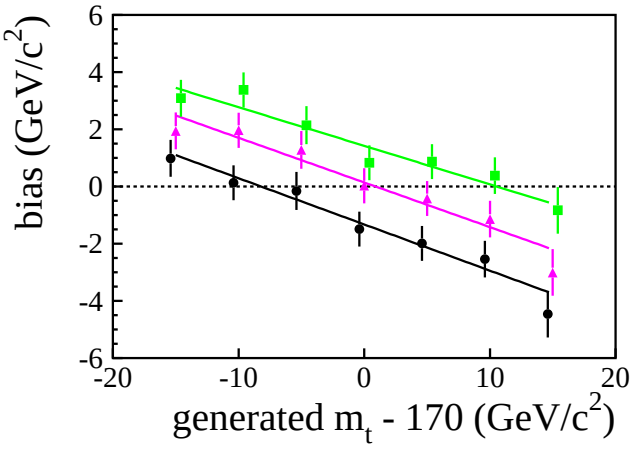

Figure 7.4: *Straight line fits to the bias in fitted top quark mass for Monte Carlo samples reconstructed with the JES shifted up (squares, upper line), the nominal JES (triangles, middle line) and the JES shifted down (dots, lower line).*

with several Monte Carlo input top quark masses. The JES applied to $t\bar{t}$ and W+jets events is shifted up and down by 1 σ from its central value and calibration curves are obtained. The results are shown in Fig. 7.4 together with the nominal result. Application of the calibration curve obtained with the JES shifted up (down), on the uncalibrated data result, leads to a top quark mass of 174.84 GeV/c^2 (178.25 GeV/c^2). The differences with 176.4 GeV/c^2, -1.61 GeV/c^2 and 1.80 GeV/c^2, are quoted as systematic uncertainties. The JES in the QCD events used for the ensemble tests is kept unchanged, as these are data events.

Consistency of the jet energy scale ratio between data and Monte Carlo simulation can also be verified with a comparison of the W boson mass peaks in data and Monte Carlo simulation, which is described here as an additional check. A Gaussian shape is fitted to the distribution of the reconstructed W boson mass (M_W) of the best (lowest χ^2) jet-parton assignment in data, as shown in the upper left plot of Fig. 7.5. The same is done for a Monte Carlo sample containing $t\bar{t}$ (m_t = 170 GeV/c^2), W+jets, and QCD events with a sample composition according to the ratio's of Table 4.4 (see the upper right plot of Fig. 7.5). The difference between the means of the Gaussians fitted in data and Monte Carlo simulation is $\delta_{\mathrm{MC-data}} = 0.0 \pm 0.9$ GeV/c^2. To demonstrate the effect of a different JES, the jets in data events are scaled by an additional JES factor in the range between 0.94 and 1.06, before the event selection. The range

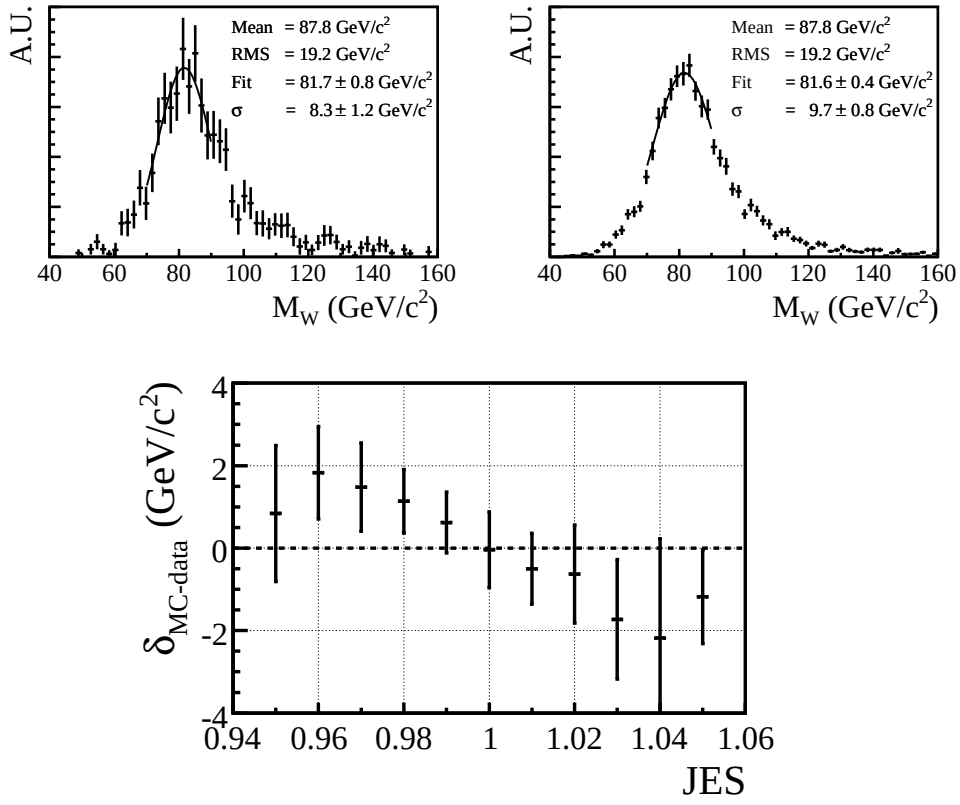

Figure 7.5: *Results of a study of the compatibility of the JES in data and Monte Carlo simulation. The upper plots show the distribution of the W boson mass peak in data (left) and Monte Carlo simulation (right) with fitted Gaussian shapes. The lower plot shows* $\delta_{\mathrm{MC-data}}$*, which is the mean of the Gaussian shape fitted to the Monte Carlo distribution minus the mean of the Gaussian shape fitted to the data distribution, versus an additional JES factor applied to data.*

from 0.94 to 1.06 is used, because it is larger than the relative uncertainty on the JES itself. For each JES factor, the difference $\delta_{\mathrm{MC-data}}$ is determined. The differences are shown versus the JES factor in Fig. 7.5. This study shows that the data and Monte Carlo jet energy scales are compatible, but a 2 % deviation cannot be excluded, which can be concluded from by observing the range in the JES factor for which the 'band' cuts the line $\delta_{\mathrm{MC-data}} = 0$. Hence, this method is not powerful enough to replace the nominal JES or improve its uncertainty.

- **Preliminary jet energy scale:** after this analysis was performed, the DØ jet energy scale was studied in more detail. It is (conservatively) estimated that the ratio of the so called final jet energy scale for data over the final jet energy scale for Monte Carlo is at most 0.15% lower than this ratio of the jet energy scale used in this analysis [94]. This indicates that the jets in data in this analysis are more energetic than the jets in the Monte Carlo events. To estimate the effect of this difference the jet energies in data are scaled down by 0.15% and the difference with 176.4 GeV/c^2 is quoted as a systematic. This difference is -0.35 GeV/c^2. This uncertainty is added linearly to the other systematic uncertainties, because its expectation value is not zero, due to its special origin.

- **Jet energy scale sample dependence:** the main component of the JES, the response (R), was derived from photon+jet events. The sample used here contains more quark instead of gluon jets and more b jets and c jets. The possible sample dependence of the JES must be investigated so that it can either be corrected for or applied as a systematic uncertainty. As with the previous systematic uncertainty, this only has an effect on the top quark mass measured on data events, if the ratio of the response to the jets used in this analysis and the response to the jets in the photon+jet sample is different in data and Monte Carlo. This double ratio has been studied by using single-particle response parametrizations measured in data and also obtained from Monte Carlo events. The two parametrizations are applied to the Monte Carlo particles in jets in $t\bar{t}$ and photon+jet samples generated with the next-to-leading order Monte Carlo generator MC@NLO. The ratio's of the response using the parametrizations of data and Monte Carlo are $R^{t\bar{t}}_{\mathrm{data}}/R^{\gamma\mathrm{j}}_{\mathrm{data}}$ and $R^{t\bar{t}}_{\mathrm{MC}}/R^{\gamma\mathrm{j}}_{\mathrm{MC}}$, respectively. The double ratio $\frac{R^{t\bar{t}}_{\mathrm{data}}/R^{\gamma\mathrm{j}}_{\mathrm{data}}}{R^{t\bar{t}}_{\mathrm{MC}}/R^{\gamma\mathrm{j}}_{\mathrm{MC}}}$ is determined as a function of the jet energy. The double ratio is close to unity. Because it was derived with less precision than the JES, the Monte Carlo jets in this analysis are not corrected for the sample dependence of the JES, but a systematic uncertainty is assigned. To study the effect of this double ratio not being unity, the jets in the $t\bar{t}$ Monte Carlo events are corrected to look more like the data jets. Only the jets in the $t\bar{t}$ Monte Carlo are corrected and not those in the W+jets Monte Carlo, because $t\bar{t}$ events contribute most to the mass analysis. A new calibration curve is derived from the corrected Monte Carlo events, which is the line through the downward triangles in Fig. 7.6. This

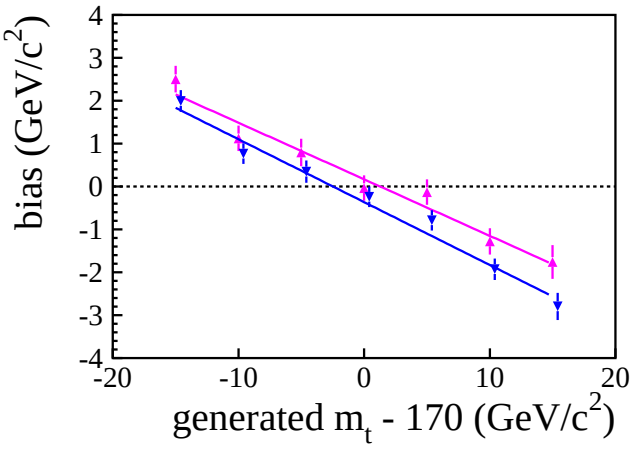

Figure 7.6: *The two lines fitted to the Monte Carlo sample reconstructed with the final JES. The upward triangles do not have the sample dependent correction as described in the text. The downward triangles have the sample dependent correction for the JES applied.*

new calibration curve cannot easily be compared to the nominal calibration curve without the sample dependent correction, because in this study the final JES was used. Therefore, a new nominal calibration curve is derived with the final JES, without the sample dependent correction. This is the line through the upward triangles in Fig. 7.6. The difference in top quark mass measured on data calibrated with these two calibration curves is $+0.63$ GeV/c^2, which is quoted as a systematic uncertainty. Note that this systematic uncertainty includes the uncertainty on the b jet energy scale.

- **Jet energy resolution:** the jet energy smearing described in Section 3.3 has an uncertainty. To estimate its effect on the top quark mass fit, the smearing is varied by ± 1 σ and the W+jets and $t\bar{t}$ Monte Carlo samples are reprocessed. New calibration curves are obtained. Calibration of the top quark mass in data with these calibration curves gives shifts of -0.50 GeV/c^2 (more smearing) and -0.45 GeV/c^2 (less smearing). The largest of these is quoted as a systematic uncertainty in both directions.

- **Jet identification efficiency:** the difference in jet identification efficiency between data and Monte Carlo, described in Section 3.3, has an uncertainty. The effect of a lower identification efficiency is mimicked by removing more Monte Carlo jets. However, the uncertainty on the identification efficiency is compat-

ible with the data efficiency being higher than the Monte Carlo efficiency. It is not possible to add jets to the Monte Carlo events. Therefore, only the effect of a downward shift of the identification efficiency is measured and the resulting uncertainty is quoted in both directions. The shift is determined separately for jets in the CC and jets in the ICR. New calibration curves are determined and the effects on the top quark mass measurement turn out to be -0.69 GeV/c^2 (CC) and -0.36 GeV/c^2 (ICR), which in quadrature gives a total jet identification systematic uncertainty of -0.78 GeV/c^2. This is quoted in both directions.

- $\not\!\!E_T$ **uncertainty:** the uncertainty on the simulation of $\not\!\!E_T$ is already largely covered by the systematic uncertainty due to the JES uncertainty. In the μ+jets channel in Fig. 4.12 the distribution of $\not\!\!E_T$ in data peaks at a higher value than in Monte Carlo simulation. This may be due to statistical fluctuations or to an inadequate simulation of $\not\!\!E_T$. To ensure that this has no large effect on the top quark mass measurement, the following additional check is performed. The data distribution of $\not\!\!E_T$ in the muon channel is divided by the Monte Carlo distribution to obtain weights for the Monte Carlo events. Ensemble tests are performed on the reweighted μ+jets events to obtain a calibration curve. Calibration of the data in the μ+jets channel gives a shift of -0.24 GeV/c^2, well covered by the systematic uncertainty from the JES. Because this effect may be largely caused by a statistical fluctuation, this shift is not added as a systematic uncertainty.

- **Trigger uncertainty:** to address uncertainties from the trigger efficiencies, the trigger turn-on curves, applied to Monte Carlo events, are shifted up and down by 1 σ. Calibration curves are obtained and application of these curves leads to top quark mass shifts of $+0.14$ GeV/c^2 (trigger turn-on up) and -0.39 GeV/c^2 (trigger turn-on down).

- **Signal modelling:** the difference between $t\bar{t}$ events generated by Pythia and $t\bar{t}$ events in data is expected to be mainly a difference of the jet multiplicity and the E_T spectrum of the jets. To quantify this difference the jet multiplicity in $t\bar{t}$ Monte Carlo events is compared with the jet multiplicity in $t\bar{t}$ data events. To obtain a pure signal sample, only events with two or more b tags are used for this study. The jet multiplicity is binned in events with four jets and events with five or more jets. The jet multiplicity distributions of data and Monte Carlo simulation are normalized to the same number and then the distribution in data is divided by the distribution in Monte Carlo, to get the scale parameters by which the Monte Carlo weights have to be multiplied to mimic the jet multiplicity in data. Figure 7.7 shows this data and Monte Carlo ratio. Ensemble tests are performed to obtain new calibration curves on samples in which the weights of $t\bar{t}$ events are scaled by the extremes of the error bars, i.e. one set of ensemble tests is performed with scaling factors $0.90 - 0.14$ (4 jets) and $1.17 + 0.21$ (≥ 5

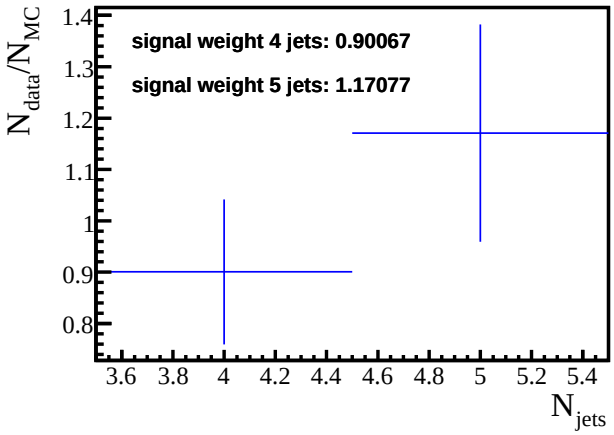

Figure 7.7: *The data and Monte Carlo ratio of the fraction of events with 4 jets and 5 or more jets in events with at least 2 b tags. The Monte Carlo events are $t\bar{t}$ events with an input top quark mass of 175 GeV/c^2.*

jets) (jet multiplicity up), while another set of tests is performed with scaling factors of $0.90 + 0.14$ (4 jets) and $1.17 - 0.21$ (≥ 5 jets) (jet multiplicity down). Calibration with these curves gives shifts of -0.01 GeV/c^2 (jet multiplicity up) and +0.01 GeV/c^2 (jet multiplicity down), which are quoted as a systematic uncertainty.

- **Background modelling:** the heavy flavour scale factor of 1.17 for W+jets background events, introduced in Section 3.1, has an uncertainty of ± 0.18. Ensemble tests are performed with the heavy flavour scale factor shifted up and down by 0.18 for the W+jets events. Calibration with the curves obtained with these ensemble tests, gives shifts of +0.18 GeV/c^2, both when shifting the heavy flavour scale factor up and down. This difference is quoted in both directions.

- **Luminosity reweighting:** after the luminosity reweighting, described in Section 3.3, which aimed to make the vertex multiplicity distributions of data and Monte Carlo agree, these two distributions of the selected samples do not agree well. Therefore, a systematic uncertainty is assigned due to the uncertainty on the amount of minimum bias overlays in Monte Carlo events. The Monte Carlo events used in the ensemble tests are reweighted according to the data and Monte Carlo ratio of the vertex multiplicity after the event selection. The ratio of the distributions of the vertex multiplicity in data and Monte Carlo is displayed in Fig. 7.8 and indicates that the amount of events with many minimum bias overlays is underestimated in Monte Carlo. The Monte Carlo

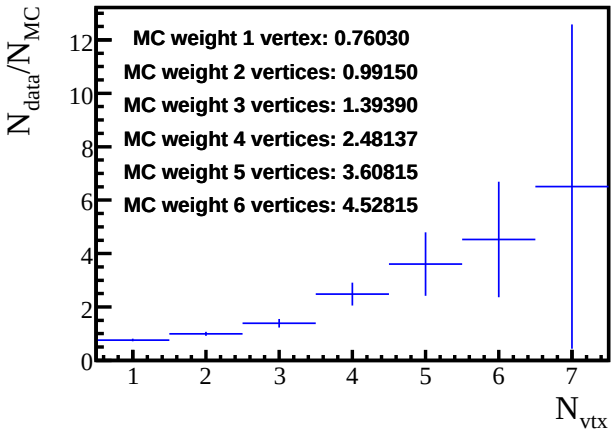

Figure 7.8: *The data and Monte Carlo ratio of the fraction of events with a certain vertex multiplicity. The $t\bar{t}$ Monte Carlo events have an input top quark mass of 175 GeV/c^2. The estimated QCD contribution has been subtracted from the data.*

events are reweighted and new calibration curves are obtained. The difference of -0.08 GeV/c^2 is quoted as a systematic uncertainty.

- **Tagging of b jets:** to estimate the effect of the uncertainty on the Monte Carlo tag rate functions for b, c, and light jets, calibration curves are obtained from Monte Carlo events in which the tag rate function for b jets and the fake rate for both c and light jets are shifted separately when assigning the b tags to the jets. Calibration with the obtained calibration curves with the tag rate functions shifted gives +0.01 GeV/c^2 (tag rate functions down) and +0.16 GeV/c^2 (tag rate functions up). Calibration with the calibration curves with the fake rates shifted gives shifts of -0.09 GeV/c^2 (fake rates down) and +0.09 GeV/c^2 (fake rates up). Values of -0.09 GeV/c^2 and +0.18 GeV/c^2 are used as the systematic uncertainties.

- **PDF uncertainty:** in Ref. [87], a preliminary version of this analysis on a smaller data set is described. The uncertainty due to the PDF set is extensively studied there, demonstrating that only relatively small effects are expected. This uncertainty includes the effects of variations in the next-to-leading order PDF set CTEQ6M [95] instead of the normal CTEQ6M PDF set and the difference between the use of PDF set CTEQ5L [96] and a different PDF set, MRST [97]. For technical reasons this study cannot be redone easily. It is not expected that the uncertainty due to the uncertainty on the PDFs changes much with respect to Ref. [87]. Therefore, to address the systematic uncertainty

caused by the uncertainty on the PDF set, the value ± 0.023 GeV/c^2, quoted in Ref. [87], is taken.

- **QCD selection:** the QCD events used in the ensemble tests to calibrate the analysis, are taken from data and thus no difference between data and Monte Carlo simulation has to be addressed for the QCD events. There may be a difference between these events and the QCD events in the data sample, because of the inversion of the isolation cut for electrons and the replacement of the tight requirement for muons, but this effect is expected to be negligible.

There are three possible sources of systematic uncertainty that do not originate from a possible difference between data and Monte Carlo events. These are:

- **signal fraction:** the fraction of $t\bar{t}$ events used in the ensemble tests has an uncertainty coming from the uncertainty on the fraction from the discriminant template fit. The uncertainty on the signal fraction of 32.4% is ± 4.6%. The signal fraction is varied accordingly and new calibration curves are obtained. Calibration of the data results in shifts of +0.02 GeV/c^2 (signal fraction down) and -0.05 GeV/c^2 (signal fraction up).

- **QCD fraction:** the QCD fraction in the ensemble tests is taken from Ref. [69], which also quotes an uncertainty on the QCD fraction. The analysis described in Ref. [69] does not use the exact same event selection as this analysis, but the difference in the QCD fraction is expected to be small and at most 40% different for the most conservative estimate. The systematic uncertainty due to the uncertainty on the QCD fraction is estimated by shifting the amount of QCD up and down in ensemble tests by 1.4 times the uncertainty quoted in Ref. [69]. The fractions of QCD are then 14.3% and 10.9% of the total sample instead of 12.6%. New calibration curves are obtained, which shift the calibrated data result by +0.10 GeV/c^2 (QCD fraction down) and -0.11 GeV/c^2 (QCD fraction up).

- **Limited Monte Carlo statistics:** the finite size of the Monte Carlo event sample leads to statistical uncertainties on the mean fitted top quark masses in ensemble tests. These uncertainties lead to the error bands on the calibration curve as shown in Fig. 6.5. To estimate the effect of shifting the calibration curve up and down within its uncertainty, the edges of the uncertainty interval of the calibration curve, as parametrized in Eq. 6.5, are applied as calibration to the data, leading to shifts of +0.25 GeV/c^2 (calibration down) and -0.25 GeV/c^2 (calibration up). These are used as systematic uncertainty.

Table 7.1 lists the systematic uncertainties. The dominant systematic effect comes from the JES related uncertainties, followed by the jet identification. The other uncertainties are typically one order of magnitude smaller. Adding all positive and negative

source	systematic uncertainty (GeV/c^2)	
JES	+1.80	-1.61
final/preliminary JES		-0.35 (linear)
JES sample dependence	+0.63	
JER	± 0.50	
jet identification	± 0.78	
trigger uncertainty	+0.14	-0.39
signal modelling	+0.01	-0.01
background modelling	± 0.18	
luminosity reweighting		-0.08
b-tagging	+0.18	-0.09
PDF uncertainty	±0.02	
signal fraction	+0.02	-0.05
QCD fraction	+0.10	-0.11
limited MC statistics	+0.25	-0.25
T O T A L	+2.16	-2.28

Table 7.1: *The systematic uncertainties on the measured top quark mass.*

uncertainties in quadrature gives a total systematic uncertainty of +2.2 GeV/c^2 and -2.3 GeV/c^2, respectively. Hence, the top quark mass is measured to be:

$$m_t = 176.4 \pm 1.9 \text{ (stat.)}^{+2.2}_{-2.3} \text{ (syst.) GeV}/c^2 \,.$$

7.4 Comparison with other measurements

Several top quark mass analyses have been performed by DØ and CDF. Figure 7.9 shows the public results as of March 2008. The CDF and DØ Run II measurements in the semi-leptonic channel have smaller uncertainties than the measurement presented here. This is partially because these measurements were performed on a larger data set of 2.1 fb^{-1}. The measurement in this thesis can best be compared to the DØ measurement in the semi-leptonic channel using the matrix element method on a similar data set, as described in Ref. [84]. The result of that measurement is 171.5 ± 1.8 (stat.+JES) ± 1.1 (syst.) GeV/c^2. The statistical uncertainty and the uncertainty due to the jet energy scale (JES) are grouped, because that analysis fits a JES factor. Via this fit the top quark mass measurement may be influenced by statistical fluctuations, to which the ideogram method without a JES factor fit is insensitive.

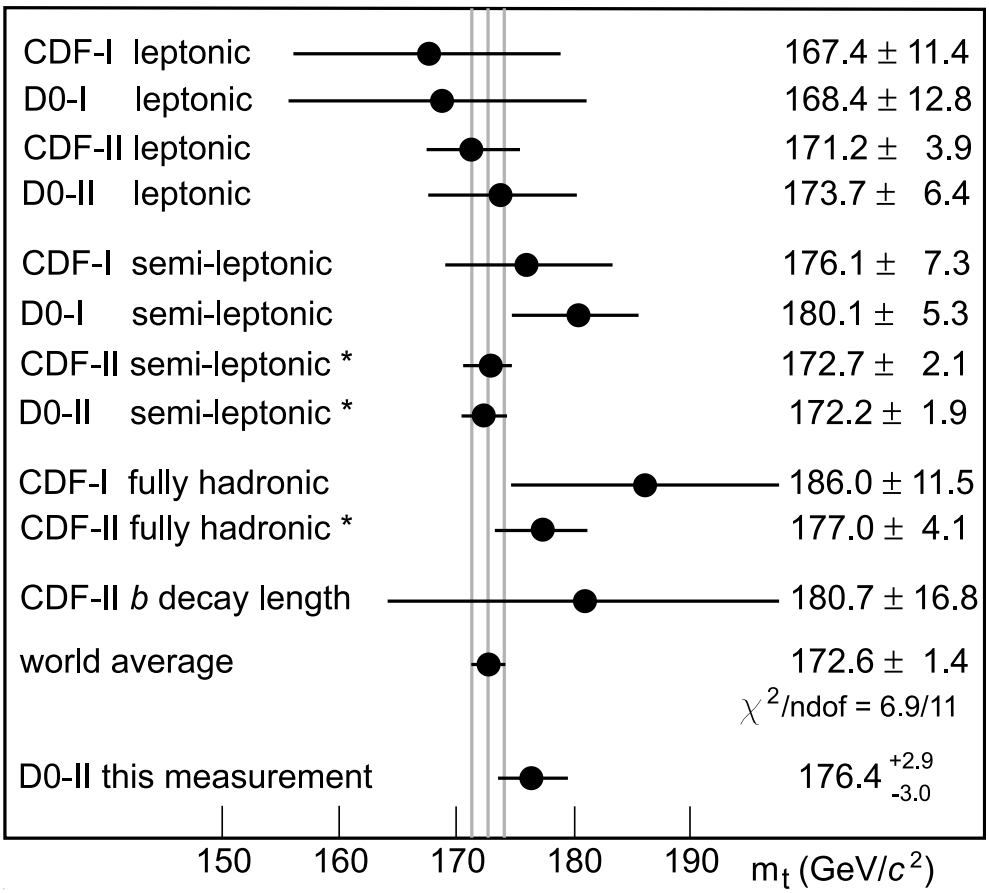

Figure 7.9: *The published and preliminary (*) measurements of the top quark mass as of March 2008 and the measurement presented in this thesis. The world average (not including this measurement) is also shown. The grey lines shows the uncertainty interval of the world average.*

Notably, both the statistical (including JES) and the systematic uncertainty of the matrix element measurement are smaller than in this measurement. The matrix element technique uses the event kinematics optimally and apparently better than the described ideogram technique. The matrix element analysis also uses b tagging in a different way: instead of either assigning a b tag or not assigning a b tag to each jet, a probability that a jet is a b jet is assigned. Both effects result in a smaller statistical uncertainty. The systematic uncertainty of the matrix element analysis is smaller, because most JES related uncertainties are calibrated out with the JES factor fit. When the residual JES related uncertainty of 0.8 GeV/c^2 is subtracted from the total systematic uncertainty, the result is ± 0.7 GeV/c^2, which is smaller than the systematic uncertainty of the ideogram measurement without the JES related uncertainties, which is $+1.0$ GeV/c^2 and -1.1 GeV/c^2.

Due to the fitted JES factor in the matrix element analysis, that result cannot be easily compared to this result. This result should be compared to the result obtained with the matrix element method without fitting the JES factor. If the JES factor is not fitted, the matrix element analysis measures a top quark mass of 172.9 $\pm$ 1.4 (stat.) GeV/c^2 [98]. The important quantity is the significance of the difference between the two measurements, which is given by:

$$\text{significance} = \frac{|(m_t^{\text{ID}} - m_t^{\text{ME}}) - \langle m_t^{\text{ID}} - m_t^{\text{ME}} \rangle|}{\sigma(m_t^{\text{ID}} - m_t^{\text{ME}})}\,, \tag{7.1}$$

with m_t^{ID} and m_t^{ME} the result of, respectively, the ideogram analysis and the matrix element analysis, $\langle m_t^{\text{ID}} - m_t^{\text{ME}} \rangle$ their expected difference, and $\sigma(m_t^{\text{ID}} - m_t^{\text{ME}})$ the standard deviation of the difference. Because both analyses are expected to obtain the same top quark mass, $\langle m_t^{\text{ID}} - m_t^{\text{ME}} \rangle$ is 0 GeV/c^2. The quantity $\sigma(m_t^{\text{ID}} - m_t^{\text{ME}})$ is obtained from ensemble tests described in Appendix A and is found to be 2.3 GeV/c^2, with a correlation of the two methods of 35 %. This leads to a significance of the observed difference between the two top quark mass measurements of 1.6. The probability to obtain a significance larger than 1.6 is 12 %.

Figure 7.9 also shows the world average as calculated by the Tevatron Electroweak Working Group [99] and the measurement presented in this thesis. The uncertainty intervals of this measurement and the world average overlap. The difference between this measurement and the world average is 1.2 times the quadratic sum of the uncertainties. It is not trivial to combine this measurement with other top quark mass measurements or the world average, because these measurements are correlated and the uncertainties are not independent.

Chapter 8

Conclusions

This thesis describes a measurement of the top quark mass. Events passing a set of selection criteria are analyzed with the ideogram technique. This technique computes a likelihood as a function of the top quark mass and the fraction of $t\bar{t}$ events in the selected data sample, which are determined simultaneously. The likelihood incorporates signal and (combinatorial) background. Key ingredients in the likelihood calculation are a kinematic fit to the events and a discriminant which discriminates between signal and background events.

On 855 data events selected from a data sample with an integrated luminosity of approximately 1 fb^{-1}, collected with the DØ detector between April 2002 and February 2006, the top quark mass is measured to be:

$$m_t = 176.4 \pm 1.9 \text{ (stat.)}^{+2.2}_{-2.3} \text{ (syst) GeV}/c^2 \,.$$

The analysis is calibrated to the input top quark mass of the Pythia Monte Carlo simulation, which is the pole mass of the top quark.

Several consistency checks were performed: the data sample was split according to the number of b tags and according to jet multiplicity. All results were consistent with each other. The measurement presented here is compatible with the world average of top quark mass measurements. It differs by 1.6 standard deviations from the result of a measurement with the matrix element technique on the same data set.

Merits of the ideogram technique are that it computes a full likelihood using all possible jet-parton assignments, it is computationally fast, and it is flexible: modifications are easily performed. The analysis can in the future be improved with the following modifications: a better Monte Carlo simulation, e.g. `MC@NLO`, fitting the JES factor, and an improvement of the approximations of the likelihood, such as a better treatment of events with more than four jets.

The measurement of the top quark mass constrains the Standard Model by providing a constraint on the mass of the Higgs boson. Figure 8.1 shows the plane of

the W boson mass, M_W, versus the top quark mass, m_t, with the contour of the 1 σ uncertainty on the mass of the top quark and the W boson. The top quark mass and its uncertainty are the ones from this analysis. The preferred Higgs boson mass with this top quark mass is 100^{+24}_{-20} GeV/c^2. A Higgs boson mass up to 114 GeV/c^2 is already excluded at 95 % confidence level by direct searches at LEP. The uncertainties are computed using only the uncertainties of the top quark mass, not the uncertainty on the W boson mass. The predicted Higgs boson mass, below the LEP exclusion limit, is in the mass region where the LHC searches will be least sensitive. At the LHC, the most sensitive channel in this mass region is expected to be the $H \to \gamma\gamma$ decay channel, which will experimentally be a challenging channel.

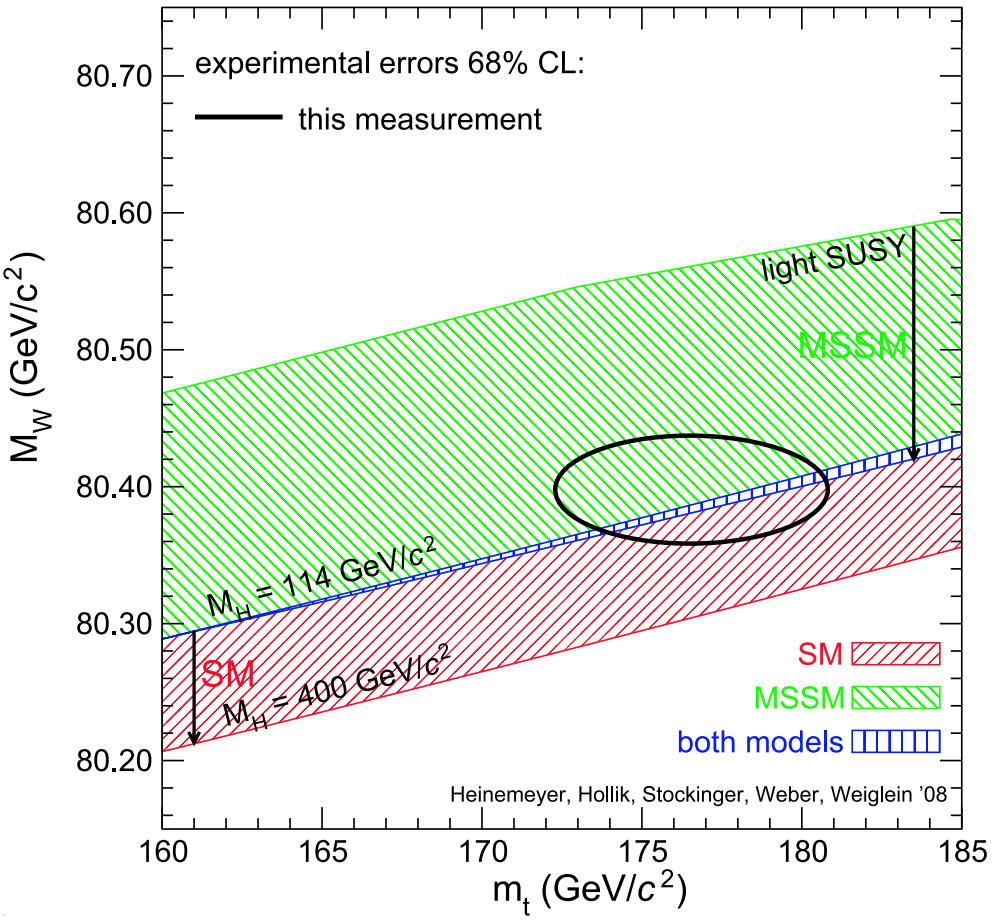

Figure 8.1: *The plane of the top quark mass and the mass of the W boson. In this plane the regions allowed by the Standard Model and the minimal supersymmetric Standard Model are indicated. The ellipse indicates the 68% confidence interval of the present day measurement of the W boson mass and the top quark mass measurement described in this thesis.*

Appendix A

Correlation with the matrix element analysis

Reference [84] describes a top quark mass measurement with the matrix element technique on the same data set as used for this thesis, which is also briefly described in Section 5.1. To compare the two analyses, it is important to know the correlation between these two analysis techniques. In this appendix the correlation between the two techniques is obtained from ensemble tests. Also the significance of the difference between the results obtained with the two analysis methods is given.

From samples of Monte Carlo events, event collections are created containing $t\bar{t}$ events and background events. Both analyses are applied on each event collection to extract two top quark mass measurements. Application of both analysis techniques to one event collection can be considered as one pseudo-experiment with two outcomes which are correlated. By performing many pseudo-experiments the correlation coefficient ($\rho_{m_t^{\rm ID} m_t^{\rm ME}}$) between the two outcomes obtained with the two analysis techniques is computed:

$$\begin{aligned} \rho_{m_t^{\rm ID} m_t^{\rm ME}} &= \frac{\mathrm{cov}(m_t^{\rm ID}, m_t^{\rm ME})}{\sigma(m_t^{\rm ID})\sigma(m_t^{\rm ME})} \\ &= \frac{\frac{1}{1000}\sum_{i=1}^{1000}(m_{t\,i}^{\rm ID} - \langle m_t^{\rm ID}\rangle)(m_{t\,i}^{\rm ME} - \langle m_t^{\rm ME}\rangle)}{\sigma(m_t^{\rm ID})\sigma(m_t^{\rm ME})}, \end{aligned} \tag{A.1}$$

with $m_{t\,i}^{\rm ID}$ and $m_{t\,i}^{\rm ME}$ the measured masses in one pseudo-experiment with the ideogram and the matrix element technique respectively, $\langle m_t^{\rm ID}\rangle$ and $\langle m_t^{\rm ME}\rangle$ their respective means, $\sigma(m_t^{\rm ID})$ and $\sigma(m_t^{\rm ID})$ their standard deviations, and $\mathrm{cov}(m_t^{\rm ID}, m_t^{\rm ME})$ their covariance.

The samples used are $t\bar{t}$ events with an input top quark mass of 170 GeV/c^2 generated with the Monte Carlo event generator Alpgen interfaced with Pythia for

the showering and decay and the W+jets samples already described. The matrix element analysis does not use QCD events in its own ensemble tests for calibration. Therefore, in the combined ensemble test no QCD events are used. Pseudo-experiments with 855 events (that pass the χ^2 selection criterion) are created according to the fractions in Table 4.4 with the QCD events replaced by W+jets events. It should be noted that the matrix element analysis uses a different event selection than the analysis described in this thesis. It only selects events with exactly four jets with $p_T > 20$ GeV/c.

The matrix element measurement presented in Ref. [84] simultaneously fits a JES factor. Via this fit the top quark mass measurement may be influenced due to statistical fluctuations, to which the ideogram method without a JES factor fit is insensitive. An important quantity is the correlation between a measurement with the ideogram technique and a measurement with the matrix element technique in which the JES factor is not fitted. For this study, the matrix element method is therefore applied without fitting the JES factor. With a thousand event collections the correlation between the two top quark mass measurements is found to be 35%.

Both analyses techniques are used on data and are likely to result in different measured top quark masses. The important quantity is the significance of the difference, which is the observed difference $(m_t^{\mathrm{ID}} - m_t^{\mathrm{ME}})$ minus the expected (or mean) difference $(\langle m_t^{\mathrm{ID}} - m_t^{\mathrm{ME}} \rangle)$ divided by the standard deviation of the difference $(\sigma(m_t^{\mathrm{ID}} - m_t^{\mathrm{ME}}))$:

$$\text{significance} = \frac{|(m_t^{\mathrm{ID}} - m_t^{\mathrm{ME}}) - \langle m_t^{\mathrm{ID}} - m_t^{\mathrm{ME}} \rangle|}{\sigma(m_t^{\mathrm{ID}} - m_t^{\mathrm{ME}})} \,. \tag{A.2}$$

The difference between the two results is expected to be zero, so $\langle m_t^{\mathrm{ID}} - m_t^{\mathrm{ME}} \rangle = 0$ GeV/c^2. The standard deviation, $\sigma(m_t^{\mathrm{ID}} - m_t^{\mathrm{ME}})$, is the square root of the variance $(V(m_t^{\mathrm{ID}} - m_t^{\mathrm{ME}}))$:

$$\begin{aligned} \sigma^2(m_t^{\mathrm{ID}} - m_t^{\mathrm{ME}}) &= V(m_t^{\mathrm{ID}} - m_t^{\mathrm{ME}}) \\ &= V(m_t^{\mathrm{ID}}) + V(m_t^{\mathrm{ME}}) - 2\mathrm{cov}(m_t^{\mathrm{ID}}, m_t^{\mathrm{ME}}) \\ &= \sigma^2(m_t^{\mathrm{ID}}) + \sigma^2(m_t^{\mathrm{ME}}) - 2\sigma(m_t^{\mathrm{ID}})\sigma(m_t^{\mathrm{ME}})\rho_{m_t^{\mathrm{ID}} m_t^{\mathrm{ME}}} \end{aligned} \tag{A.3}$$

The standard deviations of the two analysis methods ($\sigma(m_t^{\mathrm{ID}})$ and $\sigma(m_t^{\mathrm{ME}})$) are the predictions coming from the ensemble tests and are 2.1 GeV/c^2 (ideogram) and 1.9 GeV/c^2 (matrix element). Thus, the standard deviation of the difference between the two measurements ($\sigma(m_t^{\mathrm{ID}} - m_t^{\mathrm{ME}})$) is 2.3 GeV/$c^2$, and the significance of the difference observed on data is:

$$\text{significance} = \frac{|m_t^{\mathrm{ID}} - m_t^{\mathrm{ME}}|}{2.3\,\mathrm{GeV}/c^2} \,. \tag{A.4}$$

with m_t^{ID} the top quark mass measured with the ideogram method and m_t^{ME} the result of the matrix element method. The difference observed on data is 3.5 GeV/c^2, corresponding to a significance of 1.6.

Bibliography

[1] J. Dalton, *On the absorption of gases by water and other liquids.* Memoirs of the Literary and Philosophical Society of Manchester, Second Series **1**, 271 (1805).

[2] E. Rutherford, *The scattering of a and b particles by matter and the structure of the atom.* Philosophical Magazine, Series 6 **21**, 669 (1911).

[3] J.J. Thomson, *Cathode rays.* Philosophical Magazine **44**, 293 (1897).

[4] E. Rutherford, *Collision of alpha particles with light atoms; an anomalous effect in Nitrogen.* Philosophical Magazine **37**, 537 (1919).

[5] J. Chadwick, *The existence of a neutron.* Proc. Roy. Soc., A **136**, 692 (1932).

[6] M. Gell-Mann, *A schematic model of baryons and mesons.* Phys. Lett. **8**, 214 (1964).

[7] F. Abe *et al.* [CDF], *Observation of top quark production in $p\bar{p}$ collisions with the CDF detector at Fermilab.* Phys. Rev. Lett. **74**, 2626 (1995).

[8] S. Abachi *et al.* [D0], *Observation of the top quark.* Phys. Rev. Lett. **74**, 2632 (1995).

[9] S. Glashow, *Partial symmetries of weak interactions.* Nucl. Phys. **22**, 579 (1961).

[10] A. Salam, *Elementary Particle Theory.* Almqvist and Wiksell, Stockholm, 1968.

[11] S. Weinberg, *A model of leptons.* Phys. Rev. Lett. **19**, 1264 (1967).

[12] M. Veltman, *Perturbation theory of massive Yang-Mills fields.* Nucl. Phys. B **7**, 637 (1968).

[13] G. 't Hooft, *Renormalizable Lagrangians for massive Yang-Mills fields.* Nucl. Phys. B **35**, 167 (1971).

[14] G. 't Hooft and M. Veltman, *Regularization and renormalization of gauge fields.* Nucl. Phys. B **44**, 189 (1972).

[15] G. 't Hooft and M. Veltman, *Combinatorics of gauge fields.* Nucl. Phys. B **50**, 318 (1972).

[16] [Particle Data Group]. J. Phys. G: Nucl. Part. Phys. **33**, 97 (2006).

[17] G. Abbiendi *et al.* (ALEPH Collaboration, Delphi Collaboration, L3 Collaboration, OPAL Collaboration and The LEP Working Group for Higgs Boson Searches), *Search for the standard model higgs boson at LEP.* Phys. Lett. B **565**, 61 (2003).

[18] M. Veltman, *Radiative corrections to vector boson masses.* Phys. Lett. B **91**, 95 (1980).

[19] F. Antonelli, M. Consoli and G. Corbò, *One-loop correction to vector boson masses in the Glashow-Weinberg-Salam model of electromagnetic and weak interactions.* Phys. Lett. B **91**, 90 (1980).

[20] M. Consoli and W. Hollik, *Electroweak radiative corrections for Z physics*, in *Z physics at LEP*, eds. G. Altarelli, R. Kleiss and C. Verzegnassi, Vol. 1, p. 7. 1989.

[21] S. Weinberg, *The Quantum Theory of Fields.* Cambridge University Press, 1995.

[22] [Particle Data Group]. J. Phys. G: Nucl. Part. Phys. **33**, 518 (2006).

[23] M. Cacciari, S. Frixione, M. Mangano, P. Nason and G. Ridolfi, *The $t\bar{t}$ cross-section at* 1.8 *TeV and* 1.96 *TeV: a study of the systematics due to parton densities and scale dependence.* JHEP **04**, 068 (2004).

[24] N. Kidonakis and R. Vogt, *Next-to-next-to-leading order soft-gluon corrections in top quark hadroproduction.* Phys. Rev. D **68**, 114014 (2003).

[25] V. Abazov *et al.* [D0], *Evidence for production of single top quarks and first direct measurement of $|V_{tb}|$.* Phys. Rev. Lett. **98**, 181902 (2007).

[26] I. Bigi and Y. Dokshitzer and V. Khoze and J. Kühn and P. Zerwas, *Production and decay properties of ultra-heavy quarks.* Phys. Lett. B **181**, 157 (1986).

[27] M. Jeżabek and J. Kühn, *QCD corrections to semileptonic decays of heavy quarks.* Nucl. Phys. B **314**, 1 (1989).

[28] S. Heinemeyer, W. Hollik, D. Stöckinger, A. Weber and G. Weiglein, *Precise prediction for M_W in the MSSM.* JHEP **08**, 052 (2006).

[29] S. Heinemeyer, W. Hollik and G. Weiglein, *Electroweak precision observables in the minimal supersymmetric standerd model.* Phys. Rept. **425**, 265 (2006).

[30] A. Djouadi, P. Gambino, S. Heinemeyer, W. Hollik, C. Jünger and G. Weiglein, *Supersymmetric contributions to electroweak precision observables: QCD corrections.* Phys. Rev. Lett. **78**, 3626 (1997).

[31] A. Djouadi, P. Gambino, S. Heinemeyer, W. Hollik, C. Jünger and G. Weiglein, *Leading QCD corrections to scalar quark contributions to electroweak precision observables.* Phys. Rev. D **57**, 4179 (1998).

[32] S. Heinemeyer and G. Weiglein, *Leading electroweak two-loop corrections to precision observables in the MSSM.* JHEP **10**, 072 (2002).

[33] J. Haestier, S. Heinemeyer, D. Stöckinger and G. Weiglein, *Electroweak precision observables: Two-loop Yukawa corrections of supersymmetric particles.* JHEP **12**, 027 (2005).

[34] S. Dimopoulos and H. Georgi, *Softly broken supersymmetry and SU(5).* Nucl. Phys. B **193**, 150 (1981).

[35] C. Hill, *Topcolor: Top quark condensation in a gauge extension of the standard model.* Phys. Lett. B **266**, 419 (1991).

[36] C. Hill, *Topcolor assisted technicolor.* Phys. Lett. B **345**, 483 (1995).

[37] C. Hill and S. Parke, *Top quark production: Sensitivity to new physics.* Phys. Rev. D **49**, 4454 (1994).

[38] H. Nilles, *Supersymmetry, supergravity and particle physics.* Phys. Rep. **110**, 1 (1984).

[39] H. Haber and G. Kane, *The search for supersymmetry: Probing physics beyond the standard model.* Phys. Rep. **117**, 75 (1985).

[40] E. Simmons, *Thinking about top: Looking outside the standard model.* Preprint. Hep-ph/9908511.

[41] E. Simmons, *The top quark: Experimental roots and branches of theory.* Preprint. Hep-ph/0211335.

[42] D. Choudhury, T. Tait and C. Wagner, *Beautiful mirrors and precision electroweak data.* Phys. Rev. D **65**, 053002 (2002).

[43] V. Abazov *et al.* [D0], *The upgraded DØ detector.* Nucl. Instr. and Methods A **565**, 463 (2006).

[44] M. Dobbs, S. Frixione, E. Laenen, K. Tollefson *et al.*, *Les Houches guidebook to Monte Carlo generators for hadron collider physics.* 2004. Hep-ph/0403045.

[45] T. Sjöstrand, P. Edén, C. Friberg, L. Lönnblad, G. Miu, S. Mrenna and E. Norrbin, *Pythia 6.2 physics and manual.* Computer Physics Commun. **135**, 238 (2001).

[46] M. Whalley, D. Bourilkov and R. Group, *Contributed to HERA and the LHC: A workshop on the implications of HERA and LHC physics* (2005).

[47] M. Mangano, F. Piccinini, A. Polosa, M. Moretti and R. Pittau, *ALPGEN, a generator for hard multiparton processes in hadronic collisions.* JHEP **07**, 001 (2003).

[48] F. Krauss, *Matrix elements and parton showers in hadronic interactions.* JHEP **08**, 015 (2002).

[49] S. Hoeche, F. Krauss, N. Lavesson, L. Lonnblad, M. Mangano, A. Schaelicke and S Schumann, *Matching parton showers and matrix elements* (2006). Hep-ph/0602031.

[50] Y. Peters, M. Begel, E. Shabalina and D. Wicke, *D0 Note 5406: Study of the W+Jets heavy flavor scale factor in p17*, 2007.

[51] R. Brun and F. Carminati, *CERN program library long writeup, W5013*, 1993.

[52] P. Calfayan, T. Gadfort, G. Hesketh, V. Lesne, M. Owen, R. Stroehmer, V. Sharyy and B. Tuchming, *D0 Note: Muon Identification Certification for p17 data*, 2007.

[53] U. Bassler and G. Bernardi, *D0 Note 4124: Towards a Coherent Treatment of Calorimetric Energies: Missing Transverse Energy, Jets, E.M. Objects and the T42 Algorithm.*

[54] J.-R. Vlimant, U. Bassler, G. Bernardi and S. Trincaz-Duvoid, *D0 Note 4146: Technical description of the T42 algorithm for the calorimeter noise suppression*, 2003.

[55] G. Bernardi, E. Busato and J.-R. Vlimant, *D0 Note 4335: Improvements from the T42 Algorithm on Calorimeter Objects Reconstruction*, 2004.

[56] G. Blazey, J. Dittmann, S. Ellis, D. Elvira, K. Frame, S. Grinstein, R. Hirosky, R. Piegaia, H. Schellman, R. Snihur, V. Sorin and D. Zeppenfeld, *Run II jet physics*, in *QCD and Weak Boson Physics in Run II*, eds. Baur, U. and Ellis, R. K. and Zeppenfeld, D., p. 47. 2000.

[57] A. Harel, *D0 Note 4919: Jet ID Optimization*, 2005.

[58] C. Anăstăsoaie, S. Robinson and T. Scanlon, *D0 Note 5213: Performance of the NN b-tagging Tool on p17 Data*, 2007.

[59] C. Anăstăsoaie, *A search for $W^{\pm}H \to \mu\nu b\bar{b}$ production at the Tevatron.* Thesis, University of Nijmegen, 2008.

[60] S. Trincaz-Duvoid and P. Verdier, *D0 Note: Missing ET Rconstruction in p17*, 2004.

[61] C. Peterson, D. Schlatter, I. Schmitt and P. M. Zerwas, *Scaling violations in exclusive e^+e^- annihilation spectra.* Phys. Rev. D **27**, 105 (1983).

[62] Y. Peters, K. Hamacher and D. Wicke, *D0 Note 5229: Precise Tuning of the b fragmentation for the DØ Monte Carlo*, 2006.

[63] C. Ochando and J.-F. Grivaz, *D0 Note 5609: SSR for p17*, 2008.

[64] P. Gris, *D0 Note 5400: Electron Smearing Studies with RunIIa Data*, 2007.

[65] L. Christofek, *D0 Note 4978: Text and Trigger Tables for Publications for the Top Quark Physics Group*, 2006.

[66] M. Begel and S.-J. Park, *D0 Note 5324: Efficiency of the Data Quality Calorimeter Flags*, 2007.

[67] J. Brunelle, D.K. Cho, U. Heintz, M. Narain, S.-J. Park, M.-A. Pleier and E. Shabalina, *D0 Note 5249: Measurement of the $t\bar{t}$ Production Cross-Section at $\sqrt{s} = 1.96$ TeV in the Lepton+Jets Final State using a Topological Method on 1 fb^{-1} of DØ Data*, 2006.

[68] V. Barger and R. Phillips, *Collider Physics.* Addinson-Wesley Publishing Co., 1987.

[69] J. Brunelle, D.K. Cho, U. Heintz, M. Narain, S.-J. Park, M.-A. Pleier, E. Shabalina and M. Weber, *D0 Note 5354: Measurement of the top-antitop quark pair production cross section in proton-antiproton collisions at $\sqrt{s} = 1.96$ TeV in the lepton+jets final state using event kinematics on 900 pb^{-1} of DØ data*, 2007.

[70] S. Abachi *et al.* [D0], *Observation of the top quark.* Phys. Rev. Lett. **74**, 2632 (1995).

[71] S. Abachi *et al.* [D0], *Direct measurement of the top quark mass.* Phys. Rev. Lett. **79**, 1197 (1997).

[72] B. Abbott *et al.* [D0], *Direct measurement of top quark mass by the D0 collaboration.* Phys. Rev. D **58**, 052001 (1998).

[73] F. Abe *et al.* [CDF], *Evidence for top quark production in $p\bar{p}$ collisions at $\sqrt{s} =$ 1.8 TeV.* Phys. Rev. D **50**, 2966 (1994).

[74] F. Abe *et al.* [CDF], *Evidence for top production in $p\bar{p}$ collisions at $\sqrt{s} = 1.8$ TeV.* Phys. Rev. Lett. **73**, 225 (1994).

[75] F. Abe *et al.* [CDF], *Observation of top quark production in $p\bar{p}$ collisions with the Collider Detector at Fermilab.* Phys. Rev. Lett. **74**, 2626 (1995).

[76] F. Abe *et al.* [CDF], *Measurement of the top quark mass.* Phys. Rev. Lett. **80**, 2767 (1998).

[77] F. Abe *et al.* [CDF], *Measurement of the top quark mass with the collider detector.* Phys. Rev. Lett. **82**, 271 (1999).

[78] T. Affolder *et al.* [CDF], *Measurement of the top quark mass with the Collider Detector at Fermilab.* Phys. Rev. D **63**, 032003 (2001).

[79] A. Abulencia *et al.* [CDF], *Top quark mass measurement using the template method in the lepton + jets channel at CDF II.* Phys. Rev. D **73**, 032003 (2006).

[80] A. Abulencia *et al.* [CDF], *Precision top quark mass measurement in the lepton + jets topology in p anti-p collisions at $\sqrt{s} = 1.96$ TeV.* Phys. Rev. Lett. **96**, 022004 (2006).

[81] T. Aaltonen, *at al.* [CDF], *Measurement of the top-quark mass using $\not\!\!E_T$+ jets events with secondary vertex b-tagging at CDF II.* Phys. Rev. D **75**, 111103 (2007).

[82] V. Abazov *et al.* [D0], *An improved measurement of the top quark mass.* Nature **429**, 638 (2004).

[83] V. Abazov *et al.* [D0], *Measurement of the top quark mass in the lepton+jets final state with the matrix element method.* Phys. Rev. D **74**, 092005 (2006).

[84] V. Abazov *et al.* [D0], *Precise measurement of the top quark mass from lepton+jets events.* Phys. Rev. Lett. **101**, 182001 (2008).

[85] A. Abulencia *et al.* [CDF], *Measurement of the top quark mass with the dynamical likelihood method using lepton plus jets events with b-tags in $p\bar{p}$ collisions at $\sqrt{s} = 1.96$ TeV.* Phys. Rev. D **73**, 092002 (2006).

[86] A. Abulencia *et al.* [CDF], *Precise measurement of the top quark mass in the lepton+jets topology at CDF II.* Phys. Rev. Lett. **99**, 182002 (2007).

[87] V. Abazov *et al.* [D0], *Measurement of the top quark mass in the lepton+jets channel using the ideogram method.* Phys. Rev. D **75**, 092001 (2007).

[88] T. Aaltonen *et al.* [CDF], *Measurement of the top-quark mass in all-hadronic decays in $p\bar{p}$ collisions at CDF II.* Phys. Rev. Lett. **98**, 142001 (2007).

[89] P. Abreu *et al.* [DELPHI], *Measurement of the W-pair cross-section and the W mass in e^+e^- interactions at 172 GeV.* Eur. Phys. J. C **2**, 581 (1998).

[90] P. Abreu *et al.* [DELPHI], *Measurement of the mass of the W boson using direct reconstruction at $\sqrt{s} = 183$ GeV.* Phys. Lett. B **462**, 410 (1999).

[91] P. Abreu *et al.* [DELPHI], *Measurement of the mass and width of the W boson in e^+e^- collisions at $\sqrt{s} = 189$ GeV.* Phys. Lett. B **511**, 159 (2001).

[92] A. Magerkurth, *D0 Note 4708: Parton Level Corrections for Jetcorr 5.3*, 2005.

[93] S. Snyder, *Measurement of the Top Quark Mass at D0.* Thesis, State University of New York at Stony Brook, 1995.

[94] *private communication with D. Boline.*

[95] J. Pumplin *et al.* [CTEQ Collaboration], *New generation of parton distributions with uncertainties from global QCD analysis.* JHEP **07**, 012 (2002).

[96] H. Lai *et al.* [CTEQ Collaboration], *Global QCD analysis of parton structure of the nucleon: CTEQ5 parton distributions.* Eur. Phys. J. C **12**, 375 (2000).

[97] A. Martin, R. Roberts, W. Stirling and R. Thorne, *Parton distributions and the LHC: W and Z production.* Eur. Phys. J. C **14**, 133 (2000).

[98] *private communication with M. Wang.*

[99] [Tevatron Electroweak Working Group], *Combination of CDF and DØ results on the mass of the top quark* (2008). arXiv:0803.1683v1 [hep-ex].

Summary

The best description of nature at a sub-nuclear scale ($< 10^{-14}$ m) is given by the Standard Model of particle physics. This model describes nature in terms of particles and their interactions. The Standard Model has proven to be a very successful description with which several correct predictions were made. There only seems to be one unelegant property of the model: all particles are massless, whereas, in reality, they have diverse masses. To explain the masses of the particles in the model, the Brout-Englert-Higgs mechanism has been introduced in the theory. This mechanism should lead to the existence of at least one additional particle, the Higgs boson, which can be produced if enough energy is brought together. However, it has never been found experimentally. Proving the existence of the Higgs boson is the quest of many physicists.

One of the elementary particles described by the Standard Model is the top quark. It is the heaviest of the quarks with a mass approximately thirty times the mass of the second heaviest quark. Because the mass of the top quark and the mass of the Higgs boson are correlated in the Standard Model, precise knowledge of the former gives a prediction for the latter.

This thesis describes a measurement of the mass of the top quark. At the moment, the Tevatron collider at Fermilab near Chicago is the only leboratory where top quarks can be produced, which happens in collisions of protons and anti-protons at a centre-of-mass energy of 1.96 TeV. Due to the nearly immediate decay of the produced particles, not the particles themselves, but their decay products are measured. This is done with the DØ detector, which registers the collisions (also called *events*). For the measurement described here, collisions are used which took place between April 2002 and February 2006 and which correspond to an integrated luminosity of 1 fb^{-1}.

For this measurement only events in which a top quark has been produced together with an aniti-top quark ($t\bar{t}$ events), are searched. A top quark decays almost instantaneously to a W boson and a bottom quark. The latter leads to a so called b jet. A top quark and an anti-top quark thus decay to two W bosons and two b jets. Events in which one of the W bosons decays hadronically and the other one decays leptonically, are searched for. This is called the semi-leptonic channel. It is characterized by the presence of a charged lepton, four jets, of which two are b jets, and missing

transverse energy caused by the neutrino escaping detection. The main background, which are events in which no top quark pair is present, but which are selected, is formed by events with a leptonically decaying W boson plus jets (W+jets-events) en QCD events. With a number of criteria a sample of 855 events is selected. The amounts of $t\bar{t}$ events and background events are estimated with a combined quantity that discriminates between $t\bar{t}$ and background events. This discriminant combines six reconstructed variables which distringuish $t\bar{t}$ events from background events.

The top quark mass is measured with the ideogram technique. This happens by computing a likelihood as a function of the top quark mass. The position of the maximum of this likelihood gives the top quark mass. The likelihood accounts for the presence of both $t\bar{t}$ and background events and also for the presence of wrongly reconstructed $t\bar{t}$ events

Due to several assumptions and approximations in the computation of the likelihood, the result differs from the true top quark mass, which necessitates a calibration. The relation between the top quark mass determined with the likelihood and the true top quark mass is parametrized using simulated events. This parametrization is used to calibrate the top quark mass, which results in the following:

$$m_t = 176.4 \pm 1.9 \text{ (stat.)}^{+2.2}_{-2.3} \text{ (syst.) GeV}/c^2 \,.$$

As a check, the measurement is also performed on events split according to the number of b tags and the jet multiplicity. The results of these checks are all consistent with each other. Because simulated events have been used for the calibration of the measurement, all possible systematic differences between simulation and data are investigated and estimated.

This measurement is a bit higher than the world average of top quark mass measurements, but they are compatible within the uncertainties. The relatively high measured top quark mass leads to an increase in the prediction of the Higgs boson mass to 100^{+24}_{-20} GeV/c^2.

Samenvatting

De beste beschrijving van de natuur op sub-nucleaire schaal ($< 10^{-14}$ m) wordt gegeven door het standaardmodel der hoge-energiefysica. Dit model beschrijft de natuur in termen van deeltjes en hun interacties. Het standaardmodel is een zeer succesvolle beschrijving gebleken waarmee verschillende uitgekomen voorspellingen zijn gedaan. Er lijkt slechts één schoonheidsfoutje in dit model te bespeuren: alle deeltjes zijn massaloos, terwijl ze in werkelijkheid de meest uiteenlopende massa's hebben. Om de massa's van de deeltjes in het model te verklaren, is het Brout-Englert-Higgs-mechanisme ingevoerd in de theorie. Dit mechanisme zou moeten leiden tot tenminste één extra deeltje, het Higgs-boson, dat gemaakt kan worden als er genoeg energie wordt samengebracht. Dit is echter nog nooit experimenteel gevonden. Het aantonen dat het Higgs-boson bestaat, is het streven van veel natuurkundigen.

Eén van de elementaire deeltjes die door het standaardmodel beschreven worden, is het topquark. Dit is het zwaarste van de quarks met een massa die ruim dertig keer zo groot is als de massa van het één-na-zwaarste quark. Doordat de massa van het topquark en de massa van het Higgs-boson in het standaardmodel gecorreleerd zijn, levert nauwkeurige kennis van de topquarkmassa een voorspelling van de Higgsbosonmassa op.

Dit proefschrift beschrijft een meting van de massa van het topquark. Op dit moment is de Tevatronversneller op het Fermilab bij Chicago het enige laboratorium waar topquarks geproduceerd kunnen worden, en wel in botsingen van protonen en antiprotonen bij een zwaartepuntsenergie van 1,96 TeV. Doordat geproduceerde deeltjes direct vervallen, worden niet de deeltjes zelf gemeten, maar hun vervalsproducten. Dit wordt gedaan met de DØ-detector, die de botsingen (ook wel *events* genoemd) registreert. Voor de meting die hier beschreven wordt, zijn de botsingen gebruikt die plaats vonden tussen april 2002 en februari 2006 en die corresponderen met een geïntegreerde luminositeit van 1 fb^{-1}.

Voor deze meting wordt alleen gezocht naar events waarbij een topquark is geproduceerd in combinatie met een anti-topquark ($t\bar{t}$-events). Een topquark vervalt nagenoeg onmiddellijk naar een W-boson en een bottomquark. Dit laatste leidt tot een zogenaamde b-jet. Een topquark en een anti-topquark vervallen dus naar twee W-bosonen en twee b-jets. Er wordt gezocht naar events waarbij één van de W-

bosonen hadronisch vervalt en het andere leptonisch. Dit wordt het semi-leptonische kanaal genoemd. Het wordt gekarakteriseerd door de aanwezigheid van een geladen lepton, vier jets, waarvan twee b-jets, en missende energie, die veroorzaakt wordt door het neutrino dat niet gedetecteerd wordt. De belangrijkste achtergrond, dat zijn events waarin geen topquarkpaar voorkomt, maar die wel geselecteerd worden, wordt gevormd door events met een leptonisch vervallend W-boson plus jets (W+jets-events) en QCD-events. Met een aantal criteria wordt een sample van 855 events geselecteerd. De hoeveelheden $t\bar{t}$-events en achtergrondevents worden geschat met een samengestelde grootheid die discrimineert tussen $t\bar{t}$- en achtergrondevents. Deze discriminant combineert zes gereconstrueerde grootheden die $t\bar{t}$-events onderscheiden van achtergrondevents.

De topquarkmassa wordt gemeten met de ideogramtechniek. Dit gebeurt door een likelihood als functie van de topquarkmassa uit te rekenen. De positie van het maximum van deze likelihood geeft de topquarkmassa. De likelihood houdt rekening met de aanwezigheid van zowel $t\bar{t}$- als achtergrondevents en tevens met de aanwezigheid van foutief gereconstrueerde $t\bar{t}$-events.

Door verschillende aannames en benaderingen in de berekening van de likelihood wijkt het resultaat af van de werkelijke topquarkmassa, waardoor calibratie noodzakelijk is. Met behulp van gesimuleerde events wordt het verband tussen de topquarkmassa die bepaald is met de likelihood en de werkelijke massa van het topquark geparametriseerd. Deze parametrisatie wordt gebruikt om de topquarkmassa te calibreren, wat leidt tot het volgende resultaat:

$$m_t = 176.4 \pm 1.9\ (\text{stat.})^{+2.2}_{-2.3}\ (\text{syst.})\ \text{GeV}/c^2\,.$$

Ter controle wordt de meting ook uitgevoerd op events opgesplitst naar het aantal b-tags en de jetmultipliciteit. De resultaten hiervan zijn allemaal consistent met elkaar. Omdat gesimuleerde events gebruikt zijn voor de calibratie van de meting, worden alle mogelijke systematische afwijkingen tussen de simulatie en de data onderzocht en afgeschat.

Deze meting is iets hoger dan het wereldgemiddelde van topquarkmassametingen, maar is hiermee compatibel binnen de onzekerheden. De relatief hoge gemeten topquarkmassa leidt tot een verhoging van de voorspelde Higgs-bosonmassa tot 100^{+24}_{-20} GeV/c^2.

Acknowledgements

During the trajectory that lies behind me now, many people have helped me or contributed to the result you hold in your hands. First of all, I thank my promotores, Frank Linde for providing me with the opportunity to do my research at Nikhef with the D0 experiment, and Marcel Demarteau for giving me great supervision. Co-promotor Marcel Vreeswijk provided daily supervision. I am much indebted to both Marcels for both sharing their insights and motivating me, which they did with enthusiasm and patience. Marcel Demarteau was also there to give me a figurative kick in the butt when it was really necessary.

In my first months at Nikhef, the first generation of Nikhef D0 students, Lukas, Paul, Onne and Freya showed me around in the D0 software. Half a year after I had started at Nikhef I moved to the windy city, Chicago, not much later followed by Miruna and later by Pieter vdB and Jeroen, with whom I would work in good collaboration during the years that were about to come. After a short stay in the Fermilab dorms Miruna and I decided to share an apartment in the burbs, not far from our friendly neighbours Cristina and mr Sanders. During this stay at Fermilab and the other periods of my PhD program, I was helped a lot by all members of the Dutch D0 group: my former masters supervisor Sijbrand, who had convinced me to work on D0 in the first place, Paul de Jong, Frank Filthaut and Bob van Eijk, who were always available for discussions about D0 or to comment on my work, and with the guys from Nijmegen: Axel, Bram, Cristina, Miruna, Silke, Lucian and Kirby. Apart from good colleagues, the Dutch D0 guys showed to be good friends and I do keep very warm memories to our time in Chicago. I cannot finish my thesis without mentioning the Wang family, entrepreneurs in Warrenville; no matter what Freya said, the honey sesame chicken was worth the shorter life expectancy.

While at Fermilab I started working on my analysis. Two people were of crucial importance during this period and in fact for the eventual measurement presented in this thesis. Firstly, I want to thank Martijn Mulders, who introduced me to the ideogram technique and taught me quite a bit about statistics. Secondly, a big thanks must go to Michele Weber with whom I took over Martijn's analysis and measured the top quark mass on a larger data set and, as we believed, with an improved analysis. I appreciated the good cooperation with both these fellow ideogrammers. Also I

must thank everyone in the top group of D0 who helped to obtain this result and in particular the top group conveners and ex-conveners.

Back at Nikhef, there were of course Jeroen and Pieter again, but also the members of the entire Atlas group who were always available for lunch or a friendly chat. Thank you all! Teaching physics to students with my own supervisor Marcel Vreeswijk and Auke-Pieter Colijn was a nice relieve from sitting behind the computer all day. Very few students will forget what a *Beagle Boy* is.

During the past years, there have of course been many friends who lightened up my life outside the buildings of science (although some didn't help speeding up my thesis work). There are too many to mention, but some need a word of appreciation here. A special thanks should go to Niels, whose friendship I can always appreciate. Also Gossie, thanks a lot for the new experiences! My family, Piet and Anneke and Jaap, Koen and Karen, thank you for the support in the past years! Last but not least a big sign of gratitude should be paid to Bram and Miruna, not only for their pleasant friendship and for listening to my complaining once in a while, but also for actually helping me finish this thesis. Without their help there would probably be an unpublished, but fully approved manuscript lying in a drawer somewhere. All, thanks a lot!